**UNIVERSITÀ DEGLI STUDI DI MILANO**
SCUOLA DI DOTTORATO
TERRA, AMBIENTE E BIODIVERSITÀ

Dottorato di Ricerca in Ecologia Agraria
Ciclo XXIV

# Evaluation of a remote sensing based method for the assessment of agricultural crop residues on the soil surface

Ph.D. Thesis

**Paolo Prosperi**
R08435

*Supervisor*
Prof. Stefano Bocchi

*Coordinator*
Prof. Graziano Zocchi

Academic Year 2010-2011

# Table of Contents

# Index of Tables



# Index of Figures

# *Abstract*

Increased agricultural mechanization in the recent past and susceptibility of certain soils to degradation generate widespread concern among experts on the overall environmental sustainability of some of the current agricultural practices in Europe. A number of solutions could be adopted to better preserve soil resources, some of which are already supported by the Common Agricultural Policy (CAP).

Researchers demonstrated that erosion and reduction in soil organic matter are among the most acute degradation issues in Europe and that the release of crop residues on the soil surface after harvesting can greatly reduce their incidence. The use of a permanent soil cover (e.g. by use of crop residues) is one of the three fundamental principles of Conservation Agriculture.

Quantifying the amount of crop residues on the ground is important for soil and water protection, modelling of erosion processes and legislation enforcement purposes. However, common monitoring methods based on ground sampling are expensive and likely to be impracticable on vast surfaces. Remote sensing can offer a valid alternative for monitoring.

The present research intends to contribute to the efforts towards the establishments of methods for the assessment and monitoring, through remote sensing, of the effects of conservation agriculture practices on the environment, with focus on soil resources. In this respect, the research specific objective is the evaluation of a remote sensing based method for the quantification of crop residue cover in a conservation agriculture farm in Northern Italy by use of hyperspectral satellite imagery.

Results achieved show that not only crop residues percent cover is linearly related to certain remote sensing-based indices, therefore making possible to estimate how well soil is preserved from weathering, but also that spaceborne hyperspectral sensors such as Hyperion appear to have great potentiality towards monitoring of other environmental targets due to their very high spectral and spatial resolution.

The research was deeply inspired by the outcomes of a European project ("Sustainable Agriculture and Soil Conservation through simplified cultivation techniques" - SoCo) aimed at improving protection of soil resources in the European agriculture sector through a stock taking and promotion of soil-friendly agriculture practices and systems, in particular simplified cultivation techniques, within the current legislative framework.

# *Introduction*

In Europe and elsewhere agriculture occupies huge portions of land, playing a fundamental role in the human society and in shaping the environment, while ensuring that the overall demand for food is adequately met [Louwagie et al., 2009a]. However, unsustainable agricultural practices and other land uses can have an adverse impact on natural resources such as soil, water and biodiversity. Furthermore, the current trend towards an ever growing world population and increased mechanization can contribute to worsen such negative impacts [Prosperi et al., 2011]. As a consequence, pressure is mounting on agriculture as well as on other human activities for a more sustainable management of natural resources and a better preservation of cultural landscapes [Louwagie et al., 2009b].

Despite the Common Agricultural Policy (CAP) and other pieces of European legislation now largely recognize and address the environmental challenges of the modern world, data indicate that soil degradation continues to be a widespread problem in agricultural soils across Europe [EEA, 2005]. This suggests that more needs to be done in order to tackle the problem. For this reason, the European Parliament launched in 2007 the "Soil Conservation and Sustainable Agriculture" project (SoCo[1]) aimed at studying and promoting soil-friendly agriculture techniques among farmers, as well as at generating useful proposals for future improvements to the CAP.

SoCo showed that soil erosion and decrease in organic matter are currently two of the most significant degradation issues in Europe. However, the use of Conservation Agriculture techniques, based on the provision of a permanent soil cover (crop residues, catch crops), the abandonment of inversion ploughing and the use of crop rotations, could greatly contribute to protection of soils from these threats [Louwagie et al., 2009a; Louwagie et al., 2009b]. In some member countries, conservation agriculture and other soil-friendly agricultural systems and practices are supported through CAP-based incentive mechanisms.

The release of a sufficient amount of crop residues on the soil surface, alone or in combination with the other conservation agriculture principles, appears particularly important for soil protection as repeatedly reported by literature in terms of multiple beneficial effects produced. The latter include [Nagler et al., 2003]:

- a significant decrease of erosion by reducing runoff volumes and the related movement of nutrients and pollutants into water bodies;
- an improvement of soil physical and chemical parameters, including a more stable soil structure, a better water infiltration through an augmented porosity and a reduced evaporation and soil temperatures;
- an effective conservation of nutrients into the soil that in turn reduce the need for fertilization regimes (including herbicide and pesticide application);
- an effective carbon sequestration.

Measuring the effects of such practices on the environment is therefore important for the protection of natural resources, modelling of erosion phenomena [Monty et al., 2008; Nagler et al., 2003; Nagler et al., 2000], as well as for legislation enforcement purposes, as illustrated below.

One possible way for measuring the above effects is to estimate crop residues cover on the soil after harvest. Literature is rich on methods for mapping crop residues in the field. However, these methods are expensive and likely to be impracticable on vast surfaces [Bannari et al., 2006]. Remote sensing can

1 SoCo (2007-2009) was initiated by the European Parliament and primarily executed by the Institute for Prospective Technological Studies (IPTS) and the Institute for Environment and Sustainability (IES) of the Joint Research Centre (JRC), in close cooperation with the Directorate-General for Agriculture and Rural Development (DG AGRI) of the European Commission and several other European partners. Web site: *http://soco.jrc.ec.europa.eu*

offer a valid alternative for monitoring large surfaces at once by exploiting the spectral response of the observed areas in different portions of the spectrum.

While the presence and quantification of green vegetation from remote sensing could always benefit from very distinctive absorption features of the chlorophyll in the Visible (VIS) and Near Infra Red (NIR) bands made available by popular sensors such as the Landsat series, it was not until recently that researchers discovered some specific spectral features of dry and senescent vegetation (lacking chlorophyll) that facilitated the differentiation between crop residues and bare soil [Bannari et al., 2006; Nagler et al., 2003]. This was made possible by technological advancements that now allow the simultaneous acquisition of image data in hundreds of narrow contiguous bands across broad regions of the electromagnetic spectrum through airborne or spaceborne sensors (hyperspectral remote sensing) in addition to more consolidated laboratory and field instruments [Bannari et al., 2006].

Against this background, inspired by the outcomes of the SoCo project, the present Ph.D. research intends to primarily contribute to the establishment and validation of possible methods, based on remote sensing techniques, for the determination of the effects of conservation agriculture on the environment. Focus of the research is the evaluation of a remote sensing based method for the quantification of the percentage cover of crop residues on the soil surface as a proxy for soil protection against erosion. Determination of the soil organic matter through chemometric[2] modelling and remote sensing was also attempted but could not be performed due to denied access to primary soil data.

A secondary objective of the present Ph.D. is also to demonstrate that scientific research can greatly benefit from the combined use of open source and/or freely available software and data.

The originality of such research relies in the use of hyperspectral satellite data for the quantification of soil litter, which, to my best knowledge, has never been attempted in Europe before. This, in turn, could potentially contribute to the assessment of the effectiveness of other agricultural practices on the environment.

In the remainder of this chapter, the conceptual background and scientific foundation behind the proposed research are explicitly illustrated, with a summary of the main degradation processes affecting the European soils, a compendium of the characteristics of conservation agriculture, information on remote sensing principles and possible methods for the achievement of the above mentioned objectives, and a sum-up of the current European legislation regarding agriculture and soil protection.

2 Chemometrics is defined as "*a chemical sub-discipline which deals with the application of mathematical, statistical and other methods employing formal logic to evaluate and to interpret (chemical, analytical) data; to optimize and to model (chemical, analytical) processes and experiments; to extract a maximum of chemical (and hence analytical) information from experimental data.*" [Einax et al., 1997]

# Soil and related degradation processes in Europe

Soil occupies the most superficial layer of the earth's crust. It is composed of a highly variable mixture of mineral particles, water, air and organic matter, comprising living organisms. Soil is a complex, mutable, living resource and one of the fundamental substrata for supporting life on the planet as it supplies plants and crops with a medium for growing and provides them with water and nutrients. Additionally, soil serves as a storage, filter, buffer and transformer of substances that are introduced into the environment, including water and gases. Soil also constitutes one of the richest biological habitats and gene pools on earth and provides a basis for human activities, landscape and heritage, as well as the supply of raw materials [Louwagie et al., 2009b; EC, 2005].

Soil is formed naturally over time as a consequence of physical, chemical and biological processes taking place on the geological and biological material. Such processes are strongly influenced by climate conditions, organisms, topography and human activities characterizing any given area. The richness and variety of soils on the earth reflects therefore the continued interaction of these factors with the parent material [EC, 2005].

Controversy exists between soil scientists on whether soil is a renewable resource or not [EC, 2005; Encyclopædia Britannica, 2011; Roose, 1996]. This largely depends on the value given to the amount of time and of disturbance under which the forming processes can operate. In many cases, it is observed that degraded soils can indeed be restored of their original ecological functions over a number of decades provided the process is not disturbed or interrupted [Encyclopædia Britannica, 2011].

Soil is therefore a fragile resource that needs to be preserved in order to perform its many functions. However, there is evidence that in many areas of Europe and beyond it is increasingly threatened by a range of human activities. In the European Union alone, an estimated 52 million hectares, representing more than 16% of the total land area, are affected by some kind of degradation. In the new Member States this figure rises to 35% [EC, 2005].

For these reasons, in 2006 the European Union institutions decided to protect soil in the same manner as water and air by developing a strategy to safeguard this vital resource. To this end, the European Commission, supported by the Council of Ministers and the European Parliament, developed and issued a Thematic Strategy for Soil Protection (COM(2006)231)[EC, 2005].

Six of the soil degradation processes recognised by the Thematic Strategy (water, wind and tillage erosion; decline of soil organic carbon; compaction; salinisation and sodification; contamination; and declining soil biodiversity) are closely linked to agriculture and present various degrees of risk across Europe. By 'risk' (of soil degradation) it is intended the occurrence of the underlying pre-disposing factors in a given area but it does not necessarily indicate the actual existence of degradative processes.

Erosion is a natural process that by means of meteorological phenomena, such as rain, wind, ice and temperature (freezing and thawing), wears down and shatters rock surfaces and detaches soil particles, displacing the weathered material. Erosion is therefore responsible, over geological timescales, for shaping the physical landscape and is an essential component of soil formation. With reference to soil, however, erosion can accelerate (becoming a degradative process) whenever the natural rate of particles removal is increased by human activities to a level that overcomes the natural formation of particles. Accelerated erosion can occur when certain soil parameters are modified, such as following a reduction or rapid change of soil cover (e.g. clearing of forests and conversion of rangelands or grasslands for cultivation, excessive grazing, controlled burning or wildfires, tillage), a change in the length or slope of the land surface, or as a consequence of a reduction of the infiltration capacity (e.g. as a result of compaction or reduction of the soil organic carbon content). Varying the intensity of land management can also influence the rate of erosion, for example through deep tillage, poor maintenance of terrace structures and inappropriate cultivation of steep slopes. Experts around the world consider soil losses in excess of 2 t/ha/yr irreversible within a timescale of 50-100 years [EC, 2005].

According to the Pan-European Soil Erosion Risk Assessment (PESERA), almost a quarter of Europe's land is estimated to be at some risk of erosion. Risk is defined as 'high' or 'very high' on 10 million hectares of Europe's lands and 'moderate' on a further 27 million hectares. The Thematic Strategy for Soil Protection further specifies that 'an estimated 115 million hectares or 12 % of Europe's total land area are subject to water erosion, and 42 million hectares are affected by wind erosion' (COM(2006) 231). Eroded soils are apt to suffer from supplementary degradation such as reduced efficiency in filtering pollution, in capturing water to replenish underground water reserves, or in storing the atmospheric carbon. The latter can contribute to further decrease the already low or very low organic carbon content in many lands in Europe and badly affects soil structure and biodiversity [Prosperi et al., 2011].

Soil water erosion and decline in soil organic matter content are two of the most widespread form of soil degradation in Europe, especially around the Mediterranean [Kirby et al., 2004; EC, 2006a; Louwagie et al., 2009b]. In agricultural areas, water erosion risk is usually high when adverse topography, low soil organic matter content, low percentage of vegetation cover, inappropriate farming practices, land marginalisation or abandonment, and high probability of intense rainfall events occur. In the Mediterranean region, such factors are often all present. Estimates indicate here a potential soil loss of 20-40 t/ha after a single downpour under the current average rates, with peaks exceeding 100 t/ha in extreme cases [Louwagie et al., 2009b].

Water (soil) erosion can cause a number of damages, both on-site (i.e. on the lands where erosion takes place) and off-site (i.e. on lands receiving the eroded material or its negative effects), as reported in the following Table 1. Many of such damages are directly or indirectly linked to the removal of soil organic matter (SOM), as explained below. Indeed, erosion can cause or contribute to organic matter decline and vice-versa.

| Kind of erosion | On-site damage | Off-site damage |
|---|---|---|
| Water | Loss of organic matter<br>Soil structure degradation<br>Soil surface compaction<br>Reduction of water penetration<br>Supply reduction to water table<br>Surface erosion<br>Nutrient removal<br>Increase of the coarse fraction of soil<br>Rill and gully generation<br>Plant uprooting<br>Reduction of soil productivity | Floods<br>Water pollution<br>Infrastructures burial<br>Obstruction of drainage networks<br>Changes in watercourses shape<br>Water eutrophication |

*Table 1: Potential on-site and off-site damages caused by soil water erosion.*
*Source: Louwagie et al., 2009b*

SOM is an extremely important component of soils, derived from the mixing of soil fauna and flora with the natural microbial biophysical degradation of dead organisms. The level of SOM content depends on two groups of factors: natural factors (such as soil type, climate - mainly temperature and precipitation - soil hydrology, land cover and/or vegetation and topography), and human-induced factors (land use, management and degradation). Climate alone explains the existence of a North-South climatic gradient, with high soil organic matter levels in the colder humid Northern part of Europe and

in mountainous areas and lower levels in the warmer semi-arid Southern part[3] [Louwagie et al., 2009b; EC, 2005; EC, 2011].

The amount of SOM affects soil's structure and in turn soil aeration and root capacity to penetrate the soil. SOM also improves water infiltration rates and water storage capacity, thus reducing run-off and erosion. Furthermore, SOM serves as a buffer against rapid changes in soil pH and sustaining soil micro-organisms contributes to soil biodiversity. Finally, SOM maintaining and optimising organic carbon levels (as a specific objective of land management) is an important contribution to climate change mitigation. Indeed, soil (organic matter) is at the same time an emitter of greenhouse gases and also a major storer of carbon, containing an estimated 1,500 giga tons of organic and inorganic carbon [Louwagie et al., 2009b; EC, 2005; EC, 2006b].

Much of these characteristics are explained by the composition of SOM, that is very rich in organic carbon [EC, 2011]. Soil Organic Carbon (SOC) is a very heterogeneous mixture of both simple and complex substances containing carbon (C) that includes all carbon-containing constituents like undecomposed organic vegetation residues, soil fauna and humus. Within the SOC, different pools based on composition and durability can be distinguished:

1. A labile pool: it is made of easily decomposable organic materials, including micro-organisms (many of which are involved in the actual decomposition and recycling processes), that only last from a few days to months in the soil. Such pool is an important source of food and energy for soil organisms and a source of plant nutrients (nitrogen and phosphorus). It also facilitates the stability of large soil aggregates.
2. A slow pool: it is made of well decomposed and stabilised organic materials (humus) that last many years in the soil. Humus is important for stabilising soil structure (micro- aggregates), improving water-holding capacity and retaining plant nutrients, e.g. cations.
3. An inert pool: it includes biologically very resistant organic materials that remain in the soil for thousands of years. These materials resemble charcoal (in chemical terms) and can retain cations, improving soil physical properties, due to their charge properties and porous nature.

Observations indicate that healthy soils contain all of the three pools above and well serve the different functions of the ecosystem. Therefore SOC is a good indicator of soil health [EC, 2005].

These functions and ecological services can be significantly impaired by a reduced SOM (SOC) content. Unfortunately, SOM is indeed on the decline in the European soils [EC, 2005]. An estimated 45% of European soils have low SOM (0-2% organic carbon) , principally in Southern Europe but also in areas of France, the UK and Germany [EC, 2006a]. A further 45% of soils have a medium content (2-6% organic carbon) [EC, 2005].

3 Climate drives decomposition rates as these increase with temperatures (by a factor of two to three for each 10 deg centigrade increase in temperature) and soil moisture (decomposition of organic matter requires oxygen and this is in short supply in waterlogged soils) [EC, 2005].

# Conservation Agriculture and crop residues for soil protection

This chapter describes the principles underpinning Conservation Agriculture and their expected environmental effects that lay behind the choice of this particular form of farming for the present research.

An effective protection of soil against degradation in agriculture is important to sustain production and to avoid the occurrence of off-site phenomena like water pollution and mud flows. The SoCo project identified numerous farming systems and practices that could help reducing or eliminating a number of degradation factors. The following were considered: conservation agriculture, organic farming, ridge tillage, contour farming, subsoiling, intercropping, maintenance of grasslands, agroforestry and conservation buffers [Louwagie et al., 2009a].

Conservation Agriculture (CA) addresses in particular the maintenance and improvement of soil resources while sustaining production. There is no agreement over a standardized international definition for CA, but the underlying techniques are commonly regarded as being underpinned by the following three principles:

- use of no-tillage or reduced tillage for seedbed preparation (instead of ploughing), in order to preserve soil organic matter;
- use of a permanent soil cover to protect the soil surface from weathering and contribute to the control of weeds;
- use of diversified crop rotations and associations to promote soil enriching micro-organisms while limiting plant pests and diseases [Prosperi et al., 2011; FAO, 2008].

More in detail, **no-tillage** (NT) is a cultivation technique consisting of a one-pass planting and, if needed, one fertiliser operation [Tripathi, 2009]. Soil and residues from the previous crop (mulch or stubbles) are minimally disturbed in order to keep soil constantly protected from weathering. The machines used are normally equipped with coulters, row cleaners, disk openers, in-row chisels or roto-tillers. These penetrate the mulch, opening narrow seeding slots (2-3 cm wide) or small holes, and place the seed and fertilisers into the slots [FAO, 2008]. Weed control is generally achieved with adapted crop rotations and/or herbicides [Gilliam, 2007]. The entire soil surface remains covered by mulch, or dead sod on more than 50% of the total surface.

**Reduced tillage** without inversion of soil strata represents all the practices situated between no-ploughing and no-tillage, regardless of the soil cover management. Reduced tillage can be deep or superficial and is usually used for different objectives: stubble breaking, mixing of crop residues with the topsoil, seedbed preparation, mechanical weed control and destruction of soil lumps (for example, after ploughing) [Louwagie et al., 2009b].

**Permanent soil cover** can be represented by any type of live or dead vegetation such as cover crops, green manure, catch crops or crop residues (mulches) and they are used to physically protect the soil surface from weathering. A **cover crop** is any crop grown to provide soil cover, regardless of whether it is later incorporated deep into the soil. Cover crops are grown primarily to prevent soil erosion by wind and water, but also to mobilize and recycle nutrients, improve the soil structure, permit a rotation in a monoculture, and control weeds and pests [FAO, 2008]. **"Green manuring"** involves the incorporation into the soil of any field or forage crop while green or soon after flowering, for the purpose of soil improvement. Cover crops and green manures can be annual, biennial, or perennial herbaceous plants grown in a pure or mixed stand during all or part of the year. In addition to providing ground cover and, in the case of a legume, fixing nitrogen, they also help suppress weeds and reduce insect pests and diseases. **Catch crops** are cover crops planted to reduce nutrient leaching

following a main crop [NCAT, 2009]. **Mulches**, or **crop residues**, are a valid alternative to cover crops or green manuring and have the advantage to save on costs for mechanical operations and seed purchase [Prosperi et al., 2011]. The importance of retaining crop residues on the soil surface is highlighted by several studies [Lal, 2003; IAEA, 2003; Nagler et al., 2003; Anderson and Magleby, 1997; Verhulst et al., 2011]. On-site benefits or ecosystems services provided by crop residues include the following:

- improved soil physical (e.g., structure, water infiltration rate, water capacity), chemical (e.g., nutrient cycling, cation exchange capacity, soil reaction), and biological qualities (e.g., Carbon sequestration - both as SOC and microbial biomass - , biodiversity);
- reduction of soil erosion and in decreasing losses of water by surface runoff and evaporation;
- improved agronomic productivity and profitability when crop residues are used in conjunction with CA principles.

Off-site benefits include:

- improvement of quality of water and air through reduction in erosion (water and wind), non-point source pollution, sedimentation, and transport of pollutants into the water bodies and aquatic ecosystems;
- reduction in frequency and intensity of floods with consequent reduced damages to infrastructure (e.g., highways, bridges, waterways) and tourism;
- improvement in productivity of aquaculture and agricultural systems in the flood plains as runoff of water, sediments and pollutants are reduced.

In some countries (notably in the USA), the amount of crop residues left on soil surface after harvesting is used as a discriminating factor of CA versus conventional farming based on ploughing [Daughtry et al., 2006]. Tillage is ranked as intensive if percent of crop residues cover is lower than 15%, reduced with 15–30% residue cover and conservative with more than 30% residue cover. The presence of a crop residues amount greater than 15% can therefore be considered as a distinctive feature of conservation agriculture based systems. However, under the current European legislative framework that supports the use of residues even in conventional farming, it is doubtful that the sole presence of residues may be used as a criterion to map conservation agriculture distinctively from other forms of farming.

**Crop rotation** is a planned system of growing different kinds of crops in recurrent succession on the same land. This is done to obtain various benefits, such as to avoid the build up of pathogens and pests that often occurs when a single species is continuously cropped [Miller et al., 2010], and one of the primary motivations for organic farmers to apply crop rotations [Kroeck, 2011]. Over time, crop rotation influences therefore insect, weed, and disease pressure as well as soil nutrient status by balancing the fertility demands of various crops, that avoids excessive depletion of soil nutrients. Furthermore, it affects soil physical condition by alternating deep-rooted and shallow-rooted plants [Grubinger, 1999; Miller et al., 2010].

The above information highlight that CA can be an effective farming system in addressing soil degradation and that a consistent part of the benefits deriving from its application, as reported in literature, can be attributed to the prescribed use of a permanent soil cover in one of the possible forms, including crop residues. Therefore, monitoring the amount of crop residues on the soil surface could represent a valid proxy indicator for the assessment of the protective effects of CA on the soil.

# European Legislative Framework

Agriculture is one of the most widespread human activities in terms of surface utilised. In Europe and elsewhere, it occupies vast portions of land, playing a fundamental role in shaping the environment while ensuring that the overall demand for food is adequately met [Louwagie et al., 2009a]

However, unsustainable agriculture practices and other land uses can have adverse impacts on natural resources such as soil, water and biodiversity. Furthermore, an ever larger world population and increased mechanization can contribute to worsen such impacts. Soil degradation is already considered a widespread problem in Europe, particularly in agricultural areas [EEA, 2005]. As a consequence, pressure is growing on agriculture as well as on other activities for a more sustainable management of natural resources and a better preservation of cultural landscapes [Louwagie et al., 2009b].

In recognition of these facts and of the profound changes occurred in the market, industry, regulatory and societal conditions in recent times, the European Institutions have responded with a series of initiatives and reforms of the Common Agricultural Policy (CAP) and other pieces of legislation. CAP's cross-compliance mechanism grants support to farmers who respect a minimum set of environmental standards as provided for in the Good Agriculture and Environmental Condition (GAEC[4]) and Statutory Management Requirements (SMRs[5]) regulations.

GAECs address the preservation of soil resources by setting a European framework of standards that include tackling of soil erosion as well as of soil organic matter loss and maintenance of a good soil structure (Table 1). Compulsory actions include the use of minimum soil cover and proper management of arable stubbles, whereas state-specific and optional rules include standards on crop rotations and appropriate use of machinery. GAEC standards are detailed by the single national authorities and in some countries include the release of crop residues on the surface and the use of no- or reduced-tillage.

SMRs include 23 pieces of legislation extracted from several Directives in the field of environment, public, animal and plant health, and animal welfare[6]. Some of these may have an impact on soil resources.

The rural development mechanism and its agri-environmental schemes offer additional financial assistance to farmers who commit to preserve the environment beyond the minimum baseline established by cross-compliance.

Recent research indicates that conservation agriculture, while well fitting within the current legislative framework, particularly on the provision of a permanent soil cover, the abandonment of inversion ploughing and the use of crop rotations, could greatly contribute to the maintenance and improvement of soil resources [Louwagie et al., 2009a; Louwagie et al., 2009b]. In some member countries, conservation agriculture is also financed as an agri-environmental measure.

4 Council Regulation (EC) 73/2009, Annex III

5 Council Regulation (EC) 73/2009, Annex II

6 For more information: http://eur-lex.europa.eu/LexUriServ/LexUriServ.do?uri=OJ:L:2009:030:0016:0099:EN:PDF Annex II.

| Issue | Compulsory standards | Optional standards |
|---|---|---|
| Soil erosion:<br>Protect soil through appropriate measures | — Minimum soil cover | — Retain terraces |
| | — Minimum land management reflecting site-specific conditions | |
| Soil organic matter:<br>Maintain soil organic matter levels through appropriate practices | — Arable stubble management | — Standards for crop rotations |
| Soil structure:<br>Maintain soil structure through appropriate measures | | — Appropriate machinery use |
| Minimum level of maintenance:<br>Ensure a minimum level of maintenance and avoid the deterioration of habitats | — Retention of landscape features, including, where appropriate, hedges, ponds, ditches trees in line, in group or isolated and field margins | — Minimum livestock stocking rates or/and appropriate regimes |
| | | — Establishment and/or retention of habitats |
| | — Avoiding the encroachment of unwanted vegetation on agricultural land | — Prohibition of the grubbing up of olive trees |
| | — Protection of permanent pasture | — Maintenance of olive groves and vines in good vegetative condition |
| Protection and management of water:<br>Protect water against pollution and run-off, and manage the use of water | — Establishment of buffer strips along water courses (1) | |
| | — Where use of water for irrigation is subject to authorisation, compliance with authorisation procedures | |

(1) Note: The GAEC buffer strips must respect, both within and outside vulnerable zones designated pursuant to Article 3(2) of Directive 91/676/EEC, at least the requirements relating to the conditions for land application of fertiliser near water courses, referred to in point A.4 of Annex II to Directive 91/676/EEC to be applied in accordance with the action programmes of Member States established under Article 5(4) of Directive 91/676/EEC.

*Table 2: Good agriculture and Environmental Condition framework rules currently in force. After Council Regulation (EC) 73/2009, Annex III (CAP Health Check).*

The monitoring of SMRs and of GAEC standards is central to the cross compliance as much as it is the monitoring of agri-environmental measures for the rural development schemes. Standards need to be verifiable in order to implement proper monitoring and enforcement measures. Two basic monitoring approaches are commonly distinguished: direct, on-the-ground checking of the respect of requirements, and the use of indicators reflecting outputs or results [Louwagie et al., 2009b]. However, remote sensing can also greatly contribute to these goals provided that the action performed (and the environmental effect) are proved to be linked and can effectively be observed from distance.

# Remote sensing

Remote Sensing refers to techniques that acquire data or information about objects not in contact with the viewing instrument (sensor) [Short, 2011]. Sensors can be portable or be mounted on a "platform", like an aeroplane or a satellite. Sensors are devices capable of detecting and recording the electromagnetic radiation reflected or emitted by the objects observed. In this sense, our own eyes or even the common portable cameras we all use for our holiday photos are effectively remote sensors as they acquire radiation in the visible portion of the electromagnetic spectrum as reflected by the observed objects [Levin, 1999].

The electromagnetic radiation is a form of energy that propagates at the speed of light as a double sinusoidal wave (electric+magnetic) perpendicularly to the direction of travelling. The distance between two crests of the wave is called wavelength ($\lambda$) and it is measured in metres (m) or in one of its sub-factors such as nanometres (nm, $10^{-9}$ metres), micrometres ($\mu$m, $10^{-6}$ metres) or centimetres (cm, $10^{-2}$ metres) [CCRS, 2007]. "Wavelength" is directly linked to "frequency" ($\nu$) through the equation: $c = \lambda \nu$ where:

- c represents the speed of light ($3 \cdot 10^8$ m/s);
- $\lambda$ is in m;
- $\nu$ is in cycles per second (Hz).

Therefore, the shorter the wavelength, the higher the frequency.

The range of wavelength detected and the ability to segregate different wavelengths depends on the inner nature of the sensor, that is on its "spectral resolution". Human eyes, for example, can only detect the "visible" portion of electromagnetic spectrum ($\lambda$ = 0.4-0.7 $\mu$m) and can usually detect differences only between well defined hues.

Remote Sensing imagery is affected by various forms of distortion, usually grouped in two basic categories: *geometric* and *radiometric*.

**Geometric distortions** can occur as a consequence of the perspective of the sensor optics, the motion of the scanning system (if present), the position and motion of the platform (altitude, attitude, and velocity), the terrain relief and the curvature and rotation of the Earth [CCRS, 2007]. While some of these, namely the terrain relief, are random and can only be reduced, others are systematic and can be precisely modelled for removal. Geometric corrections attempt therefore to eliminate or reduce these distortions so that the geometric fidelity of the imagery with the real world is as high as possible. Random distortions are usually removed via geometric registration of the image to known ground coordinates. One of the possible methods to do so is by identifying several image features (i.e. the corner of a building, a crossroad, etc.) called Ground Control Points (GCPs) both on the distorted image and onto a georeferenced image (image-to-image correction) or map (image-to-map correction) and registering the respective coordinates. Computer software is then able to calculate the mathematical (polynomial) relationship between the corresponding GCPs coordinates and, through it, to geometrically correct (or georeference) the distorted image. Polynomial order is usually user defined. Order 1 indicates a simple linear shift (translation), a rotation or a scale of the whole raw image and is usually good for flat areas; Order 2 (quadratic) and 3 (cubic) indicate more complex warping useful for undulated or mountainous areas. Georeferenciation with GCPs is suitable where the area is largely flat and the imagery has been acquired from nadir (near vertical) viewing. However, if image acquisition has occurred at a high angle to the vertical, or very high accuracy is required, or the imaged area shows an undulating topography, ortho-rectification is necessary [GeoImage, 2010]. Ortho-rectification is also usually required if several images or scenes need to be mosaicked seamlessly. Ortho-rectification is basically a geometrical correction process that takes the vertical aspect into account and by which relief

apparent displacement (due to the imaging geometry) is rectified through incorporation of a digital elevation model (DEM). Ortho-rectification makes use of mathematical equations that link the distorted pixels with the true location (Rational Polynomial Coefficients, or RPCs, provided by the sensor launcher) and optionally of Digital Elevation Models (DEMs) of the area of interest.

Whenever geometric correction is performed, the original pixels do not precisely overlap with the new ones. Therefore, in order to attribute the correct digital value to the new pixels, a resampling method has to be chosen between those available. With nearest neighbour, the new pixel in the corrected image takes the digital value from the nearest pixel in the original image; with bilinear interpolation, the new pixel takes a weighted average of four nearest pixels in the original image; finally, with cubic convolution, the new pixels' value is the average of the nearest sixteen pixels [CCRS, 2007]. The advantage of the first method is that it retains the original value of pixels. However, such values can be duplicated, resulting in a "blocky" image. Bilinear interpolation and cubic convolution have the disadvantage to generate new pixel values, but offer a much sharper resulting image.

**Radiometric distortions** pertain to image issues due to variations in scene illumination and viewing geometry, atmospheric conditions or sensor noise and calibration (response). These distortions are specific of the sensor and platform used to acquire the data and of the conditions during image acquisition [CCRS, 2007]. Similarly to the previous case, radiometric corrections intend to eliminate or reduce the influence of distortions on the true values of reflectance of the observed objects. Depending on the degree of pre-processing of the imagery distributed by the provider, radiometric correction may or may not be needed.

Whenever the source of radiation is the sun, sensor is referred to as "passive". Vice-versa, if the source of radiation is the sensor itself, the latter is referred to as "active".

Active sensors operate in the microwaves (low frequency) domain (0.3-40 GHz), with wavelengths of 0.01-1 m. At these wavelengths, no interaction (absorption, deviation, reflection) of the radiation emitted by the sensor with the much smaller atmospheric gaseous particles, including water vapour, occurs. Therefore, active sensors can observe the earth surface even under a thick cloud cover.

Passive sensors, instead, are deeply affected by the atmosphere because the detected radiations present much smaller wavelengths, similar to those of the gases traversed. In this case, radiation is completely masked by cloud cover, but, even with clear sky, it variously suffers from absorption and scattering phenomena [Levin, 1999]. Therefore, imagery acquired by passive sensors usually requires a careful cleaning, or atmospheric correction, of the "at sensor" or "Top Of the Atmosphere" (TOA) radiance from the influence of atmospheric elements. The result of atmospheric correction is an image containing the reflectance of the surface materials detected [Gao et al., 2007].

Atmospheric correction models are generally grouped into two basic categories (Figure 1).

The first includes empirical or relative models, that require the spectral reflectance of reference objects to be accurately known. Relative methods use input information from the image itself without considering the atmospheric components and rely on the assumption that for one image (band/channel) the relation between the radiances at TOA and at ground level follows a linear trend. Yet, given the variety of earth features present in a satellite image, the trend is rarely linear. However, linearity can be considered precise enough to solve practical applications where there are other more important source of errors. These methods are useful when there is very little information about the ground.

The second category includes the physics based absolute methods, that require a description of various properties of the atmospheric profile, such as the amount of water vapour and the distribution of aerosols. Direct measurements of these properties are usually unavailable. However, techniques have been developed for hyperspectral image data that derive atmospheric properties from their imprint on the measured radiance. Inferred values are then used to constrain highly accurate atmospheric radiation transfer[7] models to produce an estimate of the true surface reflectance. [Kawishwar, 2007; ITT VIS, 2011b]

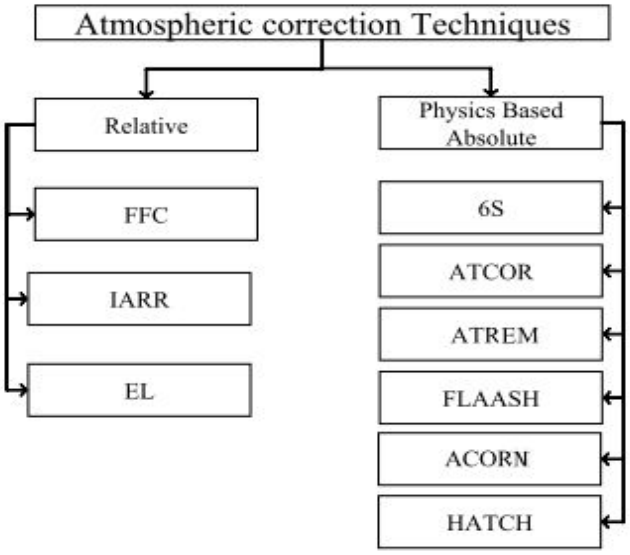


*Figure 1: Atmospheric correction techniques subdivided by category of approach. (Modified from: Kawishwar, 2007)*

A brief overview of the methods included in each category is presented hereafter.

Relative methods:

- The Flat Field Correction (FCC) method assumes that there is an area in the scene that shows little variation with wavelength (flat = neutral reflectance). The mean spectrum of such an area is then used to derive the relative reflectance spectra of other areas in the scene. [Gao et al., 2007]
- The Internal Average Relative Reflectance (IARR) correction method normalizes images to a scene average spectrum by calculating the average spectra value of the image and then by dividing each pixel's spectra value by the average spectra value in order to produce the relative reflectance spectra. [Kayadibi, 2011]. This is particularly useful in areas where no ground measurements exist and little is known about the scene. However, it works best for arid areas with no vegetation. [ITT VIS, 2011a]
- The Empirical Line Method (or Calibration) (EL) assumes that reflectance of target points is measured on the image and on the ground with a field spectrometer. The image reflectance in each band is then compared with the ground-measured reflectance and linear equations are developed to predict the true reflectance for each waveband. These equations are then applied to the remotely sensed data to produce images where both illumination and atmospheric effects are removed. [Xu and Huang, 2007]

Absolute methods:

7 Radiative Transfer Theories explain how radiation and matter interact from a mathematical point of view, like light with the atmosphere, generating absorption, emission and scattering processes [Drusch, 2005].

- 6S (Second Simulation of Satellite Signal in the Solar Spectrum) is a model based on the radiative transfer theory that takes the main atmospheric effects into account. The use of the 6S model for simulating the atmospheric scattering process assumes that a number of atmospheric correction parameters are chosen, in which aerosol optical thickness and elevation have a greater impact on the results of atmospheric correction [Xie et al.,2010 ].

- ATCOR (Atmospheric Correction for Flat and Rugged Terrain) indicates a number of models based on a large database of radiative transfer calculations from the MODTRAN-5[8] model. The underlying radiative transfer codes simulate the reflectance image by taking into account sun-sensor geometry at the time of imaging, temperature water vapour and gases concentrations profiles, aerosol type and concentration, spectral variation of ground reflectance and availability of bands in absorption regions.

- ATREM (Atmosphere REMoval Program) was developed by the University of Colorado for retrieving scaled surface reflectance from hyperspectral data that uses the 6S radiative transfer model. However, it is not distributed anymore.

- FLAASH (Fast Line-of-sight Atmospheric Analysis of Spectral Hypercubes) is a MODTRAN4 based model. One key feature of FLAASH is that it offers the option of correcting for light scattered from adjacent pixels into the field-of-view.

- ACORN is another MODTRAN4 based model to retrieve surface reflectance without ground measurements. A key feature of ACORN is that it implements a full spectral fitting technique to model for the overlap of absorption bands between water vapour in the atmosphere and liquid water in surface vegetation. ACORN also contains several artifact suppression options, including automated wavelength adjustment, elimination of noisy channels and correction (or "polishing") of residual reflectance spectral errors.

- HATCH was developed at the University of Colorado and is available through a license agreement. It uses the correlated k-method, which allows improved transmittance calculations in regions where multiple gases absorb strongly. HATCH uses a spectrum-matching technique to retrieve column water vapour amount. It also allows automatic spectral calibration of the sensors based on a "smoothness test".

Some researchers have attempted comparisons between some of the above models. Kruse, 2004, evaluated the performance of ATREM, ACORN and FLAASH models using low-altitude AVIRIS[9] data and concluded that they produce comparable atmospheric correction results. ATREM, as well as ACORN, provides a basic level of correction though ACORN also enhances correction for liquid water determination, shows some control over the underlying MODTRAN options, and offers additional multispectral correction capabilities. FLAASH provides basic corrections with enhanced corrections for adjacency effects and is most flexible for correction of hyperspectral data in light of available MODTRAN options [Kruse, 2004].

With regard to the image acquisition mechanisms, two fundamental types of sensor are distinguished: *pushbroom* or *wiskbroom*.

Pushbroom sensors collect the incoming radiation through a series of lines of sensors (one line for each band) arranged perpendicular to the flight direction of the spacecraft (or aeroplane). Different

8 MODTRAN (Moderate Resolution Transmittance) model calculates atmospheric transmittance and radiance for frequencies from 0 to 200 nm at moderate spectral resolution of 0.0001 μm. MODTRAN was developed for higher spectral resolutions for molecular band parametrization, spherical refractive geometry, solar and lunar source functions, scattering (Rayleigh, Mie, single and multiple), and default profiles (gases, aerosols, clouds, fogs, and rain) [Kneizys et al., 1996].

9 AVIRIS - Airborne Visible / Infrared Imaging Spectrometer – a NASA airborne hyperspectral sensor.

areas of the surface are recorded as the spacecraft moves forward along its orbit. This means that in the resulting image (band), each along-track column shows values as imaged by only one detector and each across-track row is imaged by an entire line of detectors at any given time. Comparatively, wiskbroom sensors use only one detector per image (i.e. per band). The scanning of the across-track direction of the image is obtained by mechanical oscillation of a mirror (Figure 2), whereas the advancement in the along-track direction, very much like the pushbroom sensors, is given by the forward movement of the satellite.

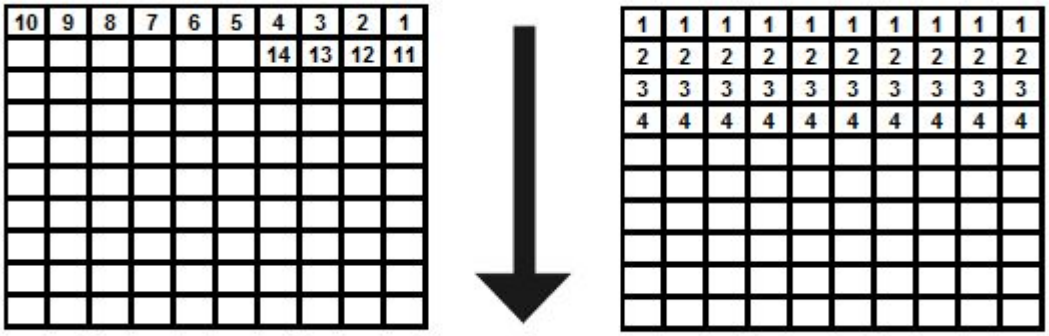


*Figure 2: Image acquisition mechanism in pushbroom and wiskbroom sensors. Wiskbroom sensors (left) acquire images one pixel at a time per image (band) in the indicated sequential order. Scanning of pixels in a row is given by an oscillating mirror integrated with the detectors. Pushbroom sensors (right) compose the image row by row (one line of detectors per image/band) in the indicated order. No mechanical scanning is needed. The central arrow represents the satellite's direction of movement, that coincides with the along-track direction of the image.*

Airborne or satellite sensors can acquire images remotely for mapping and monitoring the natural and man-made features on the land surface. Appropriate interpretation and analysis of such imagery requires a deep understanding of the processes that link the property actually measured by the sensor and the surface properties of interest [Smith, 2006].

# *Materials*

The computer phase of the present research was entirely developed on a Windows Vista Home Premium based HP Pavillon dv6700 laptop (processor Intel Core 2 Duo T9300 @ 2,50 GHz). Part of the image data processing was carried out on a Linux - Portable Ubuntu (version TRES) application (a sort of a virtual machine) running inside Vista. Other individual software and material used is specified below.

## Study area

The study area coincides with part of the Bianchini farm, that occupies five different areas in the provinces of Lodi and Milan. For the present research, a selection was operated, limiting the analysis to the two portions of farm in the province of Lodi, municipalities of San Martino in Strada and Lodivecchio due to their extensive surface and closeness. Such limitation was required to account for the characteristics of the satellite imagery and the acquisition constraints.

The farm was selected because is one of the biggest in Northern Italy among those that apply conservation agriculture principles. The Bianchini farm uses both no-tillage and minimum tillage on more than 500 hectares. Consistently with the dominating farming systems of the region, the Bianchini farm's produce include durum wheat, tender wheat and corn, and in minimal part soya and other crops. Crop planning is established year by year on the basis of the expected market demands. Corn is generally followed by wheat and then by a natural regrowth of grass. No other forms of rotation were observed during the study and the tabular data collected do not suggest that any such practice is in use at the Bianchini farm nor is any form of seeded cover/catch crops in between the main crops.

All the parcels in the Lodivecchio and San Martino areas show a flat terrain.

Soils in the two areas are predominantly Luvisols (Figure 3), with limited portions of Gleysols and Regosols. Luvisols occur mainly in temperate regions, particularly in areas with a Mediterranean-type of climate [ISRIC, 2011], and "are soils that have a higher clay content in the subsoil than in the topsoil as a result of pedogenetic processes (especially clay migration). […] Most Luvisols are fertile soils and suitable for a wide range of agricultural uses. Luvisols with a high silt content are susceptible to structure deterioration if tilled when wet or with heavy machinery. Luvisols on steep slopes require erosion control measures." [FAO, 2006].

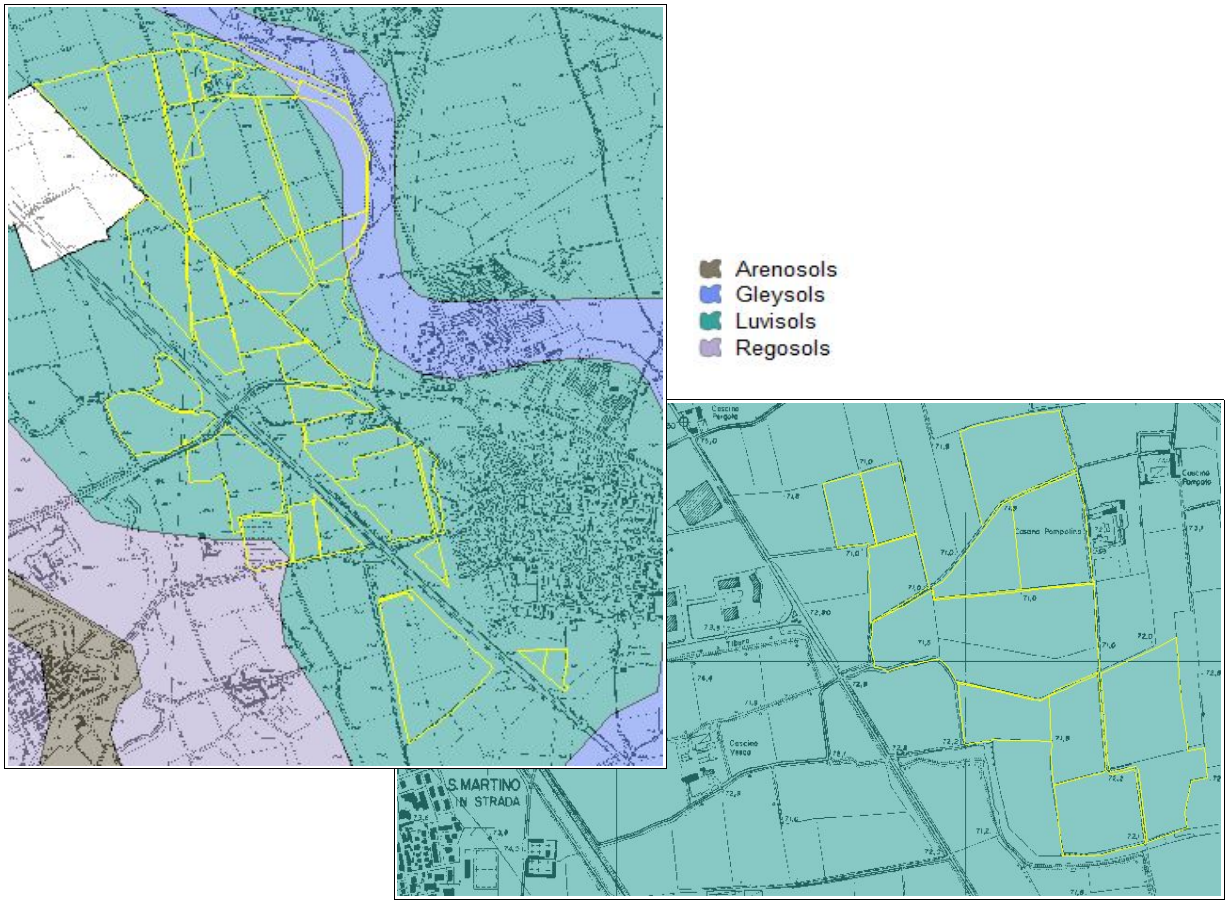


*Figure 3: The Bianchini farm superimposed to the pedological and the regional technical (CTR) map of Lombardia. Left: the Lodi Vecchio portion of the Bianchini farm. Right: the San Martino in Strada portion of farm. Source of data: pedological map [Regione Lombardia, 2011]; CTR [Provincia di Lodi, 2011].*

Climate in the study area can be defined by use of the Köppen-Geiger map [Kottek et al., 2006] and corresponds to the "Warm temperate climate, fully humid, with a hot summer" class. Such class is coded as *Cfa* and defined according to the following criteria (Table 3).

| Type | Description | Criterion |
|---|---|---|
| **C** | **Warm temperate climates** | $-3\ ^{\circ}C < T_{min} < +18\ ^{\circ}C$ |
| Cs | Warm temperate climate with dry summer | $P_{smin} < P_{wmin}$, $P_{wmax} > 3\,P_{smin}$ and $P_{smin} < 40$ mm |
| Cw | Warm temperate climate with dry winter | $P_{wmin} < P_{smin}$ and $P_{smax} > 10\,P_{wmin}$ |
| Cf | Warm temperate climate, fully humid | neither Cs nor Cw |
| a | Hot summer | $T_{max} \geq +22\ ^{\circ}C$ |

*Table 3: Criteria defining the Köppen-Geiger climatic class for the study area.*
*$T_{max}$ and $T_{min}$ indicate the monthly mean temperatures of the warmest and coldest months respectively. $P_{min}$ is the precipitation of the driest month.*
*$P_{smin}$, $P_{smax}$, $P_{wmin}$ and $P_{wmax}$ are defined as the lowest and highest monthly precipitation values for the summer and winter half-years on the hemisphere considered. All monthly precipitations are given in mm/month.*
*Source: Kottek et al., 2006*

Köppen classification was inspired by observation that plants are indicators for many climatic elements. Köppen distinguished between plants of the equatorial zone (A), the arid zone (B), the warm temperate zone (C), the snow zone (D) and the polar zone (E). As further criteria for climate classification, he considered the precipitation and the air temperature [Kottek et al., 2006].

In order to carry out the present Ph.D. research, the following data were collected from the Bianchini farm management:

- digital map (in DXF format) of all the farm's cadastral and cultivated parcels (with positional attributes: cadastral parcels' and sheets' codes, topological names);
- spreadsheet (in XLS format) containing the type of crops cultivated, dates of seeding, harvesting and type of treatments, subdivided per parcel (by name);
- spreadsheet (in paper format) with information linking parcels' names to cadastral parcels' codes.

In order to convert the farm's cadastral digital map to a fully featured vector map (in SHP format), additional data related to the study area were retrieved (and elaborated) from other sources, namely from the on-line Web Mapping Services – WMS – repository of the province of Lodi:

- cadastral map (in WMS format) of the whole Province of Lodi for the retrieval of parcels codes [Provincia di Lodi, 2011];
- aerial orthophotos (in WMS format) for the checking of the actual shape of agricultural parcels [Provincia di Lodi, 2011].

Furthermore, 2007 WMS aerial orthophotos (TerraItaly) from Provincia di Lodi, 2011, were used for the georeferenciation of Hyperion imagery, after pre-processing for radiometric (atmospheric) defects. The pedological map [Regione Lombardia, 2011] and regional technical map (CTR) [Provincia di Lodi, 2011] were downloaded from the respective sources and used for reference.

## Hyperion

Hyperion is a hyperspectral pushbroom sensor aboard the Earth Observing (EO-1) satellite, launched by the National Aerospace and Satellite Agency (NASA) of the United States on November 21, 2000 as part of a one-year technology validation/demonstration mission.

EO-1 also hosts the Advanced Land Imager (ALI) multispectral instrument which was used to validate and demonstrate technology for the Landsat Data Continuity Mission (LDCM) during the original EO-1 Mission, successfully completed in November 2001. The remote sensing research and scientific community's high interest in a continued acquisition of image data from both the ALI and Hyperion sensors, however, prompted NASA to extend the EO-1 Program initial mission.

The EO-1 Extended Mission now collects and distributes ALI and Hyperion products in response to user generated Data Acquisition Requests (DARs). Under the Extended Mission provisions and based on an agreement with the United States Geological Survey (USGS), image data acquired by EO-1 are archived and distributed by the USGS Center for Earth Resources Observation and Science (EROS) and placed in the public domain.

Each registered user can therefore fill in an on-line DAR form to request acquisitions of images from ALI, Hyperion or both, free of charge. Nadir/non nadir pointing can also be specified. The latter implies that each acquired scene has its own orientation and degree of distortion, which must be

accounted for.

Limitations in the use of the service are in place so that only one request (one DAR) per user is allowed each week and no guarantee is granted that acquisitions will actually occur, depending on the number of conflicting requests received at the same time and on the planned path/row pointing. Acquisitions can also be affected by cloud cover depending on the local meteorological conditions.

Hyperspectral sensors, compared to multispectral, normally comprise hundreds of bands with a narrow bandwidth (at Full Width Half Maximum – FWHM).

Hyperion is capable of resolving 242 spectral bands (from 0.4 to 2.5 μm) with a 30-meter geometric resolution and a 10 nm spectral resolution. "The instrument can image a 7.5 km by 100 km land area per image, and provide detailed spectral mapping across all the channels with high radiometric accuracy. The major components of the instrument include the following:

- System fore-optics design based on the Korea Multi-Purpose Satellite (KOMPSAT) Electro Optical Camera (EOC) mission. The telescope provides for two separate grating image spectrometers to improve signal-to-noise ratio (SNR).
- A focal plane array which provides separate Short Wavelength Infrared (SWIR) and Visible and Near Infrared (VNIR) detectors based on spare hardware from the LEWIS HSI program.
- A cryocooler identical to that fabricated for the LEWIS HSI mission for cooling of the SWIR focal plane.

Hyperspectral imaging has wide ranging applications in mining, geology, forestry, agriculture, and environmental management. Detailed classification of land assets through the Hyperion enables more accurate remote mineral exploration, better predictions of crop yield and assessments, and better containment mapping" [USGS, 2011].

Hyperion images exhibit a number of artefacts caused by calibration and positioning imperfections in the detector arrays [Goodenough et al., 2003; Dadon et al., 2010], atmospheric interference [Gao et al., 2006] and improper geospatial registration. In order to study surface properties using imaging spectrometer data, accurate removal of atmospheric absorption, scattering effects and other distortions is required for the conversion of radiances measured by the sensors to reflectances of surface materials [Gao et al., 2006].

The atmosphere elements and the observed surface deeply absorb and scatter[10] the solar radiation on the sun-surface-sensor ray path. Water vapour is responsible of some major absorptions centered at approximately 0.94, 1.14, 1.38 and 1.88 μm, while oxygen absorbs at 0.76 μm, and carbon dioxide at around 2.08 μm. Of the entire spectrum covered by Hyperion, nearly half is affected by atmospheric gas absorptions, whereas the wavelength region below 1μm is also affected by molecular and aerosol scattering [Gao et al., 2006]. Figure 4 displays the atmospheric transmission (opacity) windows. Waldhoff et al., 2008, created a similar image along with a comparison of Hyperion bands with those of the ASTER and Landsat ETM+ sensors.

Out of the 242 theoretically available bands acquired by the sensor, only 198 were calibrated by USGS and can be actually used (bands 8-57 and 77-224). The other bands are automatically set to zero during the calibration processing done by USGS prior to distribution, although they remain included in the file.

Image data is distributed as signed integer at 16 bits (INT16). A differential scaling factor is applied to the calibrated radiance ($W/m^2$-sr-μm). More in detail, a factor of 40 is applied to spectral bands 1-70, and a factor of 80 is applied to spectral bands 71-242 [Barry, 2001].

10 Scattering is the deviation of a radiation from the straight direction, due to interaction with some physical elements, such as the atmospheric gaseous particles and dust.

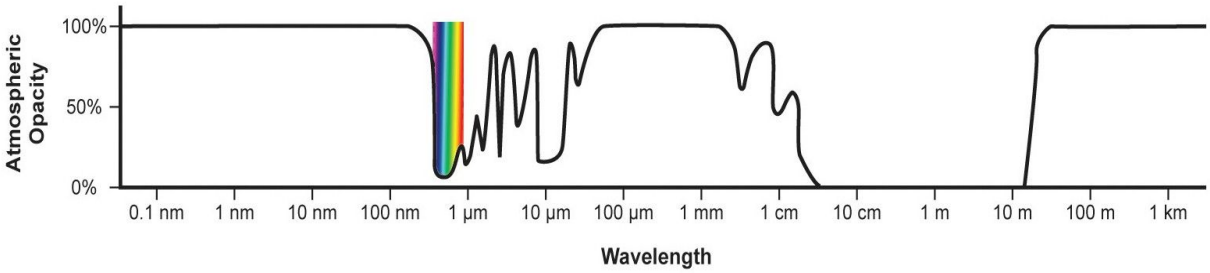


*Figure 4: The atmospheric opacity diagram.*
*(Source: NASA, 2011)*

Hyperion was chosen due to its very interesting characteristics in terms of width of the wavelength detected and the high geometrical resolution achieved. Furthermore, Hyperion is the only hyperspectral space-borne sensor currently available on the market and one of the few whose imagery is in the public domain.

# *Methods*

This Ph.D. study was initially driven by the need to acquire knowledge on existing methods for the analysis of the effects of agriculture practices on the environment through remote sensing.

In this respect, a thorough analysis of the available literature allowed to identify some methods that appeared useful to the scope of the research. Given the current status of the scientific knowledge and the present availability of satellite data on the market, three major objectives were selected as feasible by use of remote sensing techniques:

1. the determination of changes in soil organic carbon (SOC) as a consequence of the continued application of conservation agriculture practices;
2. the detection of lands under conservation agriculture as opposed to those under traditional mouldboard tillage;
3. the determination of soil cover by residues as a proxy for the estimation of the protective capability of the farming practice used.

The determination of changes in SOC through remote sensing techniques (point 1 above) appeared immediately of great interest as the decrease in SOC is one of the major soil degradation phenomena in Europe. Furthermore, remote sensing shows potential for application over vast territories. A consistent amount of time and efforts were therefore dedicated to the development of this research that would make use of a mixture of chemometric techniques, soil sampling data and complex statistical processing.

Unfortunately, though, this research had to be interrupted because of the unavailability of some fundamental soil and spectroscopic data. Details on the scientific foundation, the logical reasoning and the material collected during the research are now part of the Annex I in the present report, in the hope that they could be useful to other researchers and that the above soil data will be available in the future.

The detection of land under conservation agriculture through remote sensing (point 2 of the above list) would also be of relevant interest as the extent to which conservation agriculture is applied worldwide is only estimated through proxy data.

Various authors report of successful attempts in correctly determining small areas under CA mostly through use of optical sensors imagery, such as Landsat. However, the variety of forms in which conservation agriculture techniques are applied, which often tend to be mixed with traditional cultivation practices, make the remote sensing techniques rarely applicable to vast areas and imply that a thorough field check is applied to the results.

Like in the previous case, the information and knowledge collected for the determination of the feasibility of this research are now part of the Annex II to the present report.

Because of the above considerations, final decision was taken to pursue the research and evaluation of remote sensing methods for the determination of soil cover by crop residues. Such topic will be treated in depth in the remainder of the present document.

# GIS data processing

The geospatial data collected for the study area needed a significant amount of pre-processing before they could actually be used. Indeed, the original farm's cadastral map was not it a GIS-ready format and appeared to have only an indirect link with the other farm's tabular data through the parcels' names/cadastral codes table.

As a first step, therefore, the cadastral map was converted from the native DXF format to a geographical shapefile (SHP) format through the "Dxf2Shp converter" plugin in Quantum GIS (QGIS, v.1.6.0) [QGIS, 2011]. Projection information was missing in the DXF file and, as a consequence, also in the derived shapefile. However, by overlay with the on-line cadastral WMS map of the Province of Lodi [Provincia di Lodi, 2011], it was noted that the two maps shared the same pattern. Therefore, the projection of the cadastral WMS (EPSG[11]:3003, Gauss-Boaga zone Italy1) was attributed also to the farm's cadastral map.

Conversion from DXF to SHP data generated two separate shapefiles: one containing polygon vectors with no attributes (here representing the farm's cadastral map); and another containing point vectors and related table of attributes. In the original map in DXF format (generated by the AutoCAD software in use at the Bianchini farm), these points would translate into labels of the map's various features, ranging from parcel's cadastral codes, to sheet numbers, to topological names, etc. However, opposite to any GIS, in AutoCAD the meaningfulness of such labels purely relies on their visual positioning in the map with respect to the underline vectorial features, rather than on a mathematical relational link. Therefore, in order to link the polygon features (the parcels) with their own attributes (parcel's cadastral number and sheet number), an appropriate SQL selection for parcel numbers was operated on the point features. Then, a spatial join between the polygons and the selected point features was attempted for registration of the parcels' numbers. Subsequently, a manual on-the-fly overlay of the polygons features with the cadastral WMS map allowed for removal of the errors in the parcels cadastral numbers and the attribution of the correct cadastral sheet numbers to each parcel.

Once the map had been completed, based on the cadastral parcel's numbers and on the table of conversion provided by the farm managers, parcels' names corresponding to the appropriate cadastral sheet and parcel codes were also registered as an additional field in the map's table of attributes. However, the relationship between cultivated parcels' names and cadastral parcels often appeared to be one-to-many, as the farm managers reshaped cadastral parcels in the past according to their operational needs. Some refining consisting in the merge and/or split of some cadastral parcels had therefore to be performed manually. Eventually, by use of parcels' names, the map could finally be linked to the farm's data related to production and treatments.

In the parcels map's attributes table, two extra columns were created and records were filled in with the type of cultivated crops for each year of reference (2010, 2011). In this way, the parcels map's symbology could be customized to indicate the crops grown on each year for later use in the overlay with satellite images.

Due to Hyperion's pixel size (30 m), in order to preserve purity of border-pixels' reflectance and avoid any influence of green vegetation, roadsides and other unwanted features delimiting the parcels, a new shapefile was generated from the parcels map by creating an inner buffer at 10 m from the border. The "buffered" conservation parcels were those finally used for matching with the Hyperion images.

11 EPSG (European Petroleum Survey Group) is a body, now part of the "International Association of Oil and Gas Producers", that in recent years created and published the Geodetic Parameter Dataset, a structured dataset of Coordinate Reference Systems and Coordinate Transformations referenced by a specific number code. The EPSG coding is now supported by several GIS applications and each code uniquely identifies Datum, Ellipsoid and Coordinate System. EPSG:3003 corresponds to International Spheroid, Transverse Mercator Projection (Monte Mario/Italy 1). [OGP, 2001]

## Remote sensing data processing

The Hyperion imagery is distributed by NASA/USGS in two different levels of finish:

- Level 1Gst: it consists of terrain corrected data, provided in 16-bit radiance values; The Level 1Gst product also includes terrain (ortho-) correction through use of a digital elevation model (DEM) to correct parallax error due to topographic relief and improve the overall band-to-band registration accuracy. The elevation data used for correction consist of the Shuttle Radar Topography Mission (SRTM) "Finished" data set and other elevation data as required.
- Level 1R: it consists of radiometrically corrected-only images (watts/(sr-micron-$m^2$)x100), formatted as HDF files, and metadata in binary and ASCII formats. User georeferenciation and ortho-correction is required.

Because of the higher processing level, use of the L1Gst imagery was attempted at first. However, by overlap with some of the existing online WFS elements of the Carta Tecnica Regionale (CTR10) map [Provincia di Lodi, 2011] of the same area, it soon became clear that the georeferenciation of such Hyperion imagery could not be accepted as satisfactory because of a very clear shift of the scenes of few hundreds of meters in the North-East direction (Figure 5).

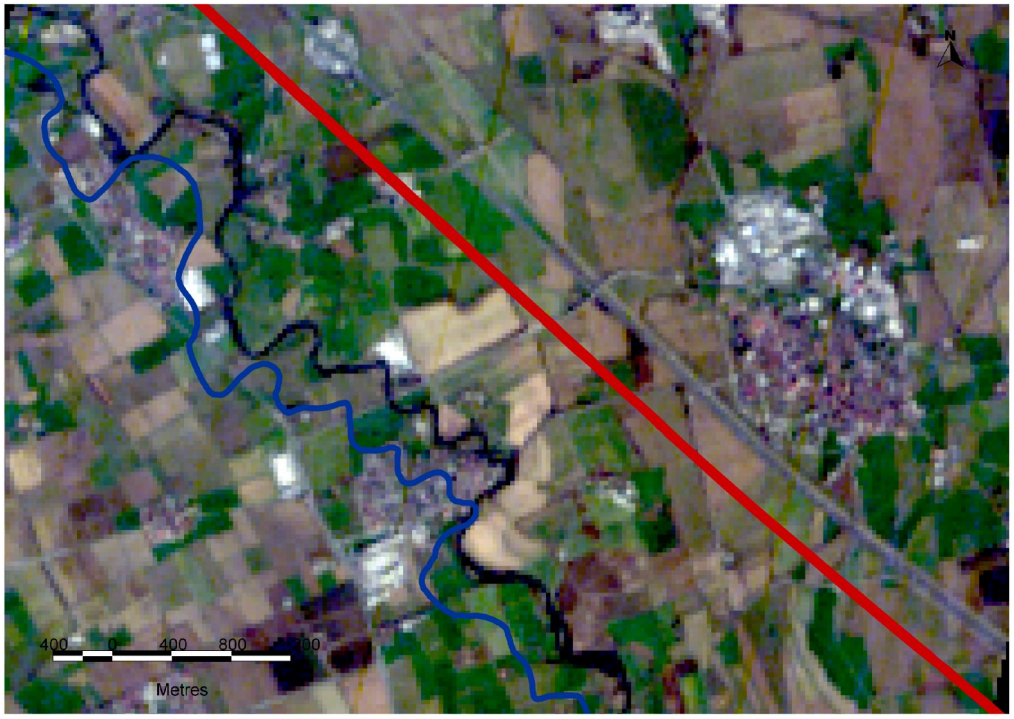


*Figure 5: An example of the bad georeferenciation of a Hyperion 1Gst scene in the area of interest. In the background: true-colour L1Gst Hyperion image (RGB=31:20:10; image no. EO1H1930282011055110PZ acquired on 24/02/2011). In red: A1 highway next to Lodi Vecchio (on the right). Source: autostrada_ct10 WFS [Provincia di Lodi, 2011]. In light blue: Lambro river. Source rete_idografica_ct10 WFS [Provincia di Lodi, 2011]. Note the shift of these very same features in the Hyperion image with respect to ground truth.*

Therefore, a careful image repositioning (georeferenciation) was successfully attempted through an image-to-ortophoto registration in QGIS using the TerraItaly 2007 WMS orthophotos from Provincia di Lodi, 2011. However, a more in depth analysis of the sub-scenes (bands) revealed further problems. In particular, a relevant striping effect was noted on several bands, including some of fundamental

importance for the elaboration of certain indices under the present research.

An investigation on the occurrence of such issue was carried out and confirmation widely found in the available literature. By doing so, an additional problem was also detected, consisting in a misregistration (one-pixel shift) of the right hand-side half of the SWIR sub-scenes with respect to the VNIR sub-scenes (Figure 6).

Therefore, it appeared clear that a destriping pre-processing and a correction of the SWIR misregistration was needed before any further processing could be performed.

Unfortunately, no open source or commercial software is currently available that performs destriping out of the box. Therefore, such an operation needed to be programmed from scratch. A literature analysis was performed on the known theoretical methods to destripe satellite imagery.

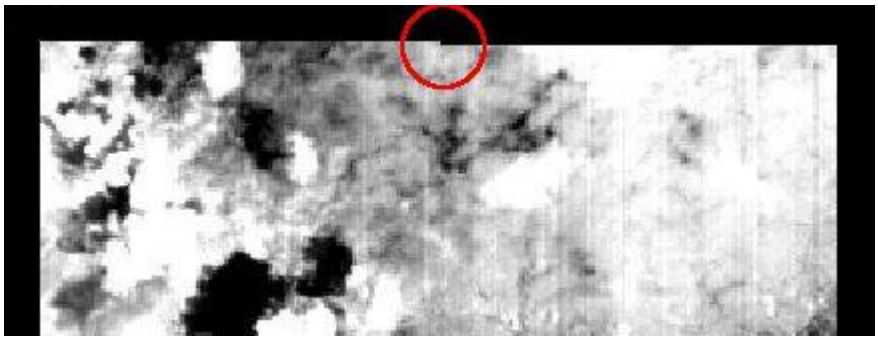

*(a)*

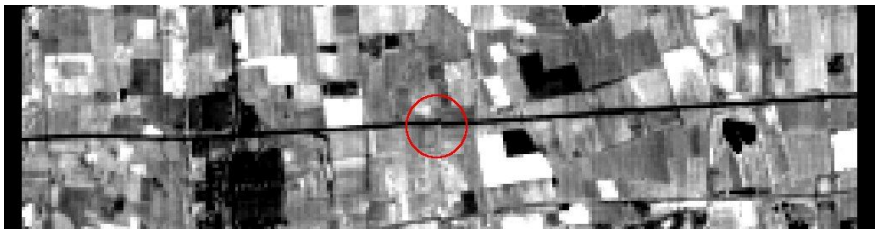

*(b)*

*Figure 6: Two examples (circled) of the step-like effects of the one-pixel misregistration in a Hyperion SWIR bands (image EO1H1930282010203110PC, band 89) on the upper image border (a) and on a road (b). Each pixel has an approximate size of 30 metres.*

Much effort is recently being dedicated by researchers around the world to solve the striping issue as it can severely impair the results of any hyperspectral analysis.

Tsai et al., 2005, proposed the use of a **cubic spline curve-fitting**[12] algorithm to destripe any Hyperion image, based on the idea that each line of an image (band) can be described as a piecewise spline curve. As a first step, pixels affected by the striping noises must be identified, followed by the collection of the noise-free pixels. These are used as samples to construct a cubic Hermite spline[13] curve that passes all of the control points (samples). The original values of the striped pixels can then be approximated from the spline curve. Applying this procedure to an image, line by line or column by column, a striping-free image can be reconstructed accordingly. Yet, the method proposed requires prior knowledge on the position of the stripes, and yields best results on images affected by narrow

12 Cubic spline fitting is a type of interpolation that uses third order piecewise polynomial equations, a category of equations that change their definition depending on the value of the independent variable and where the order, or degree, represents the highest exponent of the independent variable.

13 Hermite is a spline (see above) where each polynomial possesses two control points and two control tangents.

stripes.

**Spatial moment matching (SpaMM)** is a technique proposed by Datt et al., 2003, based on spatial autocorrelation that attempts to balance (match) histogram moments, represented by means and variances of the image pixel columns in each band, to those of a reference histogram. Such histogram varies with the form of balancing chosen. With "global" balancing, the statistical moments of each column are modified to match those for the whole image for each band. With the "local" approach, reference moments are estimated locally based on a selectable number of neighbouring columns. Spatial moment settings should be chosen considering the type of bands to destripe (VNIR or SWIR), the overall environmental conditions and the ground land cover classes (such as forests, crops, water and deserts) being imaged [Datt et al., 2003].

**Spectral moment matching (SpcMM)**, a method introduced by Sun et al., 2008, uses spectral autocorrelation (as opposed to spatial autocorrelation of SpaMM) to estimate the expected mean and standard deviation of a sub-scene (i.e. a band), which is comprised of the pixels acquired by an identical detector element (see the Hyperion paragraph above). This method has been originally implemented as one of the components of a complete software package for hyperspectral image processing maintained at the Canadian Space Centre. The software is not available to the general public. However, the whole method has been thoroughly documented in a scientific paper [Sun et al., 2008].

The method is based on the observation that in a hyperspectral image cube[14] there are usually highly correlated groups of bands; the statistics of the sub-scenes measured by the corresponding detectors in a set of highly correlated bands are usually very similar. However, SpcMM assumes that the sensor radiometric response function is linear and that the stripes are not correlated band to band.

SpcMM removes various types of stripes without introducing undesired side effects into the destriped images due to the proper estimation of the expected mean and standard deviation for each along-track column. Moreover, SpcMM can automatically destripe an entire Hyperion image cube without the manual selection of defective bands or across-track spatial regions, or the individual selection of band-specific window sizes for spatial smoothing like in the case of SpaMM.

Carfantan and Idier, 2010, adopted a self-calibration method to perform linear response correction (no specific training data required), based on a Markov random field[15] model for the logarithm of pixel intensities. This approach, calibrated for pushbroom sensors (such as Hyperion), also assumes a linear response of the detectors and its efficiency depends on the validity of such assumption. For example, if the offset of a detector's affine (i.e. linear) response has not been correctly calibrated, destriping with a moment-matching-based method may give better results than with the proposed method.

For this reason and the for the completeness of the mathematical description of the method, spectral-moment matching was adopted in the present research. An email contact with the first author of the SpcMM method (Lixin Sun) was successfully established in order to clarify few of the processing mechanisms that, despite the detailed description in the article, appeared ambiguous.

A summary of the principles underlying SpcMM is presented hereafter. Given any Hyperion scene (that is, its spectral cube, see Figure 7), the spectral moment matching method performs destriping based on the following steps:

1. Calculate spectral moments (mean and standard deviation) of each along-track column in the cube. Extreme values are likely to be caused by stripes.
2. To minimize the influence of extreme values, calculate median values of the above means and

14 "Hyperspectral cube" is the parallelepiped formed by the stack of the images (bands) of a single scene, where each layer of the stack is an image (or sub-scene). The "cube" has the following dimensions: number of bands times the number of along-track columns times the number of across-track rows of each of the sub-scenes. For Hyperion, dimensions are 242, 256, ~3000 (the latter may vary with the scene's length).

15 "Markov random field" (or MRF) is a branch of the probability theory with several applications, including image analysis. For a detailed explanation, please visit: www.cmap.polytechnique.fr/~rama/ehess/mrfbook.pdf

standard deviations in the across-track dimension based on moving windows of user specified size. Median is attributed to the central pixel in the window. For border pixels, the window is reduced.

3. For a target detector (of the band to be destriped, or target band), calculate mean and standard deviation of the medians in an across-track (target) window of user specified size centered on the detector. Then do the same in the corresponding (test) windows in all the other bands. For each of these bands, determine a rescaling factor by dividing target and test means. Do the same for the standard deviations. Repeat for all target dectors in the same band. Then rescale all the original medians of means and of standard deviations in the test bands to those of the target band by multiplying for the rescaling factor. Border pixels behave similarly to the previous point (windows reduced).

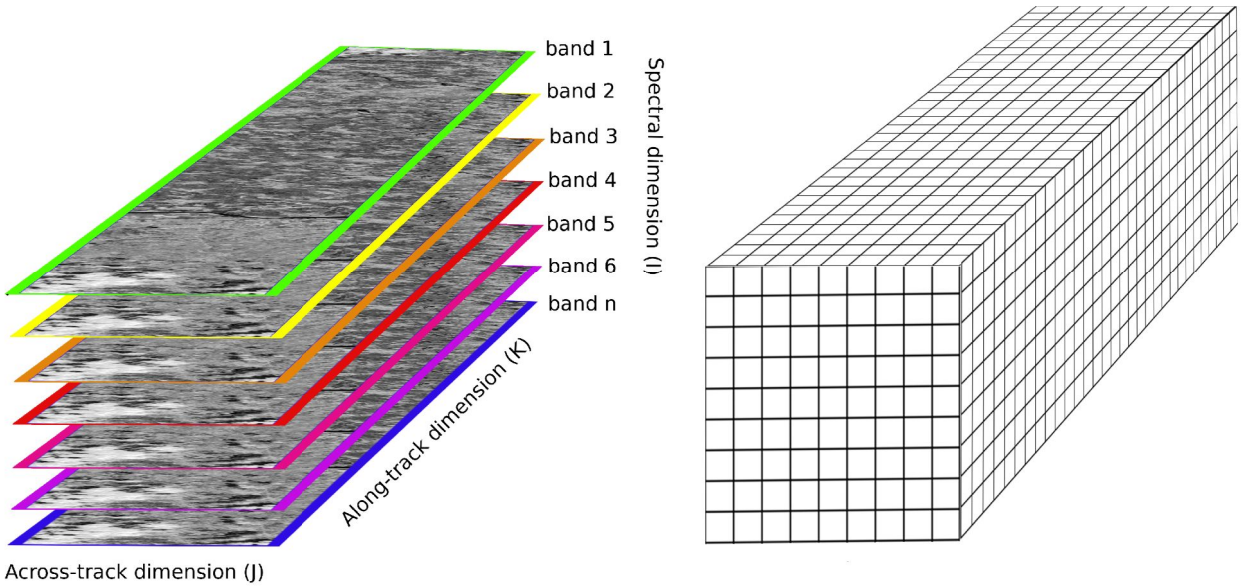


*Figure 7: Illustration of a hyperspectral cube. Stack of bands (left) and its equivalent in terms of image pixels (right). Notation of dimensions (I,K,J) has been preserved from the original article [Sun et al., 2008] to the script.*

4. For each of the detectors in the band to be destriped, identify a group of highly correlated bands (number determined by user choice) based on Euclidean distances between the rescaled means in the across-track windows of point 3 and the mean of the target window. Repeat for standard deviations.
5. Collect the original means and standard deviations of the along-track columns in the highly correlated bands.
6. Calculate the average values per column. These will represent the expected mean and standard deviation in the destriped band.
7. Calculate gain and offset based on the original and the expected means and standard deviations.
8. Destripe an entire column in the target band based on the calculated gain and offset.

Because destriping with SpcMM is performed by rows and columns, it is necessary that across-track and along-track dimensions are oriented parallel to the X and Y axes of a common Cartesian system, respectively. That is the case of the Hyperion L1R images, that were therefore used for this study.

When the programming phase was met, the question arose on which language could be used. Indeed, a

number of programming languages are available for managing image processing. The following are the languages investigated based on some personal experience in their use:

- Interactive Data Language (IDL). IDL is a proprietary software of ITT Visual Information Solutions. There exists an open source clone of IDL called GNU Data Language (GDL) and it is almost completely compatible with the IDL scripting.
- Matlab. A proprietary software of The MathWorks, Inc. A free clone is available under the name GNU OCTAVE. Like in the previous case, compatibility with Matlab is almost 100%.

Other software is available (namely, Python, Perl Data Language) that could have probably helped in addressing the objective, but it would have implied the undertaking of a long and uncertain learning process and was therefore excluded.

GDL proved very useful throughout the processing sequence. However, on the very last step consisting in the conversion of the process-resulting matrix into a proper image, GDL did not offer any usable command. Indeed, many IDL subroutines are still waiting to be implemented in GDL, including the writing of matrices to image readable files, like GeoTiff, that support 16bits signed type of data (as the original Hyperion images). The conversion of the processed matrix into image could not be solved and this in turn forced the abandonment of this language.

The choice was finally made for GNU OCTAVE, that presents a vast array of functions and is extensible with additional packages. GNU OCTAVE proved to offer all the needed commands and flexibility for the processing of the original images and their transformation. GNU OCTAVE runs on Linux, MAC OS and Windows platforms. However, the latest updates are always released for Linux first. Therefore, GNU OCTAVE was compiled and run in a Linux environment. The whole script programmed for a complete destriping of Hyperion images is reported in text format in Annex III. Additional steps were introduced with respect to the original SpcMM procedure to correct for the one pixel misregistration in the SWIR sub-scenes.

After debugging, the script's first results did not appear to fulfil the SpcMM authors' promise to eliminate the striping issue. Indeed, the script's output images were affected by even more artefacts than the original images. A deeper investigation into the problem was therefore initiated. By looking at the spectral profiles of both the original and the processed cube (Figure 8), it was noted that the latter suffered an increase – rather than a decrease – in the number and intensity of peaks and sinks with respect to the original cube's profile.

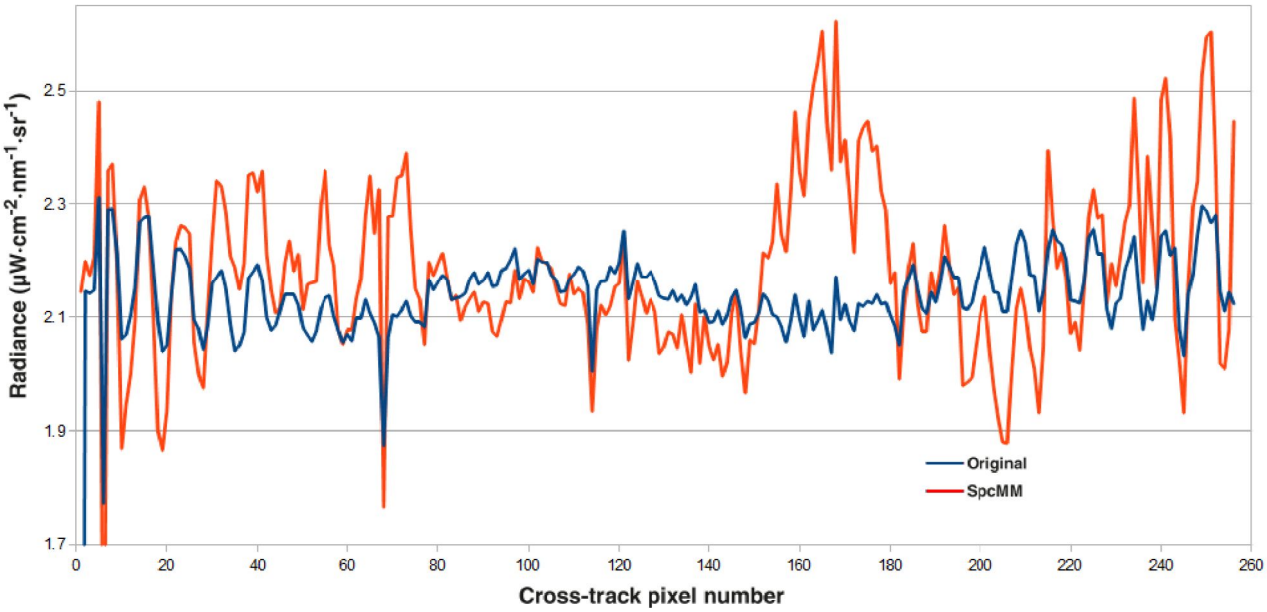


*Figure 8: Mean values of all the along-track columns of Hyperion scene EO1H1930282010265110Pz (band 8, whole image). The original image radiance is in blue and the processed radiance using the original SpcMM in red. The increase of vertical fluctuations from the blue to the red profile reflects the unwanted increase in the number and width of stripes in the processed image.*

This clearly indicated that the script was malfunctioning in the calculation of the profile correction parameters across the board. However, the script reflected exactly the indications of the paper. Further investigations revealed that a bad mathematical notation in the article related to the calculation of the image offset, and therefore of the values of the destriped pixels, could have explained this behaviour. By comparison with the way the offset was calculated in the SpaMM method [Datt et al., 2003], an attempt was made to change the offset notation from minus to plus and the script was re-run. Finally, the resulting images appeared to be consistent with the SpcMM theoretical model and showed mostly stripe-free images in all the bands.

In order to get confirmation of the findings, a further notice with a request of clarification was sent to Mr Sun (first author of the paper), but unfortunately it remained unanswered for.

An example of the remarkable results obtained with the corrected destriping code is displayed inFigure 9. The spectral profile of the destriped image versus the original image also confirmed the goodness of the processing Figure 10.

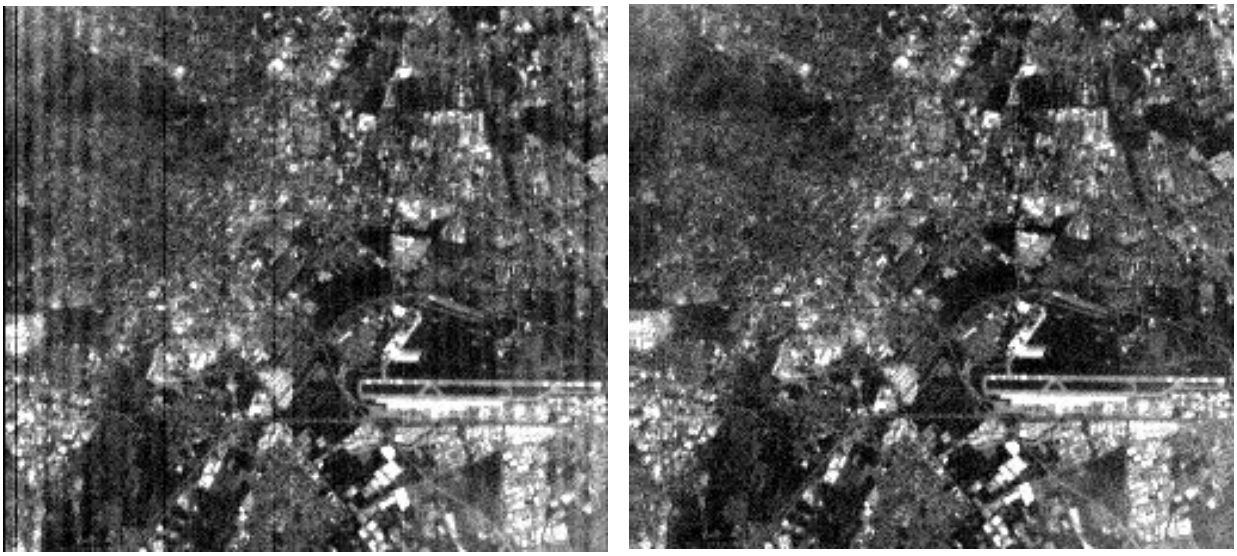

*Figure 9: Example of the effects of the destriping processing. Left: original L1R Hyperion image EO1H1930282010265110Pz (band 8, cropped) depicting the area around the Orio al Serio Airport (visible).*
*Right: the same image/band after destriping with the GNU Octave code based on the corrected spectral moment matching technique.*

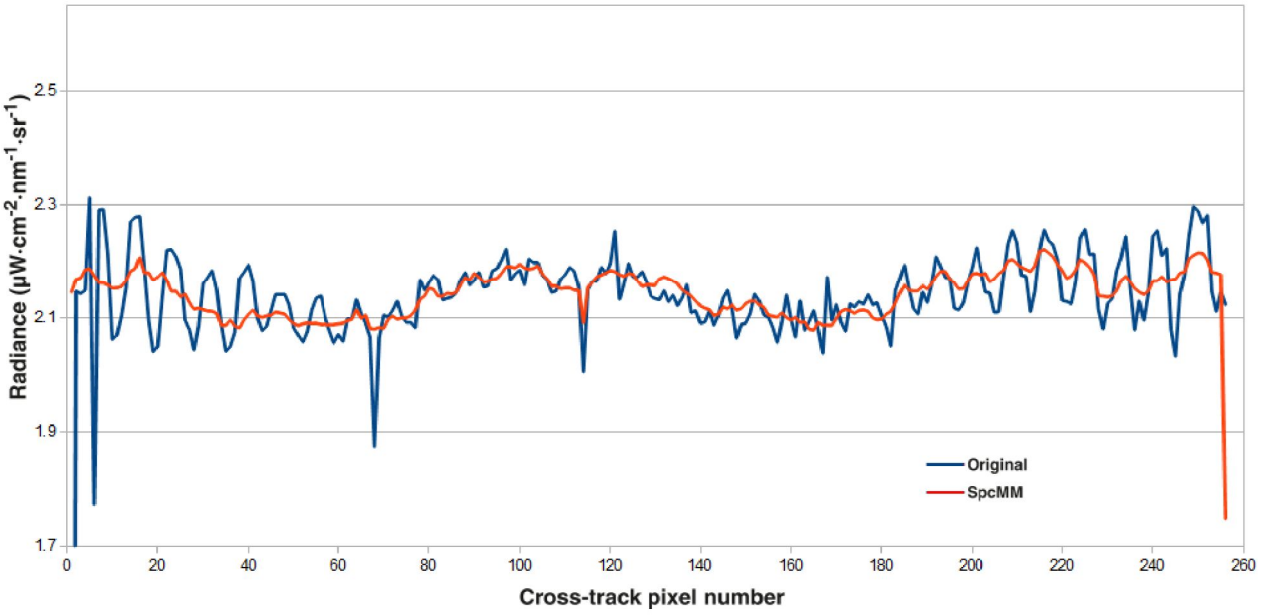


*Figure 10: Mean profiles of all the along-track columns of the images inFigure 9 (uncropped).*
*Original radiance (in blue) is exactly the same as in Figure 8. Instead, the destriped radiance obtained using the corrected SpcMM (in red) now follows well the vertical variations but with much smoothed peaks and sinks.*

After destriping was performed, the imagery had to be corrected for the atmospheric and scattering effects.

Only very few open source software perform atmospheric correction. "OPTICKS" (opticks.org) is one of them. It is an expandable remote sensing and imagery analysis open source software platform that

offers two packages for atmospheric correction: the IARR and the EL. However, OPTICKS lacks any user documentation on how to use them and information from other sources is equally insufficient. This prevented the use of OPTICKS perform atmospheric correction.

GRASS GIS [GRASS, 2011.] also offers atmospheric correction by implementing one of the available versions of the 6S code. However, the 6S correction module accepts only a number of sensors' images in input that do not include Hyperion.

Given these limitations, commercial software had to be considered. According to Kawishwar, 2007, FLAASH provides user with more options than ATCOR to control sun-sensor geometry, accommodate for adjacency effect and CO2 concentration levels. FLAASH was demonstrated to be effective in the atmospheric correction of Hyperion and Ali images [Yuan and Niu, 2008; Yuan et al., 2009]. FLAASH is also embedded in the widespread ENVI software and supports input of Hyperion data (as well as other hyperspectral sensors). It was therefore picked for use in the present research.

For atmospheric correction, FLAASH requires the preliminary input of a number of parameters such as center location of the input image, date and time of flight (pass), sensor altitude, ground elevation, pixel's size. Most of these were derived from the image's metadata. Subsequently, other input parameters are required to allow for the calculation of the water vapour column. These include the specification of the type of atmospheric model as required by MODTRAN (Sub-artic winter, Mid-latitude winter, U.S. Standard, Sub-artic summer, Mid-latitude summer, Tropical) and of the aerosol model (no aerosol, rural, maritime, urban, tropospheric)

Option is given to the user for spectral polishing, water retrieval, aerosol retrieval and wavelength recalibration. In the advanced hyperspectral settings, the user has to further specify the view zenith and azimuth angles.

For a more in depth description of the actual mathematics behind the FLAASH tool, the reader is referred to the ENVI documentation (Atmospheric Correction Module: QUAC and FLAASH User's Guide, freely available online at: www.ittvis.com/portals/0/pdfs/envi/Flaash_Module.pdf).

The United Stated Geological Survey (USGS), distributor of the Hyperion images, also offers a detailed tutorial[16] on how to perform the atmospheric correction of Hyperion images. Unfortunately, this document does not indicate how to calculate the view azimuth angle as this figure is not given in the Hyperion metadata files. In ENVI, the view azimuth is defined as the angle between the line of sight and due North of the sensor as viewed from the ground. An inquiry sent to the USGS help-desk did not clarify this issue. Further contacts were established with Marcos Montes, researcher at the US Naval Research Laboratory and first author of an article on hyperspectral remote sensing [Montes et al., 2004] where such angles were specified. Montes very kindly replied, suggesting that the azimuth angle should be derived from the bearing (heading) of the two long sides of an image. The latter can be calculated from the image's corners. Headings must then be averaged and subtracted of 90 degrees to obtain the view azimuth.

All the parameters used for atmospheric correction of each Hyperion scene in the present research can be found in the following Table 4.

16 The tutorial (EO-1 User Guide v. 2.3) is available from: http://edcsns17.cr.usgs.gov/eo1/documents/EO1userguidev2pt320030715UC.pdf

| Scene filename | Place | Date | CC | Time | Atm. Model | Center lat/long | Zenith | Azimuth |
|---|---|---|---|---|---|---|---|---|
| EO1H1930282010221110Kj | LV | 09/08/10 | 10 | 09:48:51 | Mid-lat summer | 9.42, 45.39 | 169.3200 | 103.1596 |
| EO1H1930282010260110KF | LV | 17/09/10 | 90 | | | | | |
| EO1H1930282010314110Pp | LV | 10/11/10 | 90 | | | | | |
| EO1H1930282011055110PZ | LV | 24/02/11 | 0 | 09:51:36 | Mid-lat winter | 9.42, 45.39 | 173.7474 | 103.6755 |
| EO1H1930282011252110KZ | LV | 09/09/11 | 0 | 10:00:22 | Mid-lat summer | 9.42, 45.39 | 173.1981 | 105.1087 |
| EO1H1930282010203110PC | SM | 22/07/10 | 10 | 09:51:27 | Mid-lat summer | 9.53, 45.25 | 174.3211 | 103.7350 |
| EO1H1930282010265110Pz | SM | 22/09/10 | 0 | 13:06:08 | Mid-lat summer | 9.53, 45.25 | 177.0277 | 104.0095 |
| EO1H1930282010278110KE | SM | 05/10/10 | 70 | | | | | |
| EO1H1930282011006110Kp | SM | 06/01/11 | 90 | | | | | |
| EO1H1930282011024110Pc | SM | 24/01/11 | 0 | 09:52:32 | Mid-lat winter | 9.53, 45.25 | 176.1846 | 103.9336 |
| EO1H1930282011037110PZ | SM | 06/02/11 | 20 | | | | | |
| EO1H1930282011050110Kg | SM | 19/02/11 | 0 | 09:58:04 | Mid-lat winter | 9.53, 45.25 | 174.9462 | 104.9290 |
| EO1H1930282011081110Kb | SM | 22/03/11 | 0 | 09:56:46 | Mid-lat winter | 9.53, 45.25 | 176.8453 | 103.9543 |
| EO1H1930282011151110KZ | SM | 31/05/11 | 60 | | | | | |
| EO1H1930282011270110PZ | SM | 27/09/11 | 10 | 09:54:37 | Mid-lat summer | 9.53, 45.25 | 179.1111 | 104.2253 |

*Table 4: Parameters used for the atmospheric correction of all the Hyperion scenes with FLAASH. Places: LV=LodiVecchio, SM=San Martino in Strada. CC=cloud cover (in percent). Lat/Long coordinates as well as (View) Zenith and Azimuth angles are in decimal degrees. Images with cloud cover over the area of interest were not processed and show empty fields.*

As per the above tutorial, the advanced hyperspectral settings in FLAASH were not changed from default.

An example of the correction obtained by applying the FLAASH tool can be seen in Figure 11 where the radiance/reflectance profiles of the original image and of the resulting image are displayed.

Another source of potential distortion in Hyperion images is caused by a spatial misalignment of the the detector elements that reflects into a shift in wavelength in the spectral domain known as smile/frown effect. Distortion occurs as a function of across-track pixel (column) in the swath[17] and can also be a result of aberrations in the collimator and imaging optics. Shifts of less than 1 nm have been observed in the SWIR wavelengths and 2.6 – 4.25 nm shifts in the VNIR wavelengths [Dadon et al., 2010; Aktaruzzaman, 2008]. Despite few techniques have been devised for the correction of the smile effect (Trend Line Smile Correction [Dadon et al., 2010], Cross Track Illumination correction ITT VIS, 2011a, Linear Fitting and Interpolation [Aktaruzzaman, 2008; Goodenough et al., 2003]), the correction of the smile effect remains a considerable challenge for the scientific community [Dadon et al., 2010]. In relation to this, to the fact that SWIR bands are used and to the reduced size of the study area, the smile effect correction was not attempted as an independent process. However, the above FLAASH module in ENVI does minimize the smile effect when recalibrating the wavelengths during the atmospheric correction processing [Kawishwar, 2007; ITT VIS, 2011b].

As a last step, Hyperion images were also processed to reduce the amount of residual noise.

A Minimum-Noise-Fraction correction (forward and backward) was applied by use of a specific ENVI tool.

17 Swath is the area imaged by the sensor on the surface.

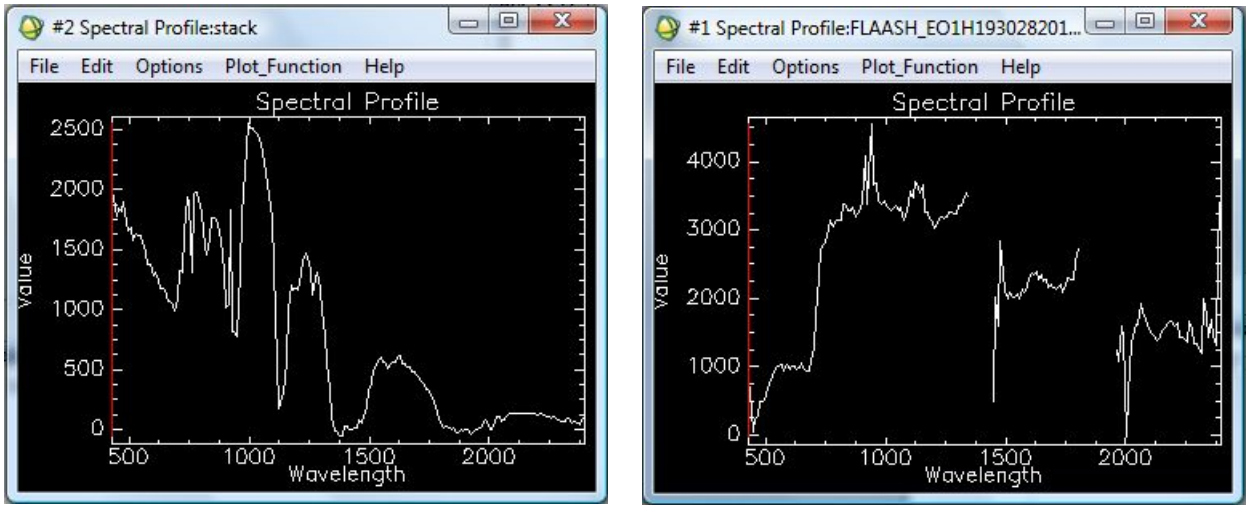


*Figure 11: Spectral profiles of an Hyperion image before and after atmospheric correction. Left: radiance of the original Hyperion image EO1H1930282010265110Pz (band 8, pixel 129(X), 200(Y)). Right: reflectance (right) of the same image after atmospheric correction with FLAASH. Gaps in the latter profile indicate bad bands.*

The Minimum Noise Fraction (MNF) transform is used to segregate noise in the data, to determine the inherent dimensionality of image data and to reduce the computational requirements for subsequent processing [ITT VIS, 2009]. The MNF transform in ENVI operates two sequential Principal Components[18] transformations. "The first transformation, based on an estimated noise covariance matrix, decorrelates and rescales the noise in the data. This first step results in transformed data in which the noise has unit variance and no band-to-band correlations. The second step is a standard Principal Components transformation of the noise-whitened data. For the purposes of further spectral processing, the inherent dimensionality of the data is determined by examination of the final eigenvalues and the associated images. The data space can be divided into two parts: one part associated with large eigenvalues and coherent eigen-images, and a complementary part with near-unity eigenvalues and noise-dominated images. By using only the coherent portions, the noise is separated from the data, thus improving spectral processing results." [ITT VIS, 2009]

In the present research, forward MNF was first applied with noise statistics estimated from the image. A spectral subset was operated to further select and exclude Hyperion sub-scenes that resulted black after atmospheric correction (bands 93-101 and 138-152 were discarded). A total of 174 bands remained for MNF processing. By visual inspection of the 174 eigen-images calculated by MNF during the forward processing, only the first 13 were retained for the subsequent inverse processing, accounting for about 60% of the variability. Inverse MNF was then run, during which the whole set of 174 'noise-free' bands was regenerated.

As a last step in the pre-processing of Hyperion imagery, georeferenciation was performed. Although ortho-correction would have been preferable, RPCs were not available and the images were acquired over largely flat terrain areas. For this reason, georeferentiation was performed and GCPs acquired through an image-to-ortophoto registration in QGIS [QGIS, 2011] using the TerraItaly 2007 WMS orthophotos from Provincia di Lodi, 2011. GCPs were then applied to the original images and warping operation performed by using specific GDAL (Geospatial Data Abstraction Library) commands [Warmerdam, 2011] to every single band in batch mode (polynomial order 1 (affine) and cubic convolution resampling). However, due to the different length of the acquired scenes, georeferenciation

18 Principal Components Analysis is a mathematical procedure that linearly transforms a set of observations of possibly correlated variables into a set of values of uncorrelated variables, called principal components, that contain most of the information of the original variables. [Dunteman, 1989]

had to be performed separately and from scratch on each scene. ENVI, GDAL and QGIS were run in a Windows Vista environment.

## Crop residue indices

Several techniques for mapping and estimating crop residues on the ground can be found in literature, such as visual estimation, line transect, point intercept, meter stick, spiked wheel and photographic techniques. However, all of these methods assume that data are collected by surveyors by means of field sampling, implying relevant financial and time investments and severe limitations in the extent of the area covered [Bannari et al., 2006; Bannari et al., 2007a]. Vice versa, provided that expert knowledge and careful processing is applied, remote sensing can effectively alleviate some of these problems by imaging vast surfaces at ones.

Since the late eighties, several indices have been developed for the estimate of crop residues. The first indices were mostly based on Landsat TM bands. Landsat offered several advantages in terms of the large areas covered, the temporal resolution and the low cost. However, discrimination of crop residues from soils in Landsat imagery proved challenging due to the similarity of their spectral responses in the visible (VIS) and Near Infra Red (NIR) wavelengths, especially under moist conditions [Streck et al., 2002], and due to the broad TM bands that convolve the spectral responses of different materials across the bandwidth [Serbin et al., 2009b].

With the discovery of crop residues distinct absorption features in the Short Wave Infra Red (SWIR) wavelengths and with the arrival on the market of hyperspectral imaging, precision in the characterisation, discrimination and estimate of crop residues improved greatly due to the extended range of wavelengths detected by the new sensors in the SWIR domain [Arsenault and Bonn, 2005]

In parallel with the evolution of remote sensing techniques and the increased availability of imagery at higher spectral and spatial resolution, new, more effective indices were and are continuously being developed.

A brief overview on the indices most commonly found in literature is presented hereafter with the aim to illustrate the reasons that brought to consider only a number of indices for the present study. Serbin et al., 2009b, grouped indices into three different categories based on their underlying principles: (i) normalized difference indices, (ii) spectral angle methods, and (iii) reflectance-band height indices. A fourth category could actually be proposed to account for the indices based on spectral unmixing, as illustrated below.

The Brightness Index (BI) [Major et al., 1990[19]] was devised as the sum of the reflectances of the first four bands of Landsat TM sensors. However, it was reported that BI is dependent on the optical properties of bare soil [Bannari et al., 1999[19]] and that its overall accuracy can be as low as 20% [Bannari et al., 2007a].

The Normalized Difference Index (NDI) [McNairn and Protz, 1993[19]; Arsenault and Bonn, 2005] is based on the same concept as the Normalized Difference Vegetation Index (NDVI) but uses the near infrared (TM4) and short wave infrared (TM5) bands instead of the red and near infrared bands. It is calculated using any of the following equations: $NDI = \frac{\rho TM4 - \rho TM5}{\rho TM4 + \rho TM5}$ or $NDI_1 = \frac{\rho TM4 - \rho TM7}{\rho TM4 + \rho TM7}$ where ρ indicates reflectance in the specified TM band or equivalent bands of other sensors. Bannari et al., 2007a, proposed an $NDI_2$ were bands were shifted upward with respect to $NDI_1$ to accommodate them for a better performance of the Probe-1 sensor.

19 In Bannari et al., 2007a.

Equally inspired by the NDVI concept are the following three indices:
The Normalized Difference Tillage Index (NDTI) [van Deventer et al., 1997[20]], is expressed as $\mathrm{NDTI}=\frac{\rho TM5-\rho TM7}{\rho TM5+\rho TM7}$ whereas the Normalized Difference Senescent Vegetation Index (NDSVI) [Qi et al., 2002[20]], is calculated as $\mathrm{NDSVI}=\frac{\rho TM5-\rho TM3}{\rho TM5+\rho TM3}$ . Both make use of the Landsat TM bands. The Shortwave Infrared Normalized Difference Residue Index (SINDRI) was proposed by Serbin at al., 2009a, and it is based on the formula: $\mathrm{SINDRI}=\frac{\rho A6-\rho A7}{\rho A6+\rho A7}$ where A indicates ASTER bands. An hyperspectral equivalent (named hyperspectral SINDRI) is also in use: $\mathrm{hSINDRI}=\frac{R_{2210}-R_{2260}}{R_{2210}+R_{2260}}$ were R are the reflectances in the indicated wavelengths.

The Soil Adjusted Corn Residue Index (SACRI) [Biard et al., 1995[21]; Arsenault and Bonn, 2005] is similar to NDI, but is less sensitive to the optical properties of bare soil as it takes the soil/line concept into account. SACRI is also reported to work better with small amounts of crop residue cover [Arsenault and Bonn, 2001[21]] and it is calculated as: $\mathrm{SACRI}=\frac{\alpha(\rho TM4-\alpha\rho-\alpha\rho TM5-\beta)}{\alpha\rho TM4+\rho TM5-\alpha\beta}$ where α is the slope and β is the intercept of the soil line[22] (TM4/TM5).

The Modified Soil Adjusted Corn Residue Index (MSACRI) [Bannari et al., 2000[21]] was derived from SACRI by substituting ETM5 and ETM7 to TM4 and TM5 respectively and by recalculating the soil line slope and intercept with the same ETM bands. MSACRI is reported to give good results and to be independent of the optical properties of bare soil.

The Cellulose Absorption Index (CAI) [Daughtry et al., 1996[23]] is based on the simple observation that some of the components of crop residues such as cellulose, hemicellulose and lignin present an absorption feature in the short infrared region (2.1 μm) which allows to differentiate residues from soils.
CAI is calculated as $\mathrm{CAI}=0.5(R_{2.0}+R_{2.2})-R_{2.1}$ where $R_{2.0}, R_{2.1}, R_{2.2}$ are reflectance factors in bands at 2.00–2.05, 2.08–2.13, and 2.19–2.24 μm, respectively [Nagler et al., 2003].

The Lignin-Cellulose Absorption Index (LCA) [Daughtry et al., 2005[24]] was originally devised for use of the Advanced Spaceborne Thermal Emission and Reflection Radiometer (ASTER) data and it is expressed as: LCA = 100[2(A6)-(A5+A8)] , where A indicates the relative ASTER band, A5 is in the range 1.60 – 1.70 μm, A6 is in the range 2.145 – 2.185 μm and A8 is the range 2.235 – 2.285 μm.

The Crop Residue Index Multiband (CRIM) [Biard and Baret, 1997[25]] implements a linear unmixing model to extract the crop residue fraction from the soil-residue complex. CRIM may be applied to any set of spectral bands [Arsenault and Bonn, 2005] and it is calculated as follows:

20 In Serbin et al., 2009b.
21 In Bannari et al., 2007a.
22 The "soil line" is a linear relationship between bare soil reflectance observed in two different wavelengths [Baret et al., 1993]. A similar linear relationship exists for crop residues [Arsenault and Bonn, 2005].
23 In Nagler et al., 2003.
24 In Serbin et al., 2009b.
25 In Arsenault and Bonn, 2005.

$CRIM = \frac{\cos(\zeta)}{\cos(\delta)} * \sqrt{\frac{1-\cos^2(\delta)}{1-\cos^2(\zeta)}}$ where ζ is the angle between the soil line and residues line and δ is the angle between the line formed by uniting two points (a crop residue cover fraction on the soil-residue complex and the intercept point between soil and residue lines) and the soil line. Arsenault and Bonn, 2005, offer a graphical interpretation of the above.

The Spectral Mixture Analysis (SMA) method is based on the observation that each pixel in a digital image is formed by a mixture of reflectances of the underlying pure materials, such as vegetation, soil, water, etc. called endmembers [Arsenault and Bonn, 2005]. Pixels of medium spatial resolution such as Hyperion or Landsat (30 m) are likely to contain a multitude of endmembers. Adams et al., 1989[26], described the mixture in terms of linear combinations of various endmember fractions, as expressed by the equation:

$R_i = \sum_{j=1}^{n} F_j * \mathrm{RE}_{ij} + E_i$ where $R_i$ is the relative reflectance of a pixel in band i; $F_j$ is the fraction of the endmember j, with a constraint that $\sum_{j=1}^{n} F_j = 1$ ; $\mathrm{RE}_{ij}$ is the relative reflectance of the endmember j in band i; $E_i$ is the residual error in band i of j spectral endmembers; and n is the total number of endmembers.

SMA offers a methodology to quantify the fraction of each endmember in the overall scene provided the pure endmembers are identified and their reflectances are collected from the ground, from the image itself or from reference libraries. However, these operations are not always easy to perform due to the complexity of mixtures (number of endmembers) or the unavailability of pure reflectances that may preclude an optimal estimate of the fractions [Song, 2005].

Bannari et al., 2007a, carried out a study on the comparison of several of the above indices (BI, CAI, NDI, SACRI, MSACRI and CRIM) for estimating crop residue cover in order to identify the best performing. Ground-based reflectance measurements and hyperspectral Probe-1[27] data were used as separate remote sensing data sources, whereas ground truth residue values were obtained from estimates based on vertical photographs. The assessment of the indices' accuracy was performed under various crop residues. BI was generally found a poor predictor of residue cover, whereas CAI, contrary to other studies [Nagler et al., 2003], was considered poorly performing on bare soil and sparse corn residue cover under 50%. NDI (in its two forms) and SACRI were found to show a poor correlation with residue cover covers. Both NDI and BI were also found affected by the optical properties of bare soil. The research concluded that the best indices for crop residue cover estimation with ground-based reflectance data are the CRIM and MSACRI-1. For hyperspectral Probe-1 data, the latter was also reckoned relatively representative of the ground reference information and outperformed the other indices.

Arsenault and Bonn, 2005, compared NDI, SACRI, CRIM and SMA on two case study areas. NDI and SACRI calculated with both hyperspectral and TM reflectances were confirmed as not conclusive on the determination of residue cover. CRIM was also confirmed as best performing index ahead of SMA, whose accuracy seems to be affected by the spectral resolution of the input reflectance data.

Similarly, Streck et al., 2002, reported that BI and SACRI under performed in the determination of crop residues but so did the Landsat based indices NDI, NDTI, NDSVI according to Serbin et al.,

26 In Arsenault and Bonn, 2005.

27 An airborne hyperspectral sensor operated by Earth Search Sciences, Inc.

2009b. On the other hand, CAI and to a lesser extent LCA, were found effective by use of hyperspectral data [Serbin et al., 2009b]. SINDRI performed better than LCA but worse than CAI when ASTER data were used. In addition to that, it was found to be sensitive to green vegetation and, to some extent, also to soil and crop residue water content [Serbin et al., 2009b].

Given the above considerations, the scopes and limited resources of the present research, all the Landsat based indices were not further considered. SMA could not be used because of the lack of pure endmember spectra and CRIM was equally dropped because of the uncertainties in the bands to be used [Serbin et al., 2009b]. The failure of all the SWIR ASTER bands in April 2008 further limited the choice. Therefore, final decision was taken to use CAI for this study.

According to Monty et al., 2008, when using CAI with Hyperion data, the following SWIR bands should be selected, averaged into three sets: for $R_{2.0}$, bands centered at 1982, 1992, and 2003 nm; for $R_{2.1}$, bands centered at 2093, 2103, and 2113 nm; while for $R_{2.2}$, bands centered at 2194, 2204, and 2214 nm.

Other researchers who similarly employed CAI with hyperspectral data, indicate a slightly different combination of bands. Guerschman et al., 2009, in a study on the estimate of fractional covers of photosynthetic, non-photosynthethic and bare soil in Australia, used Hyperion bands centered at 2022, 2032 for $R_{2.0}$, bands centered at 2093, 2103, 2113 for $R_{2.1}$, and bands centered at 2184, 2194, 2204 for $R_{2.2}$. Streck et al., 2002, used 1 nm-wide bands (from a portable field spectrometer) centered at 2000, 2100 and 2200 nm for $R_{2.0}, R_{2.1}, R_{2.2}$ respectively, whereas Serbin at al., 2009a, used three 11 nm-wide bands (from an airborne hyperspectral sensor) centered at 2031, 2101 and 2211 nm. Hyperion has bands centered at 2032.35 nm (10.9013 nm FWHM), 2102.94 nm (10.8039 nm FWHM) and 2213.93 nm (10.5328 FWHM nm) respectively that could be used for the scope.

The selection of bands seems to depend on the type of detector used and possibly on the type of residues (land cover) observed. For the present study, band at 2003 nm in the Monty version of CAI initially could not be used even after destriping because of a very high level of noise (Figure 12, left), confirming the findings of Monty et al., 2008. However, after the application of MNF transform, noise was removed (Figure 12, right) and the band was brought back into the index calculation.

CAI values were calculated with the Monty et al., 2008, the Guerschman et al., 2009, and the Serbin et al., 2009b, methods as the Streck et al., 2002, method does not appear to be calibrated to space or airborne hyperspectral sensors.

CAI values were all calculated on the entire cloud-free images collected. Then, pixel values in the Bianchini farm were averaged based on their overlay with buffered conservation parcels.

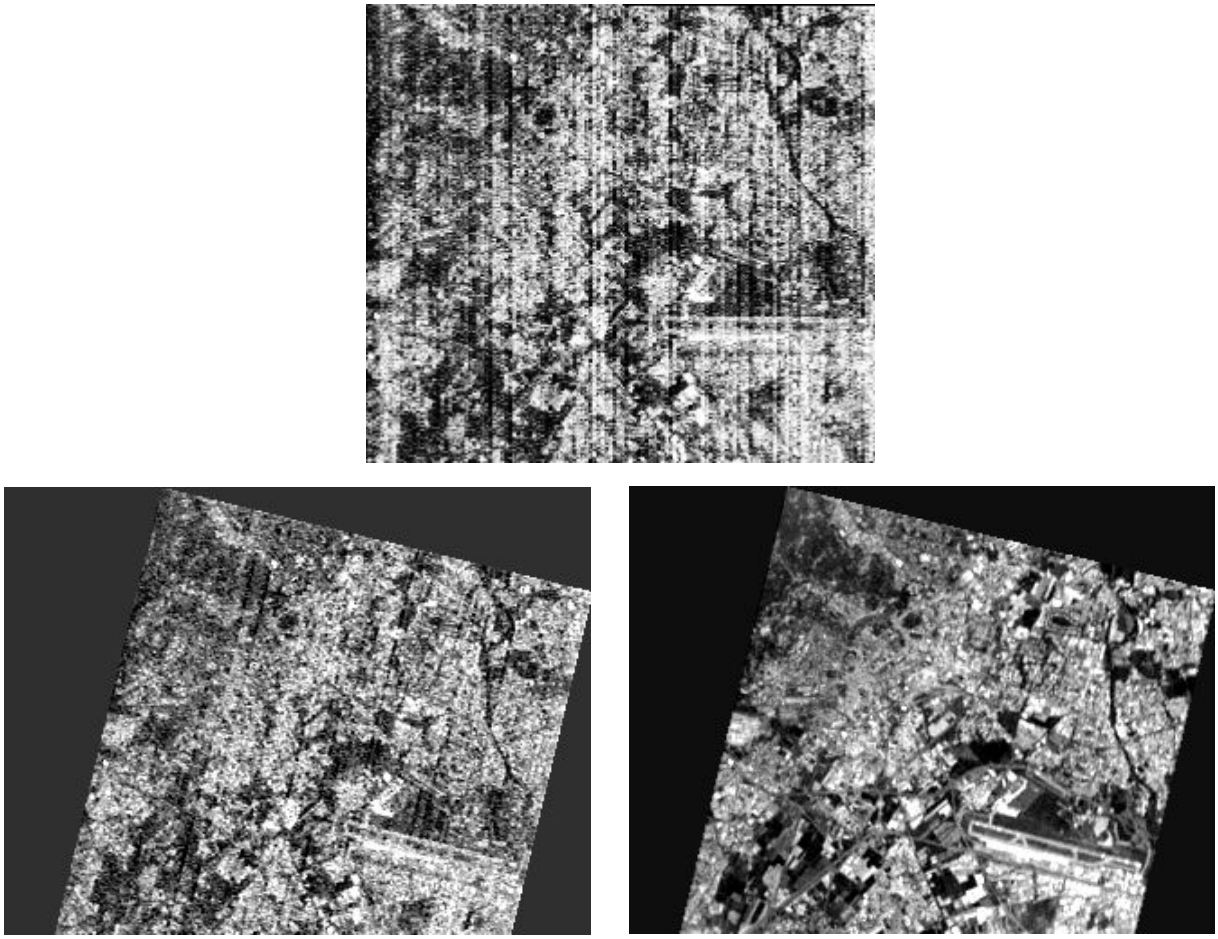

*Figure 12: Improvement of Hyperion image quality across the pre-processing.*
*Up: original Hyperion L1R image EO1H1930282010265110Pz band 185 (cropped). Lower left: the same image (now band 159) georeferenced, atmospherically corrected and partly destriped. Residual stripes are the result of either a lack of sensor linear radiometric response or band to band correlation and could not be removed by SpcMM. Bottom right: the same image (now band 135) after MNF transform.*

# Field sampling

For the determination of the actual amount of crop residues in the study area, field samplings were carried out on three different dates, in an attempt to match as much as possible the timing with the acquisition of Hyperion images and with harvesting periods.

The samplings were carried out applying the line-transect method as described in the United States Department of Agriculture (USDA) National Agronomy Manual[28]. The method was chosen in consideration for its simplicity and proven effectiveness in estimating the percent of the ground surface covered by plant residue at any time during the year [USDA, 2002].

The USDA method establishes that surveys are to be carried out by visual observation of the residues in representative areas of a field and at fixed intervals, located with the help of a meter. For ease of reading, the entire USDA method is reported in the paragraph below.

**Estimating crop residue cover in the field**
**USDA Line-Transect method**

*Estimates of percent cover are used for determining the impact of residue on sheet and rill erosion. They cannot be used directly for determining the impact of residue on wind erosion. Estimates of percent cover obtained using the line transect method to evaluate the impact of residue on sheet and rill erosion are most accurate when the residue is lying flat on the soil surface and is evenly distributed across the field.*

*The following is the recommended procedure for using the line transect method:*

1. *Use a commercially available 50- or 100-foot[29] long cable, tape measure, or any other line that has 100 equally spaced beads, knots, or other gradations (marks) at which to sight.*
2. *Select an area that is representative of the field as a whole and stretch the line out across the crop rows. The line may be oriented perpendicular to the rows, or in a direction that is at least 45 degrees off the row direction (Figure 13). The locations in the field where the line is stretched out to make measurements should be selected randomly from among the areas of the field that are typical of the entire field. End rows, field borders, and parts of the field that appear different are probably not typical of the entire field and should be avoided.*

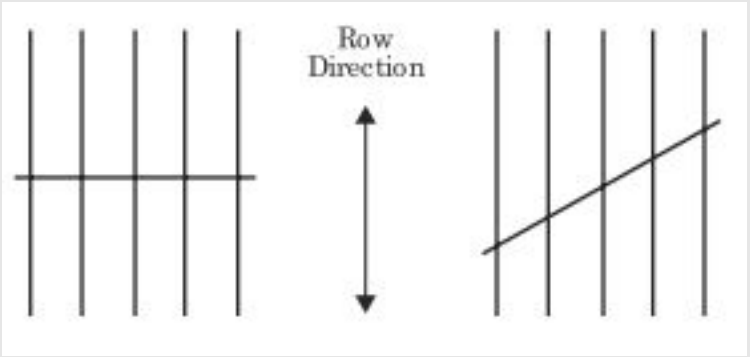


*Figure 13: Acceptable orientations for residue measurement lines.*

3. *Walk along the line, stopping at each mark. Position the eye directly over the mark, and look down at it. When sighting, do not look at the entire mark. Rather look at a single point on each mark. A point has an area*

28 Subpart 503E Crop residue, paragraph 503.43 Estimating crop residue cover. [USDA, 2002]
29 Equivalent to approximately 15 to 30 metres (respectively).

*about like the end of a needle. On commonly used equipment, the knots, beads, or gradations have much larger areas than the end of a needle. A measurement is not based on whether or not some portion of a mark is over the residue. It is based on whether or not a specific point associated with the mark is over residue. If using a commercially available beaded line, one way to accomplish the above is to select as the point of reference the place along the line where a bead begins.*

4. *Determine the percent residue cover by counting the number of points at each mark along the line under which residue is seen. Count only from one side of the line for the single, selected point count at each mark. Do not move the line while counting. Count only that residue that is large enough to intercept raindrops. A rule of thumb is to count only residue that is 3/32 inch[30] in diameter or larger (Figure 14). When using a line with 100 points, the percent residue cover is equal to the number of points under which residue is seen.*

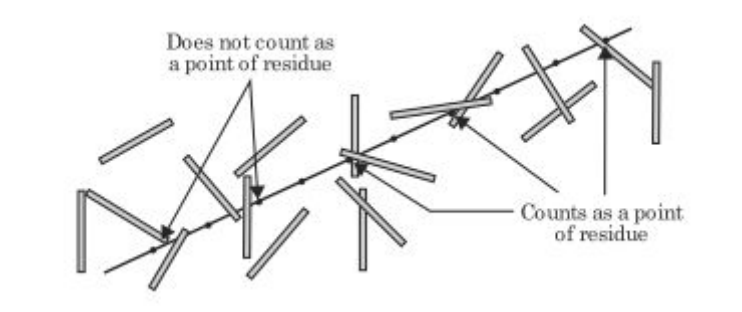


*Figure 14: Counting residue pieces along a line transect.*

5. *Three to five transects should be done in each field, using the procedure described in steps 1 through 4. Five transects are recommended. With five measurements, estimates of percent residue cover are accurate to within ±15 percent of the mean. Three measurements will give estimates accurate to within ± 32 percent of the mean. For example, if the mean of five measurements was 50 percent cover, you could be confident (at the 95% confidence level) that the true mean was between 42 percent and 57 percent cover. For a 30 percent cover average based on five measurements, you could be confident that the true value was between 25 percent and 34 percent cover.*
6. *The documentation of individual transects and computations made to determine average percent residue amounts should be done in a professional manner. Documentation should be done in a way that permits easy tracking from the field measurements to the final answer.*

*(source: USDA, 2002)*

With respect to the USDA method, because of the metric system in use in Italy and the conversion factor between foot and metre (1 foot = 0.3048 metres), it appeared appropriate to use a 20 metres plastic band for the surveys, with observations to be done at exactly 20 cm intervals. Therefore, a hundred points were sampled visually at the metre and at 20 cm, 40 cm, 60 cm and 80 cm on each location and the presence of residues was recorded on paper and then transferred onto a digital spreadsheet for processing.

Locations of each transect were recorded on a Garmin eTrex Legend Cx GPS device. Tracked points were later downloaded on PC, transformed into a point shapefile and appropriately reprojected for overlay on the farm's cadastral map in QGIS (Figure 15 and Figure 16).

Three to five samplings were surveyed for each field visited, depending on the size of the parcel and on the visual estimate of the homogeneity of the residues on the surface.

30 Equivalent to approximately 0.25 cm.

Not all the Bianchini farm's parcels were surveyed (with the line-transect method) on any of the three dates (Table 5). However, parcels excluded from field operations were visually inspected to estimate residue cover. This allowed to split the total number of parcels into two groups: a target group, consisting of the surveyed parcels used for retrieval of the mathematical relationship between residue cover and satellite imagery-derived values; and test group, for the validation of the mathematical relationship through regression. Such two groups were not of fixed composition (i.e. parcel id), but varied with the date of survey.

# *Results and discussion*

The complete list of acquisitions of Hyperion imagery has already been reported elsewhere (Table 4). Acquisitions occurred five times between August 2010 and September 2011 on the Lodi Vecchio portion of the Bianchini farm and ten times between July 2010 and September 2011 on the San Martino in Strada parcels. However, as expected for any optical sensor, cloud cover up to 90% severely limited the number of usable images, leaving out only ten cloud-free scenes overall. Furthermore, for best analysis of crop residues, the end of June beginning of July period for wheat and the September month for maize should have occurred. Instead, wheat harvest could no be observed directly in neither of the two farm's portions and on neither of the two years of acquisitions (2010-2011). Opposite to that, corn parcels enjoyed a number of acquisitions.

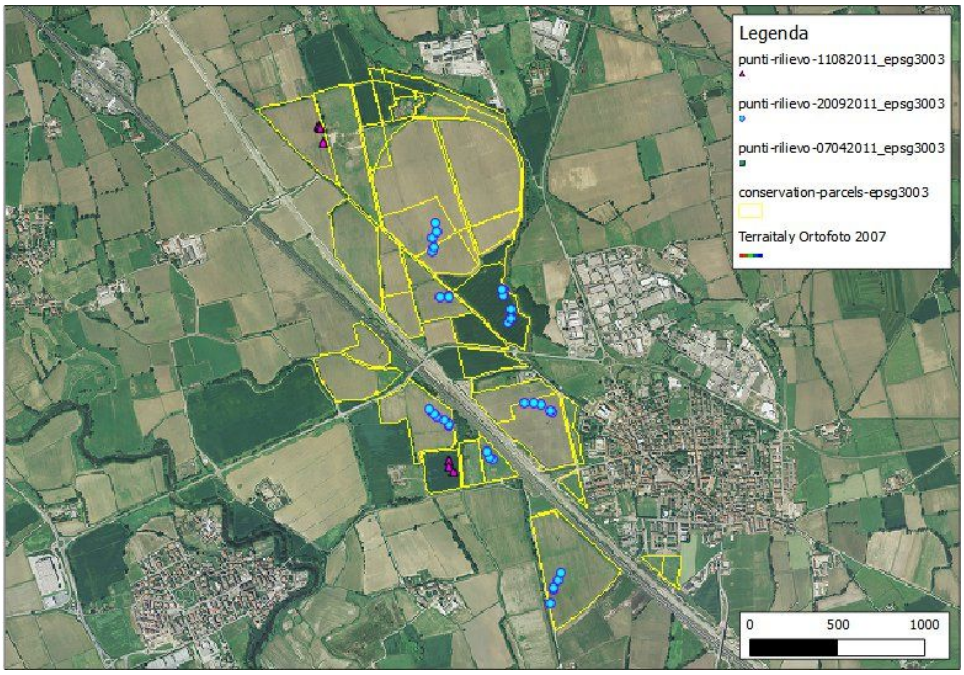


*Figure 15: Location of the surveys in the Lodi Vecchio area.*

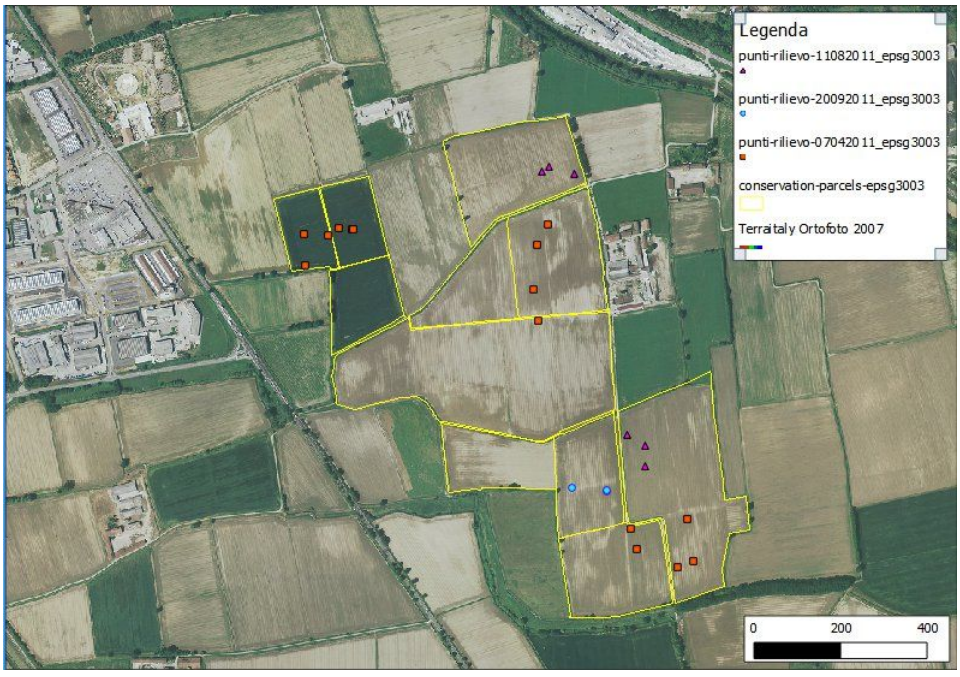


*Figure 16: Location of the surveys in the San Martino area.*

A total of 61 transects were carried out on both farm's units at Lodi Vecchio (Figure 15) and San Martino in Strada (Figure 16). Results of the field surveys are summarized in the following Table 5, where the percentage of residues cover is calculated as the sum of the points were residues were found to be present. The arithmetic mean for each parcel was then used as input in the investigation of the relationship with image pixel values in the same parcels.

| Crop type | wheat | | | | | | | | | | | | | | | | |
|---|---|---|---|---|---|---|---|---|---|---|---|---|---|---|---|---|---|
| Date of survey | 07/04/11 | | | | | | | | | | | | | | | | |
| Parcel name | Garibolde | | | | | c. Del miglio | | | | | Bescape | | | | | | |
| Parcel no. — Transect no. | SM4/23 – 1 | SM4/23 – 2 | SM4/23 – 3 | SM4/23 – 4 | SM4/23 – 5 | SM5/40 – 1 | SM5/40 – 2 | SM5/40 – 3 | SM5/40 – 4 | SM5/40 – 5 | SM6/18 – 1 | SM6/18 – 2 | SM6/18 – 3 | SM6/18 – 4 | SM6/18 – 5 | | |
| Cover (%) | 55 | 47 | 48 | 51 | 50 | 88 | 77 | 89 | 87 | 89 | 29 | 30 | 28 | 26 | 29 | | |
| Mean | 50 | | | | | 86 | | | | | 28 | | | | | | |

| Crop type | wheat | | | | | | | | | | | | | | | | |
|---|---|---|---|---|---|---|---|---|---|---|---|---|---|---|---|---|---|
| Date of survey | 11/08/11 | | | | | | | | | | | | | | | | |
| Parcel name | Avia | | | Bescape | | | Campagna | | | Giovacchino | | | | | | | |
| Parcel no. — Transect no. | SM5/23 – 1 | SM5/23 – 2 | SM5/23 – 3 | SM6/9 – 1 | SM6/9 – 2 | SM6/9 – 3 | LV1/7 – 1 | LV1/7 – 2 | LV1/7 – 3 | LV7/31 – 1 | LV7/31 – 2 | LV7/31 – 3 | | | | | |
| Cover (%) | 50 | 68 | 71 | 67 | 98 | 75 | 84 | 88 | 98 | 90 | 72 | 71 | | | | | |
| Mean | 63 | | | 80 | | | 90 | | | 78 | | | | | | | |

| Crop type | maize | | | | | | | | | | | | | | | | |
|---|---|---|---|---|---|---|---|---|---|---|---|---|---|---|---|---|---|
| Date of survey | 20/09/11 | | | | | | | | | | | | | | | | |
| Parcel name | Traversa | | | Fiorenza | | | | | Aglio | | | Cantorinone | | | | | |
| Parcel no. — Transect no. | SM6/20 – 1 | SM6/20 – 2 | SM6/20 – 3 | LV13/156 – 1 | LV13/156 – 2 | LV13/156 – 3 | LV13/156 – 4 | LV13/156 – 5 | LV7/107 – 1 | LV7/107 – 2 | LV7/107 – 3 | LV7/82 – 1 | LV7/82 – 2 | LV7/82 – 3 | LV7/82 – 4 | LV7/82 – 5 | |
| Cover (%) | 44 | 45 | 28 | 82 | 82 | 86 | 84 | 88 | 77 | 78 | 79 | 86 | 88 | 80 | 86 | 84 | |
| Mean | 39 | | | 84 | | | | | 78 | | | 85 | | | | | |

| Crop type | maize | | | | | | | | | | | | | | | | |
|---|---|---|---|---|---|---|---|---|---|---|---|---|---|---|---|---|---|
| Date of survey | 20/09/11 | | | | | | | | | | | | | | | | |
| Parcel name | Olmo Nuovo | | | | | Mariscone | | | | | Castagno | | | Fiori di Sotto | | | |
| Parcel no. — Transect no. | LV7/105 – 1 | LV7/105 – 2 | LV7/105 – 3 | LV7/105 – 4 | LV7/105 – 5 | LV3/19 – 1 | LV3/19 – 2 | LV3/19 – 3 | LV3/19 – 4 | LV3/19 – 5 | LV3/255 – 1 | LV3/255 – 2 | LV3/255 – 3 | LV1/20 – 1 | LV1/20 – 2 | LV1/20 – 3 | LV1/20 – 4 | LV1/20 – 5 |
| Cover (%) | 85 | 84 | 84 | 87 | 76 | 79 | 78 | 82 | 71 | 77 | 75 | 79 | 72 | 92 | 92 | 85 | 88 | 85 |
| Mean | 83 | | | | | 77 | | | | | 75 | | | 88 | | | | |

*Table 5: Summary table of all the field surveys carried out in the Bianchini farm. SM=San Martino in Strada. LV=LodiVecchio . Figures next to the location id indicate cadastral sheet, parcel number and survey's transect number respectively.*

The first survey (07/04/2011) followed the acquisition of an image on 22/03/2011 on the Lodi Vecchio area and observed the maize sowing phase as well as the rise of wheat on crop residues.

The second survey (11/08/2011) should have been carried out at the end of June/beginning of July to observe those parcels where wheat was being harvested. Unfortunately, as briefly mentioned above, no acquisition of imagery occurred in these nor in the following weeks and, by the date of the survey, a thick green grass had already re-grown on the harvested parcels. On the remaining cropped parcels, maize was still high and mostly green. However, the survey stood as a good check point in the agricultural operations, notably in the use of ex-wheat parcels for subsequent production of hay from (re-)growth of spontaneous vegetation.

The third survey (20/09/2011) matched both the double image acquisition of 09/09/2011 on the Lodi Vecchio area and of 27/09/2011 on the San Martino area as well as the harvesting of maize. This allowed for a complete overview on the entire range of the selected farms' parcels.

The sampling suffered from some objective difficulties. First, the maize crop stubbles were usually standing upward on the ground and very seldom they were found to having been mechanically flattened. This limited the possibility to stretch the transect plastic ribbon-meter along a straight line (Figure 17).

*Figure 17: An example of the difficulties met during in the sampling of residues: corn standing stubbles in the field. Photo taken on 20/09/2011 in Lodi Vecchio.*

Furthermore, residues were often mixed with spontaneous herbaceous vegetation. Due to the fact that the optical satellite sensors observe whatever is visible from above, sub-metre locations along the ribbon where green vegetation occurred were considered as no-residue, despite the fact that residues were frequently present under such green layer.

In the late September 2011 sampling, the spontaneous herbaceous vegetation grown on harvested wheat parcels had just been cut and removed for later use as hay, leaving a rather heterogeneous, brownish and short grass mat. A visual inspection of such parcels revealed a cover of 90% or more of the surface, but it remains questionable whether this type of cover is to be considered as made of residues.

An example of the relevant difference observed between parcels of the Bianchini farm under conservation agriculture and adjacent parcels of other farms under conventional agriculture is offered in Figure 18 and Figure 19. All photos were taken on the same day after a short rainfall event. In Figure 18 (Lodi Vecchio), photo A, surveyed corn residues cover the soil surface for 84% of its extent and no sign of stagnating water is visible, whereas in the adjacent conventional parcel (photo B), the visually estimated cover does not exceed 15% and precipitation water is clearly visible on the surface, indicating the soil has a reduced drainage capacity.

*A* *B*

*Figure 18: Example of adjacent parcels under CA and conventional farming.*
*A: Cadastral parcel 13/156 of the Bianchini farm (corn residues under conservation agriculture).*
*B: adjacent parcel (13/131) in another farm (corn residues under conventional farming).*
*Location: Lodi Vecchio. Both photos taken on 20/09/2011.*

*A* *B*

*Figure 19: Another example of adjacent parcels under CA and conventional farming.*
*A: Cadastral parcel 6/20 of the Bianchini farm (corn residues under conservation agriculture).*
*B: adjacent parcel in another farm (corn residues under conventional farming).*
*Location: San Martino in Strada. Both photos taken on 20/09/2011.*

Equally self-explanatory was the situation observed in the San Martino area (Figure 19), where residues cover both under conservation agriculture and conventional agriculture reached values very close to the previous case.

Mathematical processing of radiance from the Hyperion images for the Cellulose Absorption Indices according to the Monty, Guerschman and Serbin methods generated mean parcel values that were then compared with the ground based values of residue cover (or $f_R$ as per Table 5) for investigation on the relationship between the two. The series of plots below show the results of the comparison between the CAI values (as per the Monty, Guerschman and Serbin methods) and the ground-based crop residue cover values.

In order to calculate the regression equation, values of residues for bare soils (with a moderate degree of weed infestation) were set to zero, whereas those of set-aside parcels were set to null value.

From Figure 20 below, it can be observed that, for the case study examined and with the Monty-CAI method, CAI values are always negative but linearity is clearly present. However, when data from both the Lodi Vecchio and San Martino areas are considered together (Figure 20 - a), the coefficient of determination $R^2$ of 0.64 indicates a medium capability for the regression equation to predict unknown ground values. The coefficient greatly improves when the two areas are analysed separately. Indeed, $R^2$

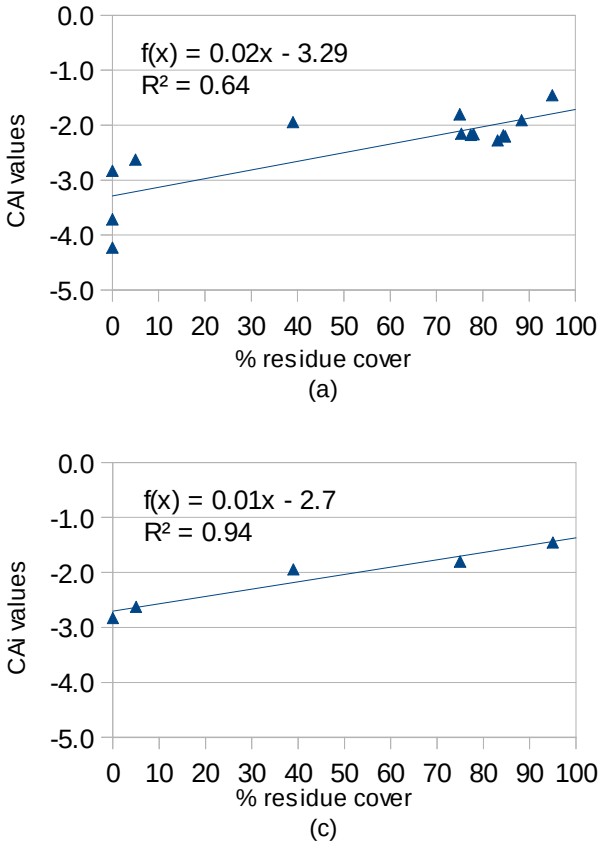


*Figure 20: Values of CAI-Monty vs the ground sampled cover of maize residues.*
*(a): both LodiVecchio and San Martino. (b): LodiVecchio. (c): SanMartino. Date survey: 20/09/2011. Image used for LodiVecchio: EO1H1930282011252110KZ (acquired 09/09/2011). Image used for SanMartino: EO1H1930282011270110PZ (acquired 27/09/2011). A linear trend line was fitted with the data and $f_R$ equation plus $R^2$ are shown above.*

reaches 0.96 for Lodi Vecchio (Figure 20 - b) and 0.94 for San Martino (Figure 20 - c).

It is also worth of noting that the regression line fitted through the data does not appear to have a constant slope nor intercept across the three cases. Because in both areas the crop is maize and the type of technique used is the same, this clearly indicates the presence of an external factor influencing the relationship.

The Guerschman-CAI, compared to the Monty-CAI, presents an even lower $R^2$ (0.1) that indicates a very low prediction capability of the linear relationship when residues from both the Lodi Vecchio and San Martino areas are considered together (Figure 21). However, a greater $R^2$ (0.97) is reached when the two portions of territory are analysed separately. A value of $R^2$ so close to 1 indicates an almost perfect prediction capability of the relationship.

Similarly to the Monty-CAI, the slope of the $f_R$ line fitted through the data appears to change in the three cases, although Guerschman-CAI values are much closer and above zero. Equally, the intercept of the trend line changes as well, confirming the presence of a hidden factor affecting the regression.

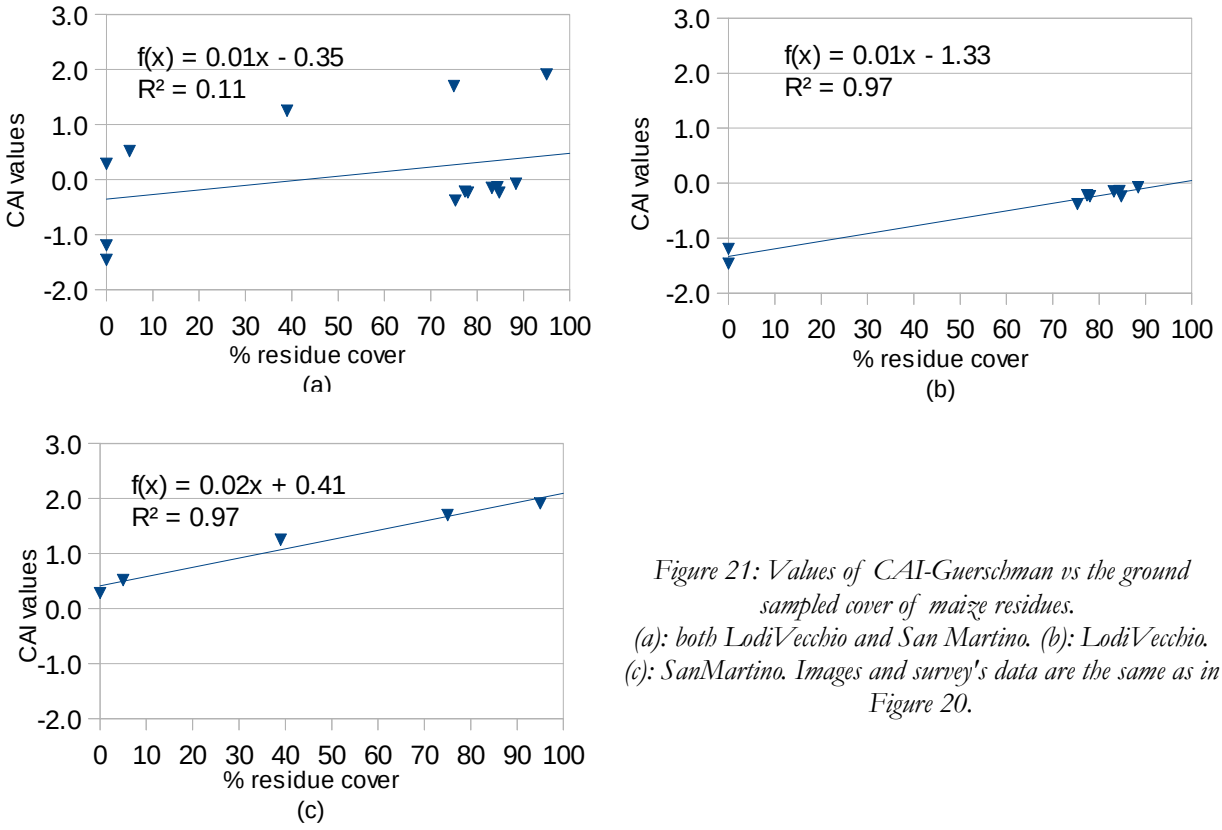


*Figure 21: Values of CAI-Guerschman vs the ground sampled cover of maize residues.*
*(a): both LodiVecchio and San Martino. (b): LodiVecchio. (c): SanMartino. Images and survey's data are the same as in Figure 20.*

The Serbin-CAI case (Figure 22) is similar to the Guerschman-CAI in the $R^2$ values and in the separability of residue covers the two farm-areas already when combined (Figure 22 - a).

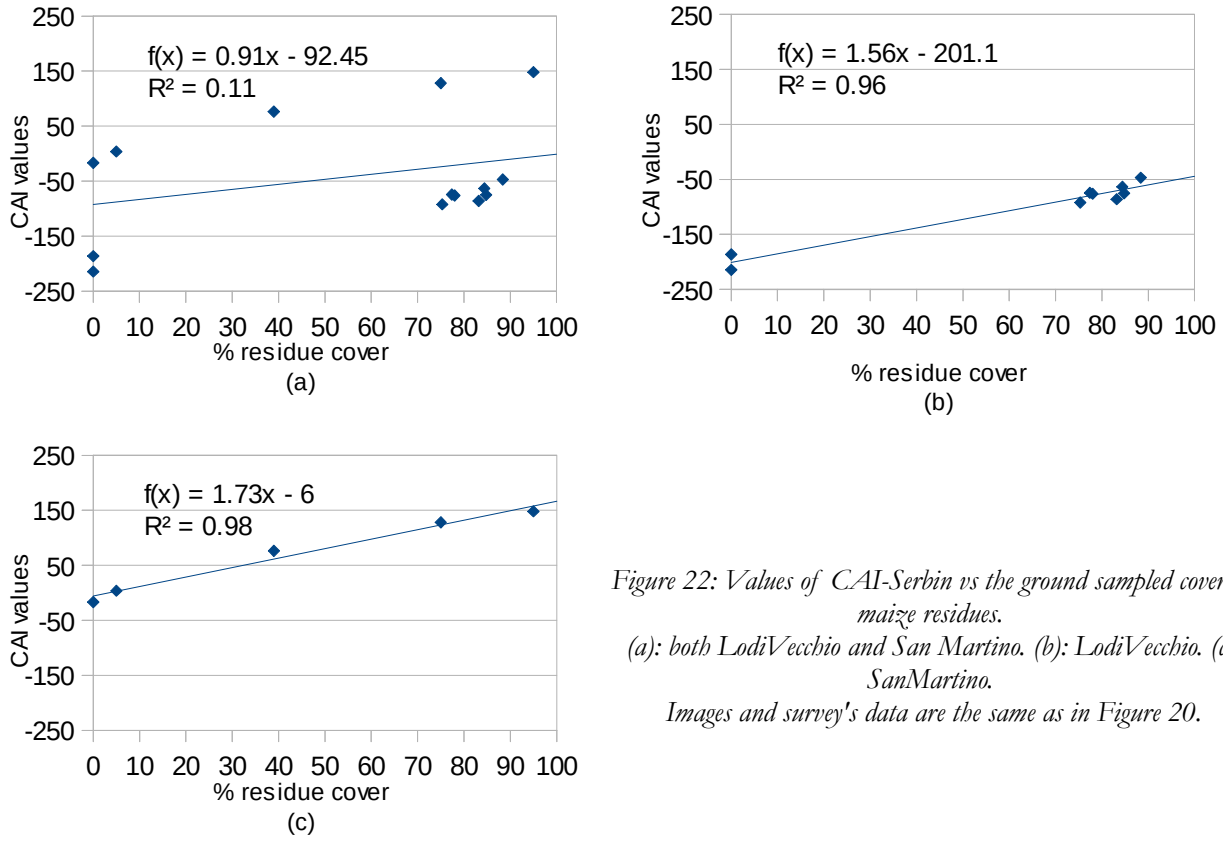


*Figure 22: Values of CAI-Serbin vs the ground sampled cover of maize residues.*
*(a): both LodiVecchio and San Martino. (b): LodiVecchio. (c): SanMartino.*
*Images and survey's data are the same as in Figure 20.*

In all three cases, it should be noted that intermediate values of ground residues are rather limited, therefore there is room for an improvement in the statistical significance of regression by widening the range of parcels surveyed.

Further investigation into the factors behind the variations of equation of the trend lines was considered. The influence of soils on CAI is to be excluded (as discussed above) in addition to the fact that soils in the two areas are similar. Furthermore, no difference can be noted in the type of cultivation techniques nor in the density of sowing.

Precipitations were then taken into consideration. Meteorological data from the ARPA Lombardia meteorological database [ARPA, 2011] were extracted for the three stations closest to the study area (Cavenago d'Adda, Lodi (ERSAF) and Sant'Angelo Lodigiano)(Figure 23).

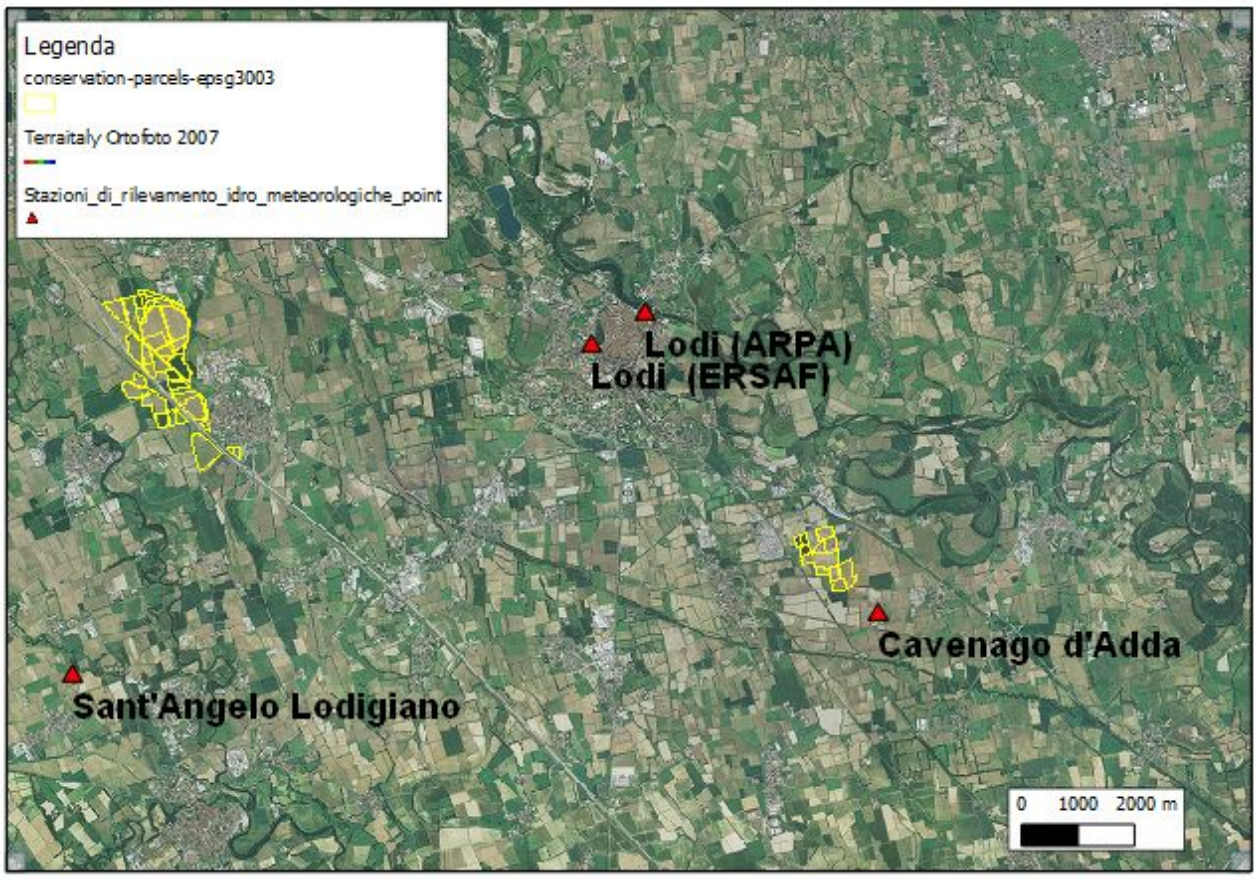


*Figure 23: Location of the ARPA weather stations closest to the study area (parcels in yellow). The Lodi Vecchio portion of the Bianchini farm is on the left. San Martino, on the right. Source of the weather station locations: ARPA, 2011. Orthophoto TerraItaly 2007 WMS: Provincia di Lodi, 2011.*

Data retrieved (Figure 25) revealed that a significant rainfall event occurred on September 1 through 5, but it was only recorded by the Lodi (ERSAF) station as the other two stations report incomplete data for the same dates (subject to manual editing at a later stage). Such rainfall is compatible with the effects of "darkening" in the Hyperion acquisition of September 9 and with the downward shift of the trend line, confirming similar literature findings (Daughtry and Hunt, 2008; Bannari et al., 2007b).

Another rainfall event occurred on September 16 through 20, seven days before the Hyperion acquisition on September 27, but with much reduced amount of precipitation with respect to the previously cited event. Furthermore, the high temperatures in that period of the year seem to have dried the soil up as the San Martino CAI values appear consistent to literature data on dry soils.

Further literature research revealed that Daughtry and Hunt, 2008, in a series of experiments with laboratory reflectance data, found the $R_{2.2}/R_{2.0}$ ratio (Reflectance Ratio Water Index, RRWI) indicative of soil+residues moisture and somewhat linearly related to the slope of the residues vs CAI values, making it possible to adjust the residues/CAI equation based on actual moisture content. $R_{2.2}$ and $R_{2.0}$ represent the same wavelenghts used to calculate CAI (10 nm-wide bands centered at 2210 nm and 2030 nm respectively according to the authors) and are based on the fact that as water content increases, reflectance of residues at 2030 nm is attenuated with respect to reflectance at 2210 nm. Further data analysis was then performed to assess whether such relationship held true for the present case study. In addition to the September double acquisition and field sampling, data from the March/April acquisition/sampling (wheat+maize residues) were processed to work out the regression

line's slope and the RRWI value. No other image, despite being available, was matched by other field samplings. Therefore, there were only three points at disposal to build the relationship (Figure 24). For RRWI, Hyperion bands no.154 (band number after MNF transform, centered at 2213.93 nm and corresponding to original band no.206) and no. 136 (centered at 2032.35 nm, corresponding to original band no.188) were used.

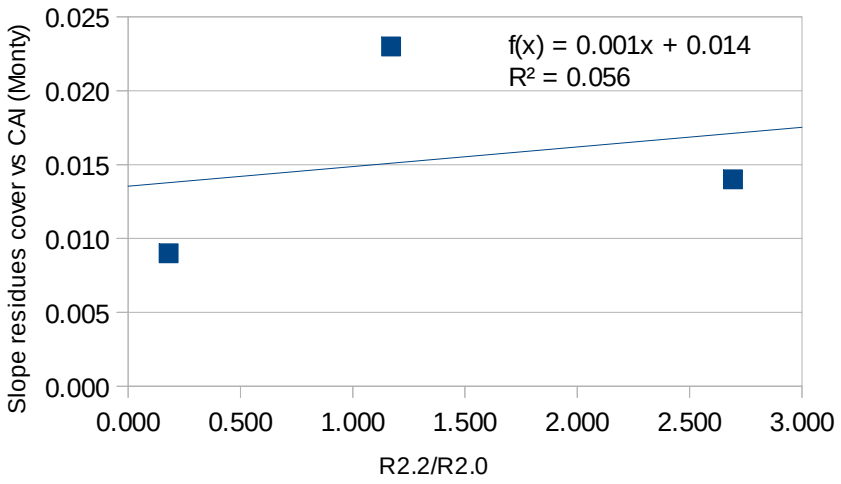


*Figure 24: Slope of residue cover vs CAI as a function of the RRWI ($R_{2.2}/R_{2.0}$)*

As it can be observed from the figure above, RRWI (in the current formulation) does not appear as a valid factor to explain variations in the equations linking residues to CAI (Figures 20-22). However, this could be due to a number of reasons, such as the limited number of sampling dates, the mixture of crop residues (wheat+corn) and the noise contained in the imagery with respect to laboratory reflectances of the original study [Daughtry and Hunt, 2008], despite the preprocessing of the Hyperion imagery described above. Furthermore, should the RRWI method be verified, it would only offer a solution to linking residue moisture content to the slope of the $f_R$ equation, leaving out the determination of the intercept.

Independently of rainfall events, and therefore of soil+residue moisture content, the question now arises on which of the three CAI methods is the most reliable for determining residue cover. By use of the above regression equations and of the CAI values as independent variables, it is possible to calculate values of residue cover (dependent variables) on parcels where such values were only assessed visually. Ideally, a cross-check with surveyed residue values not already employed for the retrieval of the regression equation should have been used, but the number of surveyed parcels is not sufficient for such an operation.

Excluding the equations with minimal prediction capability (e.g. Guerschmann and Serbin equations for the two areas together), the other four equations were used to calculate the regressed values of residues as reported in Table 6 below. The "expected values" are those assumed from adjacent parcels of the same type and management or esteemed after visual inspection in the field.

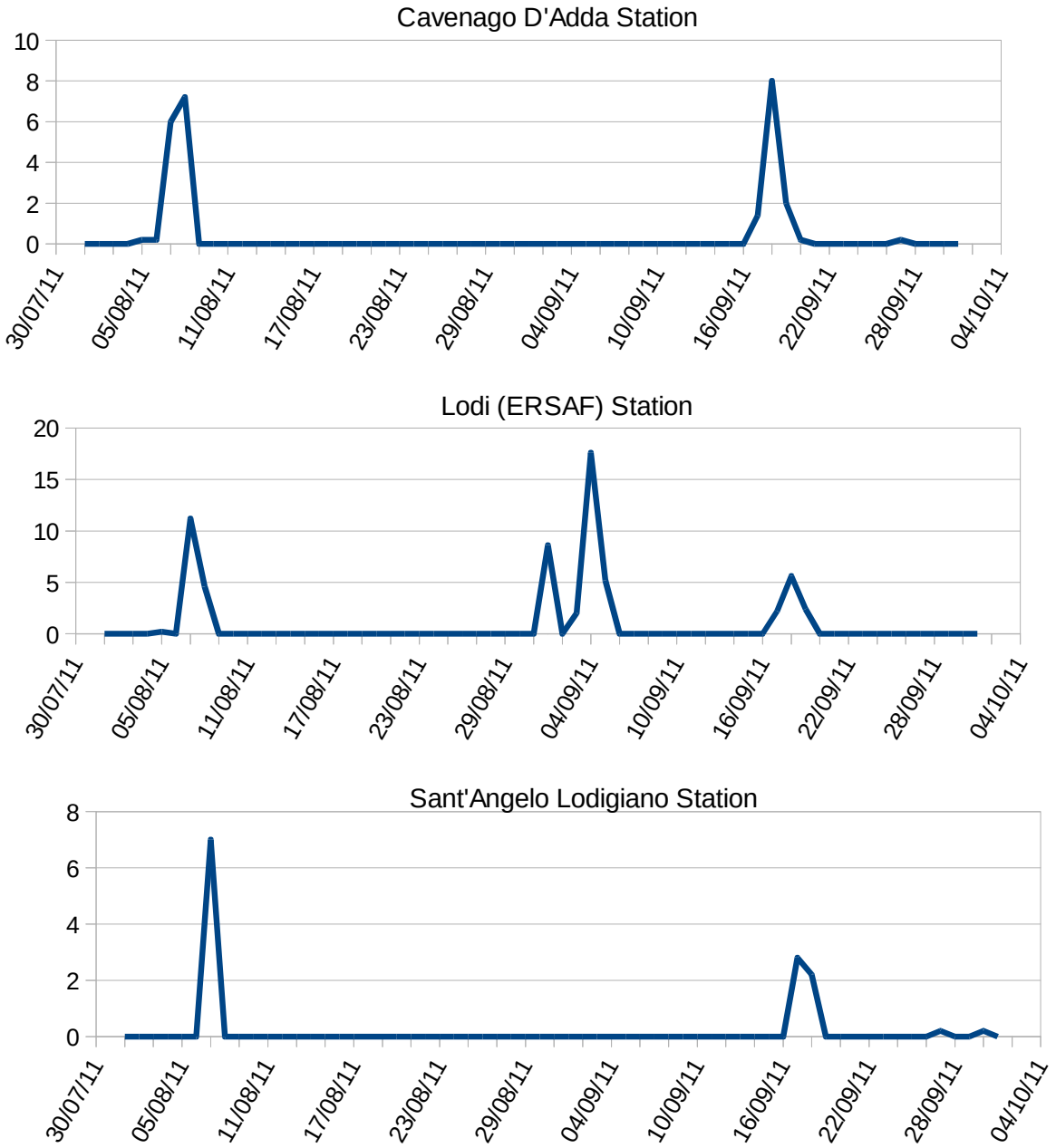


*Figure 25: Pluviometry of the three meteorological stations nearest to the study area. Cavenago d'Adda station is the nearest to San Martino in Strada,. The other two are almost equidistant and the nearest to the Lodi Vecchio farm.*

Parcel 13/131 can be considered representative of a harvested maize under conventional agriculture , while parcel 13/133 indicates a parcel with standing mature (brown) maize under conventional agriculture (expected approximately 90% cover). Both parcels are adjacent to the Bianchini farm but not part of it.

Although the "expected values" may not be necessarily consistent with the ground-based truth (because not surveyed with transects, but only visually estimated), an analysis of the above results suggests that the Monty regression tends to severely underestimate the correct values (RMSE=14.1), whereas the Guerschman-LV $f_R$ equation overestimates high values and underestimates low values (RMSE=13.4).

In general, it can be observed that values above 100 should be rejected as they would represent a residue cover greater than the available surface. For the same reason, the Monty-LV $f_R$ equation should be considered with care (RMSE=18.4).

| **Parcel name** | **Granmigne** | **Campazzino** | **Cantorinetto** | **Fopa** | **Olmo Nuovo** |
|---|---|---|---|---|---|
| **Parcel no.** | **2/10 + 2/71** | **3/7** | **7/77** | **2/24** | **7/105** |
| **Crop:** | maize | maize | maize | maize | maize |
| **Expected values** | 75 | 75 | 85 | 85 | 83 |
| **Notes** | Assumed 3/255 | Assumed 3/255 | Assumed 7/82 | Assumed 3/255 | Assumed 7/115 |
| **Monty** | 72 | 49 | 52 | 54 | 64 |
| **Monty – LV** | 105 | 83 | 86 | 88 | 98 |
| **Guerschman – LV** | 124 | 94 | 114 | 119 | 126 |
| **Serbin – LV** | 90 | 72 | 89 | 93 | 93 |

| **Parcel name** | **Orti** | **Orti** | **Pivot Grande** | **13/131** | **13/133** |
|---|---|---|---|---|---|
| **Parcel no.** | **1/4** | **1/3** | **1/21** | | |
| **Crop:** | maize | maize | maize | maize | maize |
| **Expected values** | 88 | 88 | 88 | 15 | 90 |
| **Notes** | Assumed 1/20+1/21 | Assumed 1/20+1/21 | Assumed 1/20+1/21 | Visually estimated | Visually estimated |
| **Monty** | 35 | 56 | 68 | -21 | 47 |
| **Monty – LV** | 68 | 89 | 101 | 12 | 81 |
| **Guerschman – LV** | 120 | 131 | 125 | 3 | 119 |
| **Serbin – LV** | 84 | 97 | 98 | 7 | 87 |

*Table 6: Values of residues estimated with the indicated equations and respective CAI values for the Lodi Vecchio (LV) area. Equations are as following: Regression Monty: Figure 20-a; Monty – LV: Figure 20-b; Guerschman – LV: Figure 21-b; Serbin – LV: Figure 22-b.*

On the other hand, values calculated with the Serbin-LV $f_R$ equation appear to well fit with the expected data across the different parcels (RMSE=9.9). As far as the absolute values are concerned, it can be noted that the minimum residue cover requirement of the conservation agriculture principles are always respected, with crop residue covers well above 30%. This is clearly not the case of the parcels under conventional agriculture (with a calculated cover of less than 10%). However, the lack of intermediate cover values does not allow further speculations on the accuracy of the proposed regression.

It is also interesting to take a look at the values calculated with the above equations for set-aside parcels (dominated by spontaneous herbaceous vegetation), for parcels with a harvested grass mat following cultivation of wheat and for parcels with bare soil (with a variable presence of green weeds)(Table 7).

| Parcel name | cant Bassi | cant Bassi | cant Valle | cant Lungo Silaro | cant Giovacchino | Sstef Fiori di sopra |
|---|---|---|---|---|---|---|
| Parcel no. | 14/293 | 14/295 | 13/177 | 7/97 | 7/31 | 1/20 |
| Survey 20/09/11 Crop: | set aside | set aside | set aside | set aside | grass (ex wheat) | grass (ex wheat) |
| Expected values | NA | NA | NA | NA | NA | NA |
| Notes | | | | | | |
| Monty | 31.49 | 17.61 | 1.2 | 13.14 | 37.75 | 38.39 |
| Monty – LV | 64.99 | 51.11 | 34.7 | 46.64 | 71.25 | 71.89 |
| Guerschman – LV | 118.75 | 105.56 | 84.01 | 92.71 | 127.84 | 147.32 |
| Serbin – LV | 86.21 | 73.52 | 55.75 | 65.21 | 86.5 | 94.91 |

| Parcel name | cant Bianchino | gabazzino | cant Leonardo | sstef Partitora | cant Gabazza |
|---|---|---|---|---|---|
| Parcel no. | 7/36 | 2/11 | 3/274 | 1/8 | 2/98 |
| Survey 20/09/11 Crop: | bare soil (+weeds) | bare soil (+weeds) | bare soil (+weeds) | bare soil (+weeds) | bare soil (+weeds) |
| Expected values | 0 | 0 | 0 | 0 | 0 |
| Notes | Visually estimated | Visually estimated | Visually estimated | Visually estimated | Visually estimated |
| Monty | -50.19 | -21.24 | -46.95 | -44.23 | -42.34 |
| Monty – LV | -16.69 | 12.26 | -13.45 | -10.73 | -8.84 |
| Guerschman – LV | -5.55 | 13.39 | -13.2 | -17.2 | -25.42 |
| Serbin – LV | -8.12 | 9.4 | -8.62 | -9.85 | -15.83 |

*Table 7: Values of residues estimated with the indicated equations and respective CAI values for the Lodi Vecchio (LV) area. Equations are as following: Regression Monty: Figure 20-a; Monty – LV: Figure 20-b; Guerschman – LV: Figure 21-b; Serbin – LV: Figure 22-b.*

From the table above, it can be observed that the bare soil parcels are generally well characterized in all the equations, with mostly negative values, whereas the ex-wheat and set-aside parcels seem to indicate an extraordinary presence of residues in all $f_R$ equations excluding Monty (and the untrustworthy Guerschman-LV). These results appear to suggest that the examined CAI-based methods are able to correctly separate bare-soil parcels from vegetated or cultivated ones, but they are not be particularly useful to segregate parcels with residues from parcels under set-aside or dominated by a mat of grass (like in the case of the Bianchini farms, the latter are parcels previously cultivated with wheat). However, values for these parcels suggest a good or excellent soil cover, whose assessment is very relevant for the protection of soil resources.

The same considerations hold true for the San Martino area, where similar findings can be highlighted (Table 8, Table 9 and Table 10).

| Parcel name | Traversa | Traversa | c del Miglio | c del Miglio | c del Miglio |
|---|---|---|---|---|---|
| Parcel no. | 6/20 | 6/7 | 6/2 | 5/64 | 5/40 |
| Crop: | maize | maize | maize | maize | maize |
| Expected values | 39 | 39 | 95 | 95 | 95 |
| Notes | Sampled | Assumed 6/20 | Visually estimated | Assumed 6/2 | Assumed 6/2 |
| Monty | 86 | 91 | 111 | 88 | 99 |
| Monty – SM | 75 | 85 | 125 | 79 | 101 |
| Guerschman – SM | 42 | 38 | 75 | 47 | 56 |
| Serbin – SM | 48 | 42 | 89 | 55 | 66 |

*Table 8: Values of residues estimated with the indicated equations and respective CAI values for the San Martino (SM) area. Equations are as following: Regression Monty: Figure 20-a; Monty – SM: Figure 20-c; Guerschman – SM: Figure 21-c; Serbin – SM: Figure 22-c.*

Serbin-CAI values (55% and 66%) for the last two parcels (5/64 and 5/40) in Table 8 above seem to depart considerably from the expected cover values (both 95%). However, the latter were assumed based on the vicinity and type of crop of parcel 6/2, that was instead visually assessed. Serbin-CAI value for parcel 6/2, indeed, shows a much better matching with the expected value. This seem to suggest that more caution should be applied in extending surveyed crop residue cover values to "similar" parcels, as this can be misleading due to unexpected heterogeneity within the unsurveyed parcels. Therefore, at the time the mathematical model is built, all the parcels should be sampled carefully.

| **Parcel name** | **SM5/24** | **SM5/38** | **SM6/3** | **SM4/21+4/22** |
|---|---|---|---|---|
| **Parcel no.** | | | | |
| **Survey 20/09/11. Crop:** | bare soil (+weeds) | harrowed | maize | maize |
| **Expected values** | 0 | 5 | 10 | 75 |
| **Notes** | Visually estimated | Visually estimated | Visually estimated | Visually estimated |
| **Monty** | 42 | 52 | 48 | 93 |
| **Monty – SM** | -13 | 7 | -2 | 90 |
| **Guerschman – SM** | -6 | 5 | -21 | 64 |
| **Serbin – SM** | -6 | 6 | 33 | 77 |

*Table 9: Values of residues estimated with the indicated equations and respective CAI values for the San Martino (SM) area. Equations are as following: Regression Monty: Figure 20-a; Monty – SM: Figure 20-c; Guerschman – SM: Figure 21-c; Serbin – SM: Figure 22-c.*

All the parcels in Table 9 above are external to the Bianchini farm, but adjacent to it and were taken as representatives of fields under conventional agriculture soon after harvesting. Parcel SM6/3 is the one depicted in Figure 19 - B, whereas parcel SM5/38 and SM5/24 are depicted in Figure 26 and Figure 27 respectively.

With regard to parcel SM6/3 it can be noted that the difference between the CAI value and the estimated value is quite large. However, by looking at the above Figure 19 - B, it can be observed that several bales of hay were collected on that parcel that could be held responsible for having increased CAI values compared to those visually estimated and therefore having "mislead" satellite observation.

*Figure 26: Parcel 5/38 in the San Martino area, while harrowing was under way (photo taken 20/09/2011).*

*Figure 27: Parcel 5/24 in the San Martino area.*
*Ploughed some weeks before photo was taken (20/09/2011).*

For the ex-wheat parcels, Serbin-CAI values seem to confirm a good or excellent crop residue soil cover, ranging from 38 to 73% of the surface (Table 10).

| **Parcel name** | **Avia** | **Bescape** | **Bescape/Traversa** | **Garibolde** | **Garibolde** | **Garibolde** |
|---|---|---|---|---|---|---|
| **Parcel no.** | **5/23** | **6/9** | **6/17+6/18** | **4/24** | **4/23** | **4/30** |
| **Crop:** | grass (ex wheat) | grass (ex wheat) | grass (ex wheat) | grass (ex wheat) | grass (ex wheat) | grass (ex wheat) |
| **Expected values** | NA | NA | NA | NA | NA | NA |
| **Notes** | | | | | | |
| **Monty** | 92 | 102 | 96 | 106 | 102 | 107 |
| **Monty – SM** | 86 | 106 | 96 | 115 | 106 | 118 |
| **Guerschman – SM** | 36 | 45 | 46 | 59 | 57 | 63 |
| **Serbin – SM** | 38 | 50 | 54 | 68 | 68 | 73 |

*Table 10: Values of residues estimated with the indicated equations and respective CAI values for the San Martino (SM) area.*
*Equations are as following: Regression Monty: Figure 20-a; Monty – SM: Figure 20-c;*
*Guerschman – SM: Figure 21-c; Serbin – SM: Figure 22-c.*

# *Conclusions*

The present research demonstrated that an expert use and attentive processing of Hyperion satellite imagery represents a viable solution to the problem of determining the degree of crop residues soil cover over vast areas. Compared to the field-based sampling methods, remote sensing methods appear to be more objective in predicting residue cover. The Cellulose Absorption Index (CAI) has confirmed its usefulness in this sense, in particular in the formulation proposed by Serbin at al., 2009a.

However, sensitivity of the linear relationship between residues and satellite imagery-based CAI to small variations in the amount of residue content and to soil and residues water content was noted, that requires a careful calibration of the method. Consequently, field samplings for the establishment of the mathematical relationship should be carried out as completely and precisely as possible. Furthermore, it is essential to take rainfall events into consideration in order to account for the change in residues (and soil) colour when wet, which deeply influences the above relationship. The relationship between residues water content and slope of the $f_R$ equation proposed by Daughtry and Hunt, 2008, could not be verified, possibly due to the limited amount of field sampling collected in the present study.

Results will hopefully be of great interest to researchers and modellers of soil erosion and $CO_2$ related phenomena, but also to public institutions in charge of verifying the application of obligations related to cross-compliance or rural development measures. Knowledge on the percent of cover by crop residues could also contribute to the calculation of the balance of carbon (C) stored annually in the soil as a result of agricultural activities, notably in the conservation agriculture domain.

The Bianchini farm applies reduced tillage extensively, with little long-term accumulation of litter on the soil surface, typical, instead, of the no-till farms. It was observed, however, that the release of a thick layer of residues after harvesting (as part of the broader conservation agriculture system) contributes to a better infiltration of rainfall waters and therefore to reduce run-off, soil erosion and soil crusting compared to adjacent parcels under conventional agriculture. Certainly, the use of more elaborated crop rotations could further contribute to an even greater level of protection through the crops' green canopies, to a better use of resources, and to a possible reduction in the use of fertilizers and pest repellent chemicals.

Despite the fact that the EO-1 satellite was launched as an experimental mission and that the Hyperion sensor has already passed its tenth year of operation, this sensor still offers valuable data for environmental studies. It is hoped that the release of soil data from public sources such as the JRC – LUCAS could finally allow for even broader researches on soils through chemometric modelling.

The present research could also represent a valid support in the use of other hyperspectral data in view of the next round of new sensors planned for launch in the near future with the provision of an open-source script for a very effective destriping of the imagery. As for all the passive sensors, however, the careful timing of acquisition is fundamental for a correct and reliable determination of residues cover and to avoid that an excessive growth of green vegetation could partly or totally mask the residues at later stages of the season. Inappropriate dates of acquisition have indeed limited the results of the present research.

In comparison with sensor aboard of planes, satellite imagery may suffer additional constraints, such as from heavy interference from a thicker atmospheric column and cloud cover. However, satellites observe much larger areas and at a minimal costs.

Additional research is suggested to quantify residues cover with more accuracy and to better define how soil and residue moisture affect the residues/CAI relationship from a mathematical standpoint, possibly by establishing a trustworthy residue water index.

It was observed in literature that the use of spectral unmixing techniques based on the quantification of the amount of pure end member spectra within each pixel of an image could improve the results of the CAI. The lack of a field spectrometer with resolution and bandwidths similar to those of Hyperion

as well as the lack of an open database of spectral reflectance of agriculture related materials, such as grasslands, green and dried crop residues, soils has prevented this possibility.

The research has also contributed to the advancements in the use and processing of remote sensing imagery by showing that the use of open source software is not only possible, but also of great help in solving complex problems, like in the case of destriping and geolocation of the Hyperion scenes.

# *Annex I*

## Chemometric modelling for the determination of soil organic carbon

The present annex contains a short summary of the information collected from various sources concerning the establishment and validation of chemometric models for the determination of soil organic carbon (SOC). Part of a wider research aimed at measuring variations of SOC in conservation agriculture farms from remote sensing, chemometric modelling could not be performed due to insuperable restrictions in the access to existing soil spectral and analytical data (LUCAS project, EUROSTAT/JRC-IES), an essential prerequisite to perform the modelling.

Reflectance spectra of soils represent a very rich source of information that allows inferring soil chemical, physical or biological properties through chemometrics. The latter is defined by the International Chemometrics Society as "the science of relating measurements made on a chemical system or process to the state of the system via application of mathematical or statistical methods"[Hibbert et al., 2009]. A possibly more illuminating definition states that chemometrics is a collection of "multivariate methods of data analysis applied to data of chemical interest" [Mark and Workman, 2007]. Many other definitions and variants may yet be found in the literature [Hibbert et al., 2008].

Multivariate (calibration)[31] methods include, among others, the following:

- Multiple Linear Regression (MLR) [Ben-Dor et al., 1991; Kemper and Sommer, 2002][32];
- Principal Component Regression (PCR) [Chang et al., 2001[32]];
- Partial Least Square Regression (PLSR) [Cozzolino and Morón, 2006; Reeves et al., 2002; McCarty et al., 2002; Masserschmidt et al., 1999; Kooistra et al., 2003; Cohen et al., 2005][32];
- Artificial Neural Networks (ANN) [Fidêncio et al., 2002; Udelhoven and Schütt, 2000][32].

The goal of calibration is to establish a mathematical model (relationship) for predicting the amount of a chemical compound of interest from a type of measurement that is cheaper, faster, or better accessible (yet sufficiently accurate) than the one(s) used to build the model itself.

Multiple Linear Regression (MLR) attempts to describe the relationship between several independent (or predictor) variables X and a dependent (or criterion) variable Y by fitting a linear equation (of the following type) to the observed data [StatSoft Inc., 2011]:

$Y = a + b_1*X_1 + b_2*X_2 + ... + b_p*X_p + e$

where:
a = regression constant
$b_1$, $b_2$, $b_p$ = (partial regression) coefficients of the $X_1$, $X_2$, $X_p$ predictors
e = residual (error)

MLR is based on least squares, i.e. the line is fit such that the sum-of-squares of differences of observed and predicted values is minimized [Meko, 2011].

31 Multivariate calibration refers to the establishment of a method for manipulating many measured properties (independent or predictor variables) of a chemical system simultaneously for quantifying one or more properties of interest (dependent variables). For example, the measured variables could be spectroscopy measurements and the target variable the concentration of a solute [Martens and Naes, 1992].

32 As cited in Boettcher et al., 2008.

Principal Component Regression (PCR) is a type of regression analysis that uses Principal Components Analysis (PCA) to estimate the regression coefficients. PCA is a statistical technique that linearly transforms an original set of highly correlated variables into a substantially smaller set of uncorrelated variables (the "principal components") that represents most of the information in the original set of variables [Dunteman, 1989]. With PCR, regression is operated on the principal components, in place of the independent variables, so that the noise characterizing the latter is removed without reducing the information explained.

In common with PCR, Partial Least Squares Regression (PLSR) constructs new predictor variables, (or "latent" components) as linear combinations of the original highly correlated predictor variables. However, differently from PCR, PLSR takes the response variable into account, very often leading to the determination of fewer components for the same data [The MathWorks Inc., 2011]. PLSR can be carried out following a number of different algorithms.

Artificial Neural Networks (ANNs) are mathematical systems made of a group of interconnected artificial neurons or "nodes" that emulate the biological neural mechanisms. ANNs are adaptive systems, in the sense that they undergo a "learning phase" through which they change structure based on external or internal information that flows through the network. ANNs can used in a variety of domains to model complex relationships between inputs and outputs or to identify patterns in data [Gershenson, 2003; Rios, 2011].

Numerous studies can be found in literature dealing with the use of diffuse reflectance spectroscopy in the visible (VIS), Near Infra Red (NIR) and Medium Infra Red (MIR) regions for the prediction of several soil properties through multivariate calibration [Ben-Dor et al., 2009]. Some of these deal specifically with the determination of SOC/SOM content [Masserschmidt et al., 1999; Reeves et al., 2002; Fidêncio et al., 2002; Cozzolino and Morón, 2006; Stevens, 2008][33].

Soil Organic Matter (SOM) influences the reflectance response of soil. Organic Matter (OM) is usually measured as organic carbon (OC), which is more clearly definable and measurable with less uncertainty. The OC values are converted to OM using a standard conversion ratio OC:OM of 1:72, considered satisfactory for broad scale environmental assessments and monitoring [Boettcher et al., 2008].

Boettcher et al., 2008, successfully established a chemometric model for the determination of SOC in arable land from proximal spectroscopy and then employed the model for predicting SOC in a study area by use of satellite remote sensing. To calibrate the model, they applied PLSR to a training set of N observations (soil samples) with K X-variables (spectral bands in the range 0.4 - 2.5 nm) and M Y-variables (soil constituents). These training data formed the matrices X and Y with dimensions (N*K) and (N*M), respectively. The accuracy attained by the model reached $R^2$=0.75 for SOM and $R^2$=0.85 for total carbonates.

Their study pursued the following steps: pre-processing of the spectroscopy data (standardisation, vector-normalisation and extraction of first order derivatives), application of PLSR on each of the four pre-processed sets of data and the soil analytical data to calibrate four chemometric models, including outliers detection and removal, and validation.

Standardisation and vector-normalisation prevent that large differences in the standard deviations of the variables could cause numerical instability and dependence on the scale used for the variables [Höskuldsson, 2004].

Derivatives of VIS/NIR sample spectra carry predominantly chemical information as albedo effects

33 As cited in Boettcher et al., 2008.

are reduced and overlapping spectral features are resolved. For example, soil OH absorption becomes visible as a distinct peak at 1400 nm only in the second derivative of the soil spectrum [Boettcher et al., 2008].

The study concluded that chemometric models built with first order derivatives achieve a higher determination coefficient score in discriminating SOM and total carbonates than with other types of data pre-processing (standardisation and vector-normalisation). It was also ascertained, through spectral degradation of the soil data, that out of the three satellite sensors considered (Landsat TM, MERIS, MODIS), only MERIS could potentially be employed to successfully build chemometric model capable of estimating the SOM. No other sensor, nor soil parameter (including total carbonates) can be modelled due to the low spectral range detected by this sensor.

Gomez et al., 2008, carried out a similar research in a study area in Australia, building chemometric models by use of SOC content data of a number of soil samples on the one hand and soil spectra taken in the field with a portable spectrometer on the other hand, along with soil spectra from the satellite Hyperion sensor. The authors ascertained that prediction of SOC using the Hyperion spectra was possible although less accurate than those of the field spectrometer data. This would suggest a potential for the use of hyperspectral remote sensing for predictions of soil organic carbon.

Other studies dealing with chemometric modelling for the determination of SOC/SOM from a variety of spectral sensors are presented hereafter as a series of (publicly available) abstracts from papers retrieved during the bibliographic search.

**Stevens, A., Udelhoven, T., Denis, A., Tychon, B., Lioy, R., Hoffmann, L., van Wesemael, B., 2010. Measuring soil organic carbon in croplands at regional scale using airborne imaging spectroscopy. Geoderma 158 (2010) 32–45**

Conventional sampling techniques are often too expensive and time consuming to meet the amount of data required in soil monitoring or modelling studies. The emergence of portable and flexible spectrometers could provide the large amount of spatial data needed. In particular, the ability of airborne imaging spectroscopy to cover large surfaces in a single campaign and to study the spatial distribution of soil properties with a high spatial resolution represents an opportunity for improving the monitoring of soil characteristics and soil threats such as the decline of soil organic matter in the topsoil. However, airborne imaging spectroscopy has been generally applied over small areas with homogeneous soil types and surface conditions. Here, five hyperspectral images acquired with the AHS-160 sensor (430 nm–2540 nm) were analysed with the objective to map soil organic carbon (SOC) at a regional scale. The study area, covering a surface of ~420 $km^2$ and located in Luxembourg, is characterized by different soil types and a high variation in SOC contents. Reflectance data were related to surface SOC contents of bare croplands by means of 3 different multivariate calibration techniques: partial least square regression (PLSR), penalized-spline signal regression (PSR) and support vector machine regression (SVMR). The performance of these statistical tools was tested under different combinations of calibration/validation sets (global and local calibrations stratified according to agro-geological zones, soil type and image number). Under global calibration, the Root Mean Square Error in the Predictions reached 5.3–6.2 g C $kg^{-1}$. Under local calibrations, this error was reduced by a factor up to 1.9. SOC maps of bare agricultural fields were produced using the best calibration model. Two map excerpts were shown, which display intra- and inter-field variability of SOC contents possibly related to topography and land management.

**Aïchi, H., Fouad, Y., Walter, C., Viscarra Rossel, R.A., Chabaane, Z.L., Sanaa, M., 2009. Regional predictions of soil organic carbon content from spectral reflectance measurements. Biosystem Engineering 104 (2009) 442–446**

Diffuse reflectance spectroscopy is used to overcome the limitations of conventional methods of soil analysis. The objective was to develop a regional prediction model of soil organic carbon content based on laboratory measurements of reflectance within the visible and near-infrared spectral ranges. To achieve this, principal component analysis was used in order to determine the chemical and physical variability of 64 soil samples collected from different sites in Brittany (France). This analysis allowed samples to be divided into both calibration and validation data sets with quite similar analytical properties. A partial least squares regression algorithm was then applied to model and predict the soil organic carbon content on the basis of its spectral reflectance within the visible and near-infrared domain (400–950 nm). Results revealed a high level of agreement between measured and predicted values with coefficients of determination, root mean-squared errors and relative prediction deviations of 0.91, 0.36% and 3.4 in cross-validation and of 0.83, 0.46% and 2.35 in prediction. The model proved to be valid over the range 0.90–5.20% of organic carbon content. Good predictions of the soil organic carbon content are therefore still possible by simply using a cheap spectrometer operating between 400 and 950 nm using a regional soil database which can be progressively enhanced.

**Stevens, A., van Wesemael, B., Vandenschrick, G., Touré, S., Tychon, B., 2006. Detection of Carbon Stock Change in Agricultural Soils Using Spectroscopic Techniques. Soil Science Society of America Journal, Vol. 70, May-June 2006**

Soil organic carbon (SOC) represents one of the major pools in the global C cycle. Therefore, even small changes in SOC stocks cause important $CO_2$ fluxes between terrestrial ecosystems and the atmosphere. However, SOC stocks are difficult to quantify accurately due to their high spatial variability. The aim of this paper is to evaluate the potential of Imaging Spectroscopy (IS) using the Compact Airborne Spectrographic Imager (CASI; 405–950 nm) and field spectroscopy with an Analytical Spectral Devices spectrometer (ASD; 350–2500 nm) to measure SOC content in heterogeneous agricultural soils. We used both stepwise and partial least square (PLS) regression analysis to relate spectral measurements to SOC contents. Standard Error of Prediction (SEP) for the ASD ranged from 2.4 to 3.3 g C $kg^{-1}$ depending on soil moisture content of the surface layer. Imaging spectroscopy performed poorly, mainly due to the narrow spectral range of the CASI. Tests using both the CASI and the Shortwave infrared Airborne Spectrographic Imager (SASI; 900–2500 nm) showed better results. The variation in soil texture and soil moisture content degrades the spectral response to SOC contents. Currently, SEP allows to detect a SOC stock change of 7.2–9.9 Mg C $ha^{-1}$ in the upper 30 cm of the soil, and is therefore still somewhat high in comparison with changes in SOC stocks as a result of management or land conversion (0.3–1.9 Mg C $ha^{-1}$ $yr^{-1}$ ). A detailed SOC maps produced by IS reflected the patterns in SOC contents due to the recent conversion from grassland to cropland.

**Viscarra Rossel, R.A., Walvoort, D.J.J., McBratney, A.B., Janik, L.J., Skjemstad, J.O., 2006. Visible, near infrared, mid infrared or combined diffuse reflectance spectroscopy for simultaneous assessment of various soil properties. Geoderma 131 (2006) 59–75**

Historically, our understanding of the soil and assessment of its quality and function has been gained through routine soil chemical and physical laboratory analysis. There is a global thrust towards the development of more time- and cost- efficient methodologies for soil analysis as there is a great demand for larger amounts of good quality, inexpensive soil data to be used in environmental monitoring, modelling and precision agriculture. Diffuse reflectance spectroscopy provides a good alternative that may be used to enhance or replace conventional methods of soil analysis, as it overcomes some of their limitations. Spectroscopy is rapid, timely, less expensive, non-destructive,

straightforward and sometimes more accurate than conventional analysis. Furthermore, a single spectrum allows for simultaneous characterisation of various soil properties and the techniques are adaptable for on-the-go field use. The aims of this paper are threefold: (i) determine the value of qualitative analysis in the visible (VIS) (400–700 nm), near infrared (NIR) (700–2500 nm) and mid infrared (MIR) (2500–25000 nm); (ii) compare the simultaneous predictions of a number of different soil properties in each of these regions and the combined VIS–NIR–MIR to determine whether the combined information produces better predictions of soil properties than each of the individual regions; and (iii) deduce which of these regions may be best suited for simultaneous analysis of various soil properties. In this instance we implemented partial least-squares regression (PLSR) to construct calibration models, which were independently validated for the prediction of various soil properties from the soil spectra. The soil properties examined were soil $pH_{Ca}$ , $pH_{w}$ , lime requirement (LR), organic carbon (OC), clay, silt, sand, cation exchange capacity (CEC), exchangeable calcium (Ca), exchangeable aluminium (Al), nitrate–nitrogen ($NO_3$ –N), available phosphorus ($P_{Col}$ ), exchangeable potassium (K) and electrical conductivity (EC). Our results demonstrated the value of qualitative soil interpretations using the loading weight vectors from the PLSR decomposition. The MIR was more suitable than the VIS or NIR for this type of analysis due to the higher incidence spectral bands in this region as well as the higher intensity and specificity of the signal. Quantitatively, the accuracy of PLSR predictions in each of the VIS, NIR, MIR and VIS–NIR–MIR spectral regions varied considerably amongst properties. However, more accurate predictions were obtained using the MIR for pH, LR, OC, CEC, clay, silt and sand contents, P and EC. The NIR produced more accurate predictions for exchangeable Al and K than any of the ranges. There were only minor improvements in predictions of clay, silt and sand content using the combined VIS–NIR–MIR range. This work demonstrates the potential of diffuse reflectance spectroscopy using the VIS, NIR and MIR for more efficient soil analysis and the acquisition of soil information.

# *Annex II*

## Remote sensing methods for discriminating conservation agriculture tillage from conventional tillage

This part of the research was only started but not completed. A thorough bibliographic research on previous studies on this matter was carried out that shows how segregation of conservation agriculture from conventional farming is generally possible though remote sensing. Results of the studies found are presented hereafter as a series of (publicly available) abstracts.

**Hache, C., Shibusawa, S. , Sasao, A., 2005. Discriminating conventional and conservation agricultural management practices with airborne multispectral imagery. Agriculture, Ecosystems & Environment. Volume 111, Issues 1-4, 1 December 2005, Pages 354-366**

In its collaborative efforts towards environmental preservation, the agricultural sector faces the challenge of adopting management practices that reduce carbon emission and increase its sequestration. Remote sensing offers the means to discriminate the spectral signatures of conventional and conservation practices and develop monitoring methods so needed by policy makers. This research provides valuable insight into the applicability of wheat canopy multispectral airborne images to discriminate conventional and conservation tillage practices interacting with two nutrient sources (i.e., inorganic and a mixture of inorganic–organic fertilizer). Combinations of tillage and nutrient sources were considered as treatments in this research. Multispectral images were acquired at different growth stages. Three simple analysis methods (analysis of variance, supervised image classification and its contingency analysis, and unsupervised classification) yielded similar results. Analysis of variance indicated high capability of the red band to discriminate tillage practices, the green band to differentiate nutrient sources and the near infrared to separate treatments. Tillage practices were discriminated with high accuracy throughout the growing season using both supervised (70–82% accuracy) and unsupervised classification methods. Nutrient source classification accuracy was also high (77–89%), but imagery should be collected from partially vegetated fields (i.e., before flowering). For treatment discrimination using either supervised or unsupervised methods, images should be acquired before flowering. Multispectral images collected early in the season demonstrated a high potential to discriminate conventional and conservation practices.

**Yang, C.-C., Prasher, S.O., Enright, P., Madramootoo, C., Burgess, M., Goel, P.K., Callum, I., 2003. Application of decision tree technology for image classification using remote sensing data. Agricultural Systems 76 (2003) 1101–1117**

Hyperspectral images of plots, cropped with silage or grain corn and cultivated with conventional tillage, reduced tillage, or no till, were classified using the classification and regression tree (C&RT) approach, an innovative intelligent computational algorithm in data mining. Each tillage/cropping combination was replicated three times, for a total of 18 plots. Five hyperspectral reflectance measurements per plot were taken randomly to obtain a total of 90 measurements. Images were taken on June 30, August 5, and August 25, 2000 to reflect three stages of crop development. Each measurement consisted of reflectances in 71 wave bands ranging from 400 to 950 nm. C&RT models were developed separately for the three observation dates, using the 71 reflectances as inputs to classify the image according to: (a) tillage practice, (b) residue level, (c) cropping practices, (d) tillage/cropping (residue) combination. C&RT models could generally distinguish tillage practices with a classification accuracy of 0.89 and residue levels with a classification accuracy of 0.98.

**Hadria, R., Duchemin, B., Baup, F., Le Toan, T., Bouvet, A., Dedieu, G., Le Page, M., 2009. Combined use of optical and radar satellite data for the detection of tillage and irrigation operations: Case study in Central Morocco. Agricultural Water Management 96 (2009) 1120–1127**

The objective of this study is to present a new application of optical and radar remote sensing with high spatial (#10 m) and temporal (a few days) resolutions for the detection of tillage and irrigation operations. The analysis was performed for irrigated wheat crops in the semi-arid Tensift/Marrakech plain (Central Morocco) using three FORMOSAT-2 images and two ASAR images acquired within one week at the beginning of the 2005/2006 agricultural season. The approach we developed uses simple mapping algorithms (band thresholding and decision tree) for the characterisation of soil surface states. The first images acquired by FORMOSAT and ASAR were processed to classify fields into three main categories: ploughed (in depth), prepared to be sown (harrowed), and not ploughed-not harrowed. This information was combined with a change detection analysis based on multitemporal images to identify harrowing and irrigation operations which occurred between two satellite observations. The performance of the algorithm was evaluated using data related to land use and agricultural practices collected on 124 fields. The analysis shows that drastic changes of surface states caused by ploughing or irrigation are detected without ambiguity (consistency index of 96%). This study provided evidence that optical and radar data contain complementary information for the detection of agricultural operations at the beginning of agricultural season. This information could be useful in regional decision support systems to refine crop calendars and to improve prediction of crop water needs over large areas.

**Haché, C., Shibusawa, S., Sasao, A., Suhama, T., Sah, B.P., 2007. Field-derived spectral characteristics to classify conventional and conservation agricultural practices. Computers and Electronics in Agriculture 57 (2007) 47–61**

Field-derived hyperspectral reflectance of soil and wheat were collected during a wheat-growing season (February, March and April) using a portable spectrophotometer in an experimental field receiving conventional and conservation agricultural practices. These practices included two types of tillage, conventional and conservation, and two types of nutrient sources, inorganic and a combination of inorganic–organic fertilizers. This research aims at discriminating conventional and conservation practices and identifying the most applicable bands for discrimination. Spectral characteristics of soil and wheat indicated that soil spectra were useful to discriminate tillage practices, while wheat spectra were useful to discriminate nutrient sources. Cluster and principal component analysis (PCA) revealed that the best time to collect soil and wheat spectra for tillage and nutrient sources differentiation was at the beginning of the season. According to the best time for spectra collection, wavelengths more suitable for discriminating tillage practices were in the VIS and NIR ranges, and in the NIR range for nutrient sources. Furthermore, spectra and band-wise normalization were applied indistinctly to the data sets. It was understood that soil or wheat spectra could not be independently used to discriminate treatments (interactions between tillage and nutrient sources), unless the spectra are normalized and a method such as PCA used.

**Watts, J.D., Lawrence, R.L., Miller, P.R., Montagne, C., 2009. Monitoring of cropland practices for carbon sequestration purposes in north central Montana by Landsat remote sensing. Remote Sensing of Environment 113 (2009) 1843–1852**

We used an object-oriented approach in conjunction with the Random Forest algorithm to classify agricultural practices, including tillage (till or no-till (NT)), crop intensity, and grassland-based conservation reserve (CR). The object-oriented approach allowed for per-field classifications and the incorporation of contextual elements in addition to spectral features. Random Forest is a classification

tree-based advanced classifier that avoids data over-fitting associated with many tree-based models and incorporates an unbiased internal classification accuracy assessment. Landsat satellite imagery was chosen for its continuous coverage,cost effectiveness, and image accessibility. Classification results for 2007 included producer's accuracies of91% for NT and 31% for tillage when applying Random Forest to image objects generated from a May Landsat image. Low classification accuracies likely were attributed to the misclassification of conservation-based tillage practices as NT. Results showed that the binary separation of tillage from NT management is likely not appropriate due to surface spectral and textural similarities between NT and conservation-type tillage practices. Crop and CR lands resulted in producer's accuracies of 100% and 90%, respectively. Crop and fallow producer's accuracies were 95% and 82% in the 2007 classification, despite post-senesced vegetation; misclassification within the fallow class was attributed to pixel-mixing problems in areas of narrow (<100 m) strip management. A between-date normalized difference vegetation index approach was successfully used to detect areas having "changed" in vegetation status between the 2007 and prior image dates; classified "changed" objects were then merged with "unchanged" objects to produce crop status maps. Field crop intensity was then determined from the multi-year analysis of generated crop status maps.

**South, S., Qi, J., Lusch, D.P., 2004. Optimal classification methods for mapping agricultural tillage practices. Remote Sensing of Environment 91 (2004) 90–97**

The classification of agricultural tillage systems has proven challenging in the past using traditional classification methods due to the similarity of spectral reflectance signatures of soils and senescent crop residues. In this study, five classification methods were examined to determine the most suitable classification algorithm for the identification of no-till (NT) and traditional tillage (TT) cropping methods: minimum distance (MD), Mahalanobis distance, Maximum Likelihood (ML), spectral angle mapping (SAM), and the cosine of the angle concept (CAC). A Landsat ETM+ image acquired over southern Michigan and northern Indiana was used to test these classification methods. Each classification method was validated with 293 ground truth sampling locations collected commensurate with the satellite overpass. Classification accuracy was then assessed using error matrix analysis, Kappa statistics, and tests for statistical significance. The results indicate that of the classification routines examined, the two spectral angle methods were superior to the others. The cosine of the angle concept algorithm outperformed all the other classification routines for tillage practice identification and mapping, yielding an overall accuracy of 97.2% (Kappa = 0.959).

**Bricklemyer, R.S., Lawrence, R.L., Miller, P.R., Battogtokh, N., 2006. Predicting tillage practices and agricultural soil disturbancein north central Montana with Landsat imagery. Agriculture, Ecosystems and Environment 114 (2006) 210–216**

Management of agricultural soils, most notably tillage, influences wind, and water erosion, which in turn has implications for non-point source pollution of pesticides, fertilizer, and sediment in agro-ecosystems. No-till (NT) practices improve soil, water, and aquatic ecosystem quality by reducing soil erosion and chemical runoff. The ability of cropland soils to sequester C from the atmosphere might help mitigate global warming. Classification of Landsat ETM+ satellite images has the potential to identify tillage practices and soil disturbance over large areas, enabling efficient monitoring of these agricultural practices. Previous studies predicting tillage management had relatively small study areas (located in a single county), relatively low numbers of fields (6–51), and were temporally focused on non-planted fields to reduce the potential effects of crop canopy interference and/or field patterning. Our objectives were to predict in the presence of crop canopy and over a spatially large, management diverse study area (1) tillage systems (NT versus tilled) and (2) soil disturbance. A farm survey of the study area, north central Montana, was used to as a means to obtain extensive field-level farm management data. We compared logistic regression (LR), traditional classification tree analysis (CTA), and boosted classification tree analysis (BCTA) for identifying NT fields. Logistic regression had an

overall accuracy of 94%, BCTA 89%, and CTA 87%, but tillage was not well distinguished. Soil disturbance was estimated using linear regression (LM), regression tree analysis (RTA), and stochastic gradient boosting (SGB), an RTA variant. Classification of soil disturbance was best achieved using RTA (predicted mean soil disturbance not significantly different than known soil disturbance, p-value = 0.08). Classification of Landsat ETM+ imagery showed promise for predicting tillage and agricultural soil disturbance over large, heterogeneous areas.

# *Annex III*

### GNU Octave code for destriping Hyperion scenes

```
# This is a GNU Octave script to destripe Hyperion imagery with radiometric corrections applied
# only. The mathematical method follows Sun L., Neville R., Staenz K., White, H.P., 2008.
# “Automatic destriping of Hyperion imagery based on spectral moment
# matching.” Canadian Journal of Remote Sensing, vol.34, Suppl.1, pp.S68-S81, 2008
# GNU Octave coding Paolo Prosperi, May 18 – Sept 16 2011, as part of my Ph.D. thesis.
# This script requires the tiffread.m module (not embedded within Octave, can be taken from
# http://www.embl.de/~nedelec/misc/index.html) to overcome some limitations of the standard
# imread command that rescales any image to "byte" type (i.e. 8bits = values range 0-255).
# This script also requires the imwrite2tif.m module (not embedded within Octave, can be
# downloaded from mathworks) to overcome the limits in data type supported by the
# standard imwrite command (unit16 only).

# All additional modules need to be copied into the /usr/share/octave/packages/3.0/image-1.0.8/
# directory in order to be usable.

# This script requires additionally the armars.m script to be present in the same directory.
# Non executable comments begin with an ash symbol (#).

# Coded with GEDIT and Octave 3.0.5 running within a Portable Ubuntu Tres (Ubuntu 9.10
# Karmic Koala) on a Windows Vista Home based HP Pavillon dv6000 notebook.

# To run this script, first split Hyperion .L1R file into 242 GeoTiff band files.
# Open an empty file with GEDIT, then copy and paste the
# text hereafter and save the file with a name (for example: destriping.m). GEDIT recognizes it is a
# GNU Octave code and will highlight the commands.
# (Remember to modify the path and imagename to be processed (first lines of code, herebelow)).
# Then do the same with the armars.m code hereafter and place in the same directory as the
# previous script.
# In Octave, type: cd your-directory-of-m-files and press enter.
# Then type in destriping.m (if you called the file like this) and press enter.
# Give response to the parameters required.
# The script can be quite slow and on a normal notebook, it takes a few hours to destripe a single
# scene. It can be interrupted with CTRL+C.
# If re-run with the same parameters will resume processing of the remaining bands.
```

# This code is licensed as 


(Creative Commons Attribution-NonCommercial-ShareAlike 3.0 Unported License).

```
# Please, acknowledge source as: Paolo Prosperi, 2011. GNU OCTAVE code for destriping
# Hyperion scenes based on spectral moment matching  Written in partial fulfilment of a Ph.D.
# thesis in Agricultural ecology on “Evaluation of a remote sensing based method for the
# assessment of agricultural crop residues on the soil surface”. State University of Milan.

# For any questions: paolo-prosperi@tiscali.it Mind, though, I'm not a programmer!
```

```
clear

dirr=input('Enter the path to the directory containing the scene to be processed (witihin “” and \
ending with /): ');
hyp=input('Enter the scene file name to be processed (witihin “”): ');


str = dir([dirr,"/*.tif"]); # Creates a structure array containing the list of all the band filenames.
nub = size(str)(1); # Retrieves the number of bands.

cd(dirr) # Changes the working directory.

img1=imread([dirr,str(1).name]) ; # Reads the first band-image, just to retrieve the dimensions
                                  # (number of rows and columns in the next two lines).
rows=size(img1)(1)-1 ;  # Calculates the number of rows in the image.
cols=size(img1)(2) ;  # Calculates the number of columns in the image.

 co=exist([hyp,'_arm.mat'],"file");
 switch co  # Checks whether the matrices of means and std have already been created
            # (in a previous run of the script).
  case 0
  cd /home/pubuntu/GDL/Scripts
  armars  # If not, it runs the armars.m script (in a separate file).
  cd(dirr)
 otherwise
  arm=load([dirr,hyp,'_arm.mat']).arm;
  ars=load([dirr,hyp,'_ars.mat']).ars;
  blist=load([dirr,hyp,'_blist.mat']).blist;
 endswitch

        N=input('Enter N, the average width of the Hyperion stripes (as number of pixels): ');
        M=input('Enter M, the length of the row segments (3 to 6 times N): ');
        P=input('Enter P, the maximum number of highly correlated bands: ');
        H=input('Enter the max. no. of columns of the most similar bands (0=all, 1=j-ieth): ');

        ind=[1];  # Creates a simpe band-index ordered vector for use in Steps 3 and 4.
         for no=2:nub
          ind=[ind;no];
         endfor


         # STEP 2.  Calculates the medians of means/stdevs.

        amm=zeros(nub,cols) ;
        # Creates an empty array (a matrix) to contain the medians of the above means,
        # calculated hereafter
        # (dimensions: rows= same as any Hyperion image, columns=number of bands).
        # 'amm'=array of medians of means (see article).
```

```
# MATRIX OF MEDIANS OF MEANS.

ams=zeros(nub,cols) ;
# Creates an empty array (a matrix) to contain the medians of the standard deviations,
# calculated hereafter
# (dimensions: rows= same as any Hyperion image, columns=number of bands). '
# ams'=array of median of standard deviations (see article).
# MATRIX OF MEDIANS OF STANDARD DEVIATIONS.

len=2*N+1 ; # The median window's size.

# The following loops go through the matrix of means to calculate the row medians of
# both the matrix of  means and the matrix of standard deviations.
# Each pixel will be assigned its own value based on the median (moving) window.
for ir=1:nub  # The beginning of the loop through the bands. 'ir' = index of rows.
 for ic=1:cols # The beginning of the loop through the columns. 'ic' = index of columns.

# The following series of 'if's check the position of the pixel compared to the border
# and the window's size.

  # Case 1: the pixel's column is lower than N. All pizels from column zero to 2N+1
  # are taken for the median.
  if ic <= N+1
    wbeg=1 ;
    wend=ic+N ;

  # Case 2: the difference between the number of columns and the pixel's column is
  # lower than N.  The last 2N+1 column pixels are taken.
  elseif ic >= (cols-N)
    wbeg=ic-N+1 ;   # The '+1' in this assignment prevents the window's size to be len+1.
    wend=cols ;

  # Case 3: all the remaining pixels. With respect to any given pixel, N pixels before
  # and N after are taken for the median.
  else
    wbeg=ic-N ;
    wend=ic+N ;
  endif
    amm(ir,ic)=median(arm(ir,wbeg:wend))  ; # 'amm'= array of medians of means.
    ams(ir,ic)=median(ars(ir,wbeg:wend))  ; # 'ams'= array of medians of standard deviations.

 endfor
endfor # Now the two new matrices of medians are filled in.


 # STEP 3. ========================== Calculates the rescaling factors.

tot=2*M+1 ; # The real length of the target row.

##### OVERALL LOOP1 #####
```

```
 # The following loops go through the matrix of medians (means & stdevs) to
 # calculate the gain- and offset- rescaling factors.
 # Each pixel will be assigned its own value based on the mean moving window.

for i=1:nub

# LOOP1. Calculation of the destriping factors for each band of a single Hyperion scene.
# Loops through the rows (i.e. the bands) of the Hyperion image cube.
# From now on, 'i' is the band to be destriped.

# Array of the Euclidean distances between target and test row segments for means
# (see article). "adm"=Array of distances for means.
adm=zeros(nubo,2) ;
ads=zeros(nubo,2) ;  # And for stdves.

awin=zeros(2,cols) ; # This matrix is to contain the M windows' beginning and
# end columns for each column in the mean or stdevs matrices.
# The value for 'beginning' (wbegf) is on row 1, for 'end' (wendf) is on row 2.

asmul=zeros(nub,cols) ; # Creates empty arrays to store the rescaling factor for
                          # means (smulj) calculated below.
assil=zeros(nub,cols) ; # Creates empty arrays to store the rescaling factor for
                         # stdevs (ssilj) calculated below.

armm=zeros(nub,cols) ; # Array of rescaled medians of means.
arms=zeros(nub,cols) ; # Array of rescaled medians of stdevs.

destriped=int16(zeros(cols,rows)) ; # Creates an empty array for storing the destriped image.
# Rows and cols are swapped to overcome a problem of Octave when writing hdf5 images.

b=ind(ind != i); # Creates a vector of l=i-1 bands to be processed
                  # (i.e. all excluding the one to destripe).

iz=blist(i); # Retrieves the image-band being destriped.
              # Only 'blist' contains the real band numbers.
disp(['Processing band no. ', num2str(iz)]) # Displays the band being processed.
fflush(stdout);

imname=[hyp,'_b',num2str(iz),'_destriped.h5'];



if (exist([hyp,'_b',num2str(iz),'_destriped.h5'],"file") == 0)
# Checks whether the destriped image has already been created (in a previous run).

 for j=1:cols # LOOP2. The beginning of the loop through the columns.
  # The following series of 'if's' checks the position of the pixel compared to
  # the window's size.

  # Case 1: the pixel's column is lower than M.
```

```
 # All pixels from column one to 2M+1 are taken for the calculation.
 if j <= M+1
   wbegf=1 ; # The starting column of the window.
    # "wbegf"= window beginning (point for rescaling) factor.
   wendf=j+M; # The closing column of the window.

 # Case 2: the difference between the number of columns and
 # the pixel's column is lower than M. The last 2M+1 column pixels are taken.
 elseif j >= (cols-M+1)
   wbegf=j-M+1 ;
   wendf=cols ;

 # Case 3: all the remaining pixels. With respect to any given pixel,
 # M pixels before and M after are taken for the calculation.
 else
   wbegf=j-M ;
   wendf=j+M ;
 endif

 awin(1,j)=wbegf;
 awin(2,j)=wendf;

 mmuij=mean(amm(i,wbegf:wendf)) ;
# 'mmuij'=mean mu of element i, j of the amm matrix (= medians of means).
 msiij=mean(ams(i,wbegf:wendf)) ;
# 'msiij'=mean sigma of element i, j of the ams matrix (= medians of stdevs).

 nubo=nub-1;
 for ix=1:nubo
# beginning LOOP3. Calculation of the rescaling factors for all bands except the one to
# destripe (i.e. nubo bands).
   l = b(ix) ;

    mmulj=mean(amm(l,wbegf:wendf)) ;
# 'mmulj'= mean mu of element l, j of the amm matrix (= medians of means). See article.
    msilj=mean(ams(l,wbegf:wendf)) ;
# 'msilj'= mean sigma of element l, j of the ams matrix (= medians of stdevs). See article.

   if mmulj != 0 && msilj != 0 # Avoids dividing by zero.
    smulj=mmuij/mmulj ;
# 'smulj'= scaling factor (s) for pixel l,j of the matrix of medians of means (mu).
    ssilj=msiij/msilj ;
# 'ssilj'= scaling factor (s) for pixel l,j of the matrix of medians of standard deviations
# (sigma).
   else
    smulj=0 ;
    ssilj=0 ;
   endif

   asmul(l,j)=smulj ; # Stores the smulj factor in the appropriate matrix for use in Step 5.
```

```
   assil(l,j)=ssilj ; # Stores the ssilj factor in the appropriate matrix for use in Step 5.

  endfor
# end LOOP3. Rescaling factors are now calculated for all rows 'l' (other than row 'i') and
# for column 'j'.
 endfor # end LOOP2. Rescaling factors are now calculated also for all columns.

 asmul(i,:)=1 ;
# Stores the smulj factor for pixels on row i in the appropriate matrix for use in Step 5.
 assil(i,:)=1 ;
# Stores the ssilj factor for pixels on row i in the appropriate matrix for use in Step 5.


 # STEP 4. ====Identifies the P bands most similar to the one to be destriped.

 armm=amm .* asmul  ; # Rescales the amm matrix (excluding row i) with the smulj factor.
 arms=ams .* assil  ; # Rescales the ams matrix (excluding row i) with the ssilj factor.

 for j=1:cols ##############
# beginning LOOP4 through all the columns.
# Calcultaes the Eu. distances. It'll last 'til the end.
  for ix=1:nubo # beginning LOOP5 through all the bands (excluding band i).
    l = b(ix) ;
   # Extraction of the 'Euclidean distances' (see article) for the test segments corresponding
   # to target segment centered on pixel 'i,j'.
   # i.e. Euclidean distance = square root of the sum of the quadratic difference
   # of test segment pixels with target segment pixels.

   adm(ix,1)=l;
# The array of distances for means. Column 1 contains the actual band being processed.
   ads(ix,1)=l;
   adm(ix,2)=sqrt(sumsq(armm(i,awin(1,j):awin(2,j)) .- armm(l,awin(1,j):awin(2,j)))) ;
# Column 2 contains the Euclidean distance.
   ads(ix,2)=sqrt(sumsq(arms(i,awin(1,j):awin(2,j)) .- arms(l,awin(1,j):awin(2,j)))) ;

  endfor  # Ends LOOP5. Euclidean distance is now calculated for all the "l" test
          # row segments corresponding to the j-ieth column.

   [orderedm,adms]=sort(adm(:,2)) ;  # Sorts all the test row segments in increasing order
                                     # based on the Eu. distance from the target row (i).
   [ordereds,adss]=sort(ads(:,2)) ; # adms/adss contain the sorted position (in the original list)
                                    # of the rescaled bands based on the Eu. distance.
                                    # 'adms' = adm sorted.
    if H == 0 # Considers all the columns in the selected, most-similar bands.

 # STEP 5. ============== Creates the C' matrices (most similar band subsets).
   tos=awin(2,j)-awin(1,j)+1;

   selm=zeros(P,tos) ; # Creates an array to contain the selected band pixels from
                       # the means matrix (see article).
```

```
                    # 'selm' = selected bands for means.
  sels=zeros(P,tos) ; # Creates an array to contain the selected band pixels from
                      # the stdev matrix (see article).
                      # 'sels' = selected bands for stdevs.


  for ip=1:P # beginning LOOP6. Retrieves and rescales the 'nearest' P bands.
   brm=adm(adms(ip),1) ; # Finds the position of the 'nearest' P bands values inside adm
   brs=ads(adss(ip),1) ; # and inside ads.

   # Rescales the original means corresponding to the selected P bands.
   selm(ip,1:tos)=arm(brm,awin(1,j):awin(2,j)) .* asmul(brm,awin(1,j):awin(2,j)) ;

   # Rescales the original stdevs corresponding to the selected P bands.
   sels(ip,1:tos)=ars(brs,awin(1,j):awin(2,j)) .* assil(brs,awin(1,j):awin(2,j)) ;
  endfor # end LOOP6. Now all the C' j pixels (for pixel i,j) are rescaled.

# STEP 6. ======================== The C^ matrices are created.
  # This calculates the means and stdevs of the columns of the selected bands (left-right).
   mselm=zeros(1,tos);
   sselm=zeros(1,tos);
   msels=zeros(1,tos);
   ssels=zeros(1,tos);
   for zx=1:tos
   mselm(1,zx)=mean(selm(:,zx))   ; # The mean of the selm array columns.
   sselm(1,zx)=std(selm(:,zx))    ; # The stdev of the selm array columns.

   msels(1,zx)=mean(sels(:,zx))   ; # The mean of the sels array columns.
   ssels(1,zx)=std(sels(:,zx))    ; # The stdev of the sels array columns.
   endfor

   for ip=1:P # beginning LOOP7. This substitutes the means or stdevs of the rows
              # of the selected bands (top-bottom), if needed.
    for zx=1:tos
    if selm(ip,zx) > mselm(1,zx)+2*sselm(1,zx)  || selm(ip,zx) < mselm(1,zx)-2*sselm(1,zx)
    # The case of the original element being more than two stdvs away from
    # the initial mean (matrix of means).
        selm(ip,zx)=mselm(1,zx) ;
    endif

    if sels(ip,zx) > msels(1,zx)+2*ssels(1,zx) || sels(ip,zx) < msels(1,zx)-2*ssels(1,zx)
    # The case of the original element being more than two stdevs away from
    # the initial mean (matrix of stdvs).
        sels(ip,zx)=msels(1,zx) ;
    endif
   endfor
  endfor # end LOOP7. Now all the elements of the C^ matrices (for pixel i,j) are there.


   mij=mean(mean(selm)) ; # The mean of the selm pixels' (column) means = the
```

```
                                # expected value for pixel i,j in the matrix of means.
sij=mean(mean(sels)) ; # The mean of the sels pixels' means = the
                               #expected value for pixel i,j in the matrix of std.

else # The H loop. Considers only the j-ieth columns in the selected, most-similar bands.

     # STEP 5bis. ============ Creates the C' matrices (most similar band subsets).

       selm=zeros(P,1) ;
       sels=zeros(P,1) ;

       for ip=1:P # beginning LOOP6. Retrieves and rescales the 'nearest' P bands.
        brm=adm(adms(ip),1) ;
             # Finds the position of the 'nearest' P bands values inside adm

        brs=ads(adss(ip),1) ; # and inside ads.

        # Rescales the original means corresponding to the selected P bands.
        selm(ip,1)=arm(brm,j) * asmul(brm,j) ;

        # Rescales the original stdevs corresponding to the selected P bands.
        sels(ip,1)=ars(brs,j) * assil(brs,j) ;
       endfor # end LOOP6. Now all the C' j pixels (for pixel i,j) are rescaled.

     # STEP 6bis. =============== The C^ matrices are created.
     # This calculates the means and stdevs of the columns of the
     # selected bands (left-right).

          mselm=mean(selm(:,1))   ; # The mean of the selm array columns.
          sselm=std(selm(:,1))    ; # The stdev of the selm array columns.

          msels=mean(sels(:,1))   ; # The mean of the sels array columns.
          ssels=std(sels(:,1))    ; # The stdev of the sels array columns.

          for is=1:P # beginning LOOP7. This substitutes the means or stdevs
                           #  of the rows of the selected bands (top-bottom), if needed.
           if selm(is,1) > mselm+2*sselm  || selm(is,1) < mselm-2*sselm
            # The case of the original element being more than two stdvs away
          #  from the initial mean (matrix of means).
            selm(is,1)=mselm ;
           endif

           if sels(is,1) > msels+2*ssels || sels(is,1) < msels-2*ssels
            # The case of the original element being more than two stdevs
                  # away from the initial mean (matrix of stdvs).
            sels(is,1)=msels ;
           endif
          endfor # end LOOP7. Now all the elements of the C^ matrices
                  # (for pixel i,j) are there.
```

```
                mij=mean(selm(:,1)) ;  # The average (mean) of the selm pixels = the
                                       # expected value for pixel i,j in the matrix of means.
                sij=mean(sels(:,1)) ; # The average (mean) of the sels pixels = the
                                       #expected value for pixel i,j in the matrix of std.

   endif # Ends the H case.


# STEP 7. ========================== Calculates gains and offsets
   if ars(i,j) == 0
    gij = 1 ; # Avoids script blockage in case the image is completely
                # black (i.e. all pixels=0).
   else
    gij=sij/ars(i,j) ; # The gain for element i,j in the matrix of along-track columns/bands.
   endif

   oij=mij - gij*arm(i,j) ; # The offset for element i,j in the matrix
                                 # of along-track columns/bands.


        disp(["arm(",num2str(iz),",",num2str(j),")= ",num2str(arm(i,j))])
        disp(["expected= ",num2str(mij)])
        disp(["gain= ",num2str(gij)])

        disp(["ars(",num2str(iz),",",num2str(j),")= ",num2str(ars(i,j))])
        disp(["expected= ",num2str(sij)])
        disp(["offset= ",num2str(oij),"\n"])
        fflush(stdout);


# STEP 8. ========================== Destripes band-image 'i'.
# Transforms the original along-track pixels in the new ones.
name2=str(i).name;
imgorig=tiffread(name2).data;

if iz >= 70 # This bit of code corrects the 1 pixel shift in SWNIR bands.
 erows=rows+1;
 imgcor=zeros(rows,cols);
 imgcor(:,1:128)=imgorig(1:rows,1:128);
 imgcor(:,129:cols)=imgorig(2:erows,129:cols);
else
 imgcor=imgorig(1:rows,:);
endif

 if j == 1
  x1=3;
  x2=2;
 elseif j == cols
  x1=j-1;
  x2=j-2;
```

```
        else
         x1=j+1;
         x2=j-1;
        endif

        if arm(i,j) == 0
         destriped(j,:)=0.5*(imgcor(:,x1)+imgcor(:,x2));
       # This would avoid a black column in case the original is black.
        else
         destriped(j,:)=imgcor(:,j)*gij + oij;
        endif

 endfor #end LOOP4. Now all the gains and offsets are there and a whole
       # image-band has been destriped.


      imname=[hyp,'_b',num2str(iz),'_destriped.h5'];
      save("-hdf5",imname,"destriped")

  endif # Ends the loop run when band was not already destriped.
endfor # end LOOP1. Now all the bands of a single Hyperion scene have been destriped.
```

---

# The following is the code that has to be copied and pasted in the armars.m file. The file has to
# reside in the same directory as the preceding one.

```
# armars.m script
#Creates the mean and std matrices for an input array of Hyperion bands.

arm=zeros(numb,cols) ; # Creates an empty array (a matrix) to contain the means calculated
                       # hereafter (dimensions: rows=number of bands,
                       # columns=same as any Hyperion image). 'arm'=array of means (see
                       # article). MATRIX OF MEANS.
ars=zeros(numb,cols) ; # Creates an empty array (a matrix) to contain the standard deviations
                      # calculated hereafter (dimensions: rows=number of bands,
```

```
                    # image, columns=same as any Hyperion image). 'ars'=array of standard
                    # deviations (see article). MATRIX OF STANDARD DEVIATIONS.

clear img1 ; # Resets the first image to avoid reading it twice (would cause error).
cd(dirr)  # Changes the working directory.

 # ======STEP 1: calculates means and stdevs of each band-image column (along-track) pixels.
blist=[]; # Initiates the list of bands to be processed.

for bl=1:numb  # The beginning of the loop through all the bands of a single Hyperion scene.
               # 'bl'= bands loop.
 name=str(bl).name; # Determines the band corresponding to the current loop index-number.
 s=size(name)(2) ; # Extracts the correct band number from image filenames (bands in 'str' are not
                   # listed in numerical order).
 if s==29
  imgb=substr(name,25,1);
 elseif s==30
  imgb=substr(name,25,2);
 else
  imgb=substr(name,25,3);
 endif
disp(['Reading band image ', imgb]);
fflush(stdout);

 imgused=tiffread(name).data ; # Reads the image and stores it into memory (as a structure). Then,
                               # it extracts the actual image as an array.
 if imgb >= 70 # This bit of code corrects the 1 pixel shift in SWNIR bands.
  erows=rows+1;
  imgcor=zeros(rows,cols);
  imgcor(:,1:128)=imgused(1:rows,1:128);
  imgcor(:,129:cols)=imgused(2:erows,129:cols);
 else
  imgcor=imgused(1:rows,:);
 endif

warning('tiffread is not perfect but will continue execution')
 blist=[blist;str2num(imgb)]; # Finalizes the list of bands to be processed.

 for ic=1:cols  # The beginning of the loop through each band-image. 'ic'= index column.
  arm(bl,ic)=mean(imgcor(:,ic)); # The mean of each image-column (i.e. the mean of the along-track
                                 # vector of pixels) stored in the arm array.
  ars(bl,ic)=std(imgcor(:,ic));  # The standard deviation of each image-column (i.e. the stdev of the
                                 # along-track vector of pixels) stored in the ars array.
 endfor
endfor # Now the matrix of means and the matrix of stdevs are there.

save([hyp,'_arm.mat'],'arm'); # Saves the arm/ars/blist matrices for use in the main script.
save([hyp,'_ars.mat'],'ars');
save([hyp,'_blist.mat'],'blist');
return
```

# References


**Aktaruzzaman, 2008**. Aktaruzzaman, M. Simulation and Correction of Spectral Smile Effect and its Influence on Hyperspectral Mapping. Available at: http://www.gem-msc.org/Academic%20Output/Academic%20Output%202006/Thesis_Md_Aktaruzzaman.pdf Accessed October 2011.

**Anderson and Magleby, 1997**. Anderson, M. and Magleby, R. (Editors) Agricultural Resources and Environmental Indicators, 1996-97. USDA Agricultural Handbook No. 712. Available at: http://www.ers.usda.gov/publications/ah712/AH712.PDF Accessed December 2011.

**ARPA, 2011**. Agenzia Regionale Protezione dell'Ambiente della Lombardia. Archivio dati meteorologici - Rete meteorologica di Arpa Lombardia. Available at: http://ita.arpalombardia.it/meteo/dati/richiesta.asp Accessed October 2011.

**Arsenault and Bonn, 2005**. Arsenault, E., Bonn, F. Evaluation of soil erosion protective cover by crop residues using vegetation indices and spectral mixture analysis of multispectral and hyperspectral data. Catena 62 (2005) 157–172.

**Bannari et al., 2006**. Bannari, A., Pacheco, A., Staenz, K., McNairn, H., Omari, K. Estimating and mapping crop residues cover on agricultural lands using hyperspectral and IKONOS data. Remote Sensing of Environment. 104 (2006) 447 – 459

**Bannari et al., 2007a**. Bannari, A., Chevrier, M., Staenz, K., McNairn, H. Potential of hyperspectral indices for estimating crop residue cover. Revue Télédétection. vol. 7, n° 1-2-3-4, p. 447-463.

**Bannari et al., 2007b**. Bannari, A., Staenz, K., Khurshid, K. S. Remote Sensing of Crop Residue Using Hyperion (EO-1) Data. IEEE. 1-4244-1212-9/07. Available at: ftp://ftp.gsfc.nasa.gov/projects/nasa_barc/outgoing/EO1refs/banari.pdf Accessed December 2011.

**Baret et al., 1993**. Baret, F., Jacquemoud, S., Hanocq, J.F. About the soil line concept in remote sensing. Advances in Space Research (ISSN 0273-1177), vol. 13, no. 5, p. 281-284

**Barry, 2001**. Barry, P. EO-1/ Hyperion Science Data User's Guide. Available at: http://www.eoc.csiro.au/hswww/oz_pi/docs/EO1_DUG.PDF Accessed October 2011.

**Ben-Dor et al., 2009**. Ben-Dor, E., Chabrillat, S., Demattê, J.A.M., Taylor, G.R., Hill, J., Whiting, M.L., Sommer, S. Using Imaging Spectroscopy to study soil properties. Remote Sensing of Environment 113 (2009) S38–S55

**Boettcher et al., 2008**. Boettcher, K., Kemper, T., Machwitz, M., Mehl, W., Sommer, S. Chemometric Modelling and Remote Sensing of Arable Land Soil Organic Carbon as Mediterranean Land Degradation Indicator. JRC Scientific and Technical Reports (EUR collection). EUR23513 Available at: http://publications.jrc.ec.europa.eu/repository/bitstream/111111111/10750/1/eur23513en-som_final.pdf Accessed December 2010.

**Carfantan and Idier, 2010**. Carfantan, H., Idier, J. Statistical Linear Destriping of Satellite-Based Pushbroom-Type Images. IEEE transactions on geoscience and remote sensing. Vol. 48, No. 4, April 2010

**CCRS, 2007**. Canada Centre for Remote Sensing Fundamentals of Remote Sensing. Available at: http://www.ccrs.nrcan.gc.ca/resource/tutor/fundam/pdf/fundamentals_e.pdf Accessed December 2011.

**Dadon et al., 2010**. Dadon, A., Karnieli, A., Ben-Dor, E. Detecting and correcting the curvature effect (smile) in Hyperion images by use of MNF. Proc. 'Hyperspectral 2010 Workshop', Frascati, Italy, 17–19 March 2010 (ESA SP-683, May 2010)

**Datt et al., 2003**. Datt, B., McVicar, T.R., Van Niel, T.G., Jupp, D.L.B., and Pearlman, J.S. Preprocessing EO-1 Hyperion hyperspectral data to support the application of agricultural indices. IEEE Transactions on Geoscience and Remote Sensing, Vol. 41, No. 6, pp. 1246–1259.

**Daughtry and Hunt, 2008**. Daughtry, C.S.T., Hunt, E.R. Jr. Mitigating the effects of soil and residue water contents on remotely sensed estimates of crop residue cover. Remote Sensing of Environment 112 (2008) 1647 – 1657

**Daughtry et al., 2006**. Daughtry, C.S.T., Doraiswamy, P.C., Hunt, E.R.Jr., Stern, A.J., McMurtrey III, J.E., Prueger, J.H. Remote sensing of crop residue cover and soil tillage intensity. Soil & Tillage Research 91 (2006) 101–108

**Drusch, 2005**. Drusch, M., Crewell, S. Encyclopedia of Hydrological Sciences: Principles of Radiative Transfer. Edited by M G Anderson. Available at: http://media.wiley.com/product_data/excerpt/39/04714910/0471491039-1.pdf Accessed December 2011.

**Dunteman, 1989**. Dunteman, G.H. Principal Components Analysis. SAGE.

**EC, 2005**. European Commission, European Soil Bureau Network. Soil Atlas of Europe.

**EC, 2006a**. European Commission. Communication - Thematic Strategy for soil protection. COM(2006) 231 Available at: http://eusoils.jrc.ec.europa.eu/ESDB_Archive/Policies/Directive/com_2006_0231_en.pdf

**EC, 2006b**. European Commission. Summary of the impact assessment - Thematic strategy for soil protection. Available at: http://eusoils.jrc.ec.europa.eu/ESDB_Archive/Policies/Directive/sec_2006_1165_en.pdf SEC(2006)1165.

**EC, 2011**. Joint Research Centre, Institute for Enviroinment and Sustainability, Soil Action Soil Organic Carbon Content. Available at: http://eusoils.jrc.ec.europa.eu/ESDB_Archive/octop/octop_download.html Accessed August 2011.

**EEA, 2005**. European Environment Agency. The European environment - State and outlook 2005. Available at: http://www.eea.europa.eu/publications/state_of_environment_report_2005_1/SOER2005_all.pdf Accessed July 2009.

**Einax et al., 1997**. Einax, J.W., Zwanziger, H.W., Geiss, S. Chemometrics in environmental analysis. VCH.

**Encyclopædia Britannica, 2011**. Encyclopædia Britannica. Soil (Web page). Available at: http://www.britannica.com.pros.lib.unimi.it/EBchecked/topic/552611/soil Accessed September 2011.

**FAO, 2006**. Food and Agriculture Organization of the United Nations. World reference base for soil resources 2006. World Soil Resources Reports 103. Available at: ftp://ftp.fao.org/agl/agll/docs/wsrr103e.pdf Accessed October 2011.

**FAO, 2008**. Food and Agriculture Organization of the United Nations. The main principles of conservation agriculture (Web site). Available at: http://www.fao.org/ag/ca/1b.html. Accessed October 2011.

**Gao et al., 2006**. Gao, B.C., Davis, C.O., Goetz, A.F.H. A Review of Atmospheric Correction

Techniques for Hyperspectral Remote Sensing of Land Surfaces and Ocean Color. Proceedings of the IEEE Environmental Applications Imaging Spectroscopy, 2006 Available at: http://webdocs.dow.wur.nl/internet/grs/Workshops/Environmental_Applications_Imaging_Spectroscopy/6_Gao_Atmosphere/IEEE_Gao_Atmosphere.pdf Accessed September 2011.

**Gao et al., 2007**. Gao, B.-C., Marcos, J.M., Davis, C.O., Goetz, A.F.H. Atmospheric correction algorithms for hyperspectral remote sensing data of land and ocean. Remote Sensing of Environment 113 (2009) S17–S24. Elsevier.

**GeoImage, 2010**. GeoImage Pty Ltd. Orthorectification (Web page). Available at: http://www.geoimage.com.au/geoimage/index.php?page=orthorectification Accessed December 2011.

**Gershenson, 2003**. Gershenson, C. Artificial Neural Networks for Beginners. Available at: http://arxiv.org/ftp/cs/papers/0308/0308031.pdf Accessed December 2011.

**Gilliam, 2007**. Gilliam, J.W., Osmond, D.L. and Evans, R.O. Selected agricultural best management practices to control nitrogen in the Neuse River Basin. North Carolina Agricultural Research Service, Technical Bulletin 31. Available at: http://www.soil.ncsu.edu/publications/BMPs/glossary.html Accessed February 2009.

**Gomez et al., 2008**. Gomez, C., Viscarra Rossel, R.A., McBratney, A.B. Soil organic carbon prediction by hyperspectral remote sensing and field vis-NIR spectroscopy: An Australian case study. Geoderma 146 (2008) 403–411.

**Goodenough et al., 2003**. Goodenough, G.D., Dyk, A., Niemann, O.K., Pearlman, J.S. Preprocessing Hyperion and ALI for forest classification.. IEEE Transactions on Geoscience and Remote Sensing, 41(6 Part 1): 1321-1331.

**GRASS, 2011.**. GRASS Development Team. Geographic Resources Analysis Support System (GRASS) Software. Available at: http://grass.osgeo.org Version 6.4.1. Open Source Geospatial Foundation.

**Grubinger, 1999**. Grubinger, V. Sustainable Vegetable Production. NRAES.

**Guerschman et al., 2009**. Guerschman, J.P., Hill, M.J., Renzullo, L.J., Barrett, D.J., Marks, A.S., Botha, E.J., Estimating fractional cover of photosynthetic vegetation, non-photosyntheticvegetation and bare soil in the Australian tropical savanna region upscaling the EO-1Hyperion and MODIS sensors. Remote Sensing of Environment 113 (2009) 928–945.

**Hibbert et al., 2008**. Hibbert, D.B., Minkkinen, P., Faber, N.M., Wise, B.M. A glossary of concepts and terms in chemometrics. IUPAC (International Union of Pure and Applied Chemistry) project. Available at: http://www.iupacterms.eigenvector.com/index.php?title=About_the_project Accessed December 2011.

**Hibbert et al., 2009**. Hibbert, D.B., Minkkinen, P., Faber, N.M., Wise, B.M. IUPAC project: A glossary of concepts and terms in chemometrics. Analytica Chimica Acta 642 (2009) 3–5.

**Höskuldsson, 2004**. Höskuldsson, A. Centring and scaling of data. Available at: http://www.chemometrics.se/images/stories/pdf/mar2004.pdf Accessed December 2011.

**IAEA, 2003**. International Atomic Energy Agency (IAEA), Soil and Water Management & Crop Production Section. Management of crop residues for sustainable crop production. Results of a co-ordinated research project organized by the Joint FAO/IAEA Division of Nuclear Techniques in Food and Agriculture 1996–2001. Available at: http://www-pub.iaea.org/MTCD/publications/PDF/te_1354_web.pdf Accessed December 2011.

**ISRIC, 2011**. ISRIC - World Soil Information. Luvisols. Available at: http://www.isric.org/about-soils/world-soil-distribution/luvisols Accessed November 2011.

**ITT VIS, 2009**. ITT Visual Information Solutions. ENVI Tutorial: Advanced Hyperspectral Analysis. Available at: http://www.ittvis.com/portals/0/tutorials/envi/Adv_Hyperspectral_Analysis.pdf Accessed October 2011.

**ITT VIS, 2011a**. ITT Visual Information Solutions. ENVI Tutorial: Introduction to Hyperspectral data. Available at: http://www.ittvis.com/portals/0/tutorials/envi/Hyperspectral_Intro.pdf Accessed October 2011.

**ITT VIS, 2011b**. ITT Visual Information Solutions. Atmospheric Correction Module: QUAC and FLAASH User's Guide. Available at: http://www.ittvis.com/portals/0/pdfs/envi/Flaash_Module.pdf Accessed July 2011.

**Kawishwar, 2007**. Kawishwar, P. Atmospheric Correction Models for Retrievals of Calibrated Spectral Profiles from Hyperion EO-1 Data. Available at: http://www.itc.nl/library/papers_2007/msc/iirs/kawishwar.pdf Accessed June 2011.

**Kayadibi, 2011**. Kayadibi, O. Evaluation of imaging spectroscopy and atmospheric correction of multispectral images (Aster and LandsaT 7 ETM+). International Conference on Recent Advances in Space Technologies (RAST), 2011

**Kirby et al., 2004**. Kirkby, M.J., Jones, R.J.A., Irvine, B., Gobin, A, Govers, G., Cerdan, O., Van Rompaey, A.J.J., Le Bissonnais, Y., Daroussin, J., King, D., Montanarella, L., Grimm, M., Vieillefont, V., Puigdefabregas, J., Boer, M., Kosmas, C., Yassoglou, N., Tsara, M., Mantel, S., Van Lynden, G.J. and Huting, J. Pan-European Soil Erosion Risk Assessment: The PESERA Map, Version 1 October 2003.. Explanation of Special Publication Ispra 2004 No.73 (S.P.I.04.73).

**Kneizys et al., 1996**. Kneizys, F.X., Robertson, D.C., Abreu, L.W., Acharya, P., Anderson, G.P., Rothman, L.S., Chetwynd, J.H., Selby, J.E.A., Shettle, E.P., Gallery, W.O., Clough, S.A., Bernstein, L.S. The MODTRAN 2/3 Report and LOWTRAN 7 MODEL. Ontar Corporation.

**Kottek et al., 2006**. Kottek, M., Grieser, J., Beck, C., Rudolf, B., Rubel, F. World Map of the Köppen-Geiger climate classification updated. Meteorologische Zeitschrift, Vol. 15, No. 3, 259-263 (June 2006) Available at: http://koeppen-geiger.vu-wien.ac.at/pdf/Paper_2006.pdf Accessed November 2011.

**Kroeck, 2011**. Kroeck, S. Crop Rotation and Cover Cropping: Soil Resiliency and Health on the Organic Farm. Chelsea Green Publishing.

**Kruse, 2004**. Kruse, F.A. Comparison of ATREM, ACORN, and FLAASH atmospheric corrections using low-altitude AVIRIS data of Boulder, CO. Available at: http://www.hgimaging.com/PDF/Kruse-JPL2004_ATM_Compare.pdf Accessed October 2011.

**Lal, 2003**. Lal, R. Crop residues and soil carbon. Available at: http://www.fao.org/ag/ca/Carbon%20Offset%20Consultation/CARBONMEETING/3FULLPAPERSBYCONSULTATIONSPEAKERS/PAPERLAL.pdf Accessed December 2011.

**Levin, 1999**. Levin, N. Fundamentals of Remote Sensing. Available at: http://geography.huji.ac.il/personal/Noam%20Levin/1999-fundamentals-of-remote-sensing.pdf Accessed December 2011.

**Louwagie et al., 2009a**. Louwagie, G., Gay, S.H., Sammeth, F., Ratinger, T., Maréchal, B., Prosperi, P., Rusco, E., Terres, J.-M., van der Velde, M., Baldock, D., Bowyer, C., Cooper, T., Fenn, I., Hagemann, N., Prager, K., Heyn, N., Schuler, J. Final report on the project 'Sustainable Agriculture and Soil Conservation (SoCo). Available at: http://soco.jrc.ec.europa.eu/documents/EUR-23820-web.pdf Accessed October 2009.

**Louwagie et al., 2009b**. Louwagie, G., Gay, S.H., Burrell, A., Sammeth, F., Ratinger, T., Cristoiu, A., Maréchal, B., Prosperi, P., Rusco, E., Terres, J.-M., Adhikari, K., Bodis, K., Cenci, R.M., Gardi, C.,

Houskova, B., Reuter, H.I., Lado, L.R., Stolbovoy, V., Toth, G., Schuler, J., Kutter, T., Zander, P., Funk, R., Helming, K., Doublet, S., Houtin, M., Pointereau, P. Addressing soil degradation in EU agriculture. Relevant processes, practices and policies. Report on the project 'Sustainable Agriculture and Soil Conservation (SoCo)'. Available at: http://soco.jrc.ec.europa.eu/documents/EUR-23767-web.pdf Accessed July 2011.

**Mark and Workman, 2007**. Mark, H., Workman, J. Chemometrics in spectroscopy. Elsevier.

**Martens and Naes, 1992**. Martens, H., Naes, T. Multivariate calibration. John Wiley and Sons.

**Meko, 2011**. Meko, D. Multiple Linear Regression. Available at: http://www.ltrr.arizona.edu/~dmeko/notes_11.pdf Accessed December 2011.

**Miller et al., 2010**. Miller, F.P., Vandome, A.F., McBrewster, J. Crop Rotation. VDM Publishing House Ltd.

**Montes et al., 2004**. Montes, M.J., Gao, B.-C., Davis, C.O. Hyperpectral remote sensing of ocean color: a comparison of Hyperion with AVIRIS. Available at: ftp://popo.jpl.nasa.gov/pub/docs/workshops/04_docs/Montes_et_al_aviris_2004.pdf Accessed July 2011.

**Monty et al., 2008**. Monty, J.G., Daughtry, C.S.T., Crawford, M. Assessing crop residue cover using Hyperion data. IGARSS (IEEE Geoscience and Remote Sensing Society) Conference proceedings.

**Nagler et al., 2000**. Nagler, P.L., Daughtry, C.S.T., Goward, S.N. Plant Litter and Soil Reflectance. Remote Sensning of the Environment. 71:207–215 (2000).

**Nagler et al., 2003**. Nagler, P.L., Inoue, Y., Glenn, E.P., Russ, A.L., Daughtry, C.S.T. Cellulose absorption index (CAI) to quantify mixed soil–plant litter scenes.

**NASA, 2011**. National Aeronautics and Space Administration. File:Atmospheric electromagnetic transmittance or opacity.jpg. Available at: http://commons.wikimedia.org/wiki/File:Atmospheric_electromagnetic_transmittance_or_opacity.jpg File in the public domain.

**NCAT, 2009**. National Center for Appropriate Technology (NCAT). Cover crops (Web page). NCAT Sustainable Agriculture Project. Available at: http://attra.ncat.org/attra-pub/covercrop.html Accessed June 2009.

**OGP, 2001**. Geodesy Subcommittee of the Geomatics Committee of the International Association of Oil & Gas Producers (OGP). Geomatics. EPSG Geodetic Parameter Dataset (Web page). Available at: http://info.ogp.org.uk/geodesy Accessed July 2011.

**Prosperi et al., 2011**. Prosperi, P., Terres, J.-M., Pointereau, P., Doublet, S. Conservation agriculture effects and policy support to mitigate soil degradation in Midi-Pyrénées (France). Land Degradation and Development. n. 22: 70–83 (2011).

**Provincia di Lodi, 2011**. Provincia di Lodi. Geoportale della Provincia di Lodi. Servizi WMS. Available at: http://cartografia.provincia.lodi.it

**QGIS, 2011**. Quantum GIS Development Team (2011). Quantum GIS Geographic Information System. Open Source Geospatial Foundation Project. Available at: http://qgis.osgeo.org Accessed October 2011.

**Regione Lombardia, 2011**. Regione Lombardia, Unità Organizzativa Infrastruttura per l'Informazione Territoriale, Direzione Generale Territorio e Urbanistica. Geoportale della Regione Lombardia. Available at: http://www.cartografia.regione.lombardia.it/rlregisdownload/ Accessed November 2011.

**Rios, 2011**. Rios, D. Neural networks: A requirement for intelligent systems. Available at:

http://www.learnartificialneuralnetworks.com/ Accessed December 2011.

**Roose, 1996**. Roose, E. Land husbandry - Components and strategy. FAO Soils Bulletin no.70. Available at: http://www.fao.org/docrep/T1765E/t1765e00.htm#Contents Accessed October 2011.

**Serbin at al., 2009a**. Serbin, G., Hunt, E.R., Daughtry, C.S.T., McCarty, G.W., Doraiswamy, P.C. An Improved ASTER Index for Remote Sensing of Crop Residue. Remote Sensing 2009, 1, 971-991; doi:10.3390/rs1040971

**Serbin et al., 2009b**. Serbin, G., Daughrty, C.S.T., Hunt, E.R.J., Brown, D.J., McCarty, G.W. Effects of Soil Spectral Properties on Remote Sensing of Crop Residue Cover. Soil Science Society of America Journal (SSSAJ): Volume 73: Number 5, September–October 2009. Available at: http://ddr.nal.usda.gov/bitstream/10113/36071/1/IND44256987.pdf

**Short, 2011**. Short, N.M. The Remote Sensing Tutorial. NASA. Available at: http://rst.gsfc.nasa.gov/ Accessed November 2011.

**Smith, 2006**. Smith, R.B. Introduction to Remote sensing of the Environment. MicroImages, Inc. Available at: http://www.microimages.com/documentation/Tutorials/introrse.pdf Accessed November 2011.

**Song, 2005**. Song, C. Spectral mixture analysis for subpixel vegetation fractions in the urbanenvironment: How to incorporate endmember variability?. Remote Sensing of Environment 95 (2005) 248–263.

**StatSoft Inc., 2011**. StatSoft Inc. Electronic Statistics Textbook. Available at: http://www.statsoft.com/textbook/ Accessed December 2011.

**Streck et al., 2002**. Streck, N.A., Rundquist, D., Connot, J. Estimating residual wjeat dry matter from remote sensing measurements. Photogrammetric engineering & remote sensing. Vol. 68, No. 11, November 2002, pp.1193-1201.

**Sun et al., 2008**. Sun, L., Neville, R., Staenz, K.,White, H.P. Automatic destriping of Hyperion imagery basedon spectral moment matching. Canadian Journal of Remote Sensing, Vol. 34, Suppl. 1, pp. S68–S81, 2008.

**The MathWorks Inc., 2011**. The MathWorks Inc. Statistics Toolbox - Partial Least Squares Regression and Principal Components Regression. Available at: http://www.mathworks.it/products/statistics/demos.html?file=/products/demos/shipping/stats/plspcrdemo.html Accessed December 2011.

**Tripathi, 2009**. Tripathi, R.S. Alkali land reclamation: a book for development. Mittal Publications.

**Tsai et al., 2005**. Tsai, F., Lin, S., Rau, J., Chen, L., Liu, G. Desriping Hyperion Imagery Using Spline Interpolation. Center for Space and Remote Sensing Research, Taiwan. Available at: http://gcl.csrsr.ncu.edu.tw/GCL/publication/destripingACRS2005.pdf Accessed November 2011.

**USDA, 2002**. United States Department of Agriculture (USDA). National Agronomy Manual. Available at: http://www.info.usda.gov/OpenNonWebContent.aspx?content=17894.wba Accessed April 2011. Document in the public domain (http://www.usda.gov/wps/portal/usda/usdahome?navid=POLICY_LINK).

**USGS, 2011**. United States Geological Survey (USGS), Earth Resources Observation and Science (EROS) Center. EO-1 (Earth Observing-1). http://eros.usgs.gov/#/Find_Data/Products_and_Data_Available/ALI Accessed August 2011.

**Verhulst et al., 2011**. Verhulst, N., Govaerts, B., Nelissen, V., Sayre, K.D., Crossa, J., Raes, D., Deckers, J. The effect of tillage, crop rotation and residue management on maize and wheat growth and

development evaluated with an optical sensor. Field Crops Research 120 (2011) 58–67

**Waldhoff et al., 2008**. Waldhoff, G., Bubenzer, O., Bolten, A., Koppe, W., Bareth, G. Spectral analysis of ASTER, HYPERION, and QUICKBIRD data for geomorphological and geological research in Egypt (Dakhla oasis, Western desert).. Conference proceedings of the The International Archives of the Photogrammetry, Remote Sensing and Spatial Information Sciences. Vol. XXXVII. Part B8. Beijing 2008. Available at: http://www.isprs.org/proceedings/XXXVII/congress/8_pdf/12_WG-VIII-12/03a.pdf Accessed October 2011.

**Warmerdam, 2011**. Warmerdam, F. FWTools: Open Source GIS Binary Kit for Windows and Linux. Available at: http://fwtools.maptools.org/ Accessed February 2011.

**Xie et al.,2010** . Xie, Y., Zhao, X., Li, L., Wang H. Calculating NDVI for Landsat7-ETM data after atmospheric correction using 6S model: A case study in Zhangye city, China. Digital Object Identifier: 10.1109/GEOINFORMATICS.2010.5567553

**Xu and Huang, 2007**. Xu, J.-F., Huang, J.-F. Empirical Line Method Using Spectrally Stable Targets to Calibrate IKONOS Imagery. Elsevier Limited and Science Press.

**Yuan and Niu, 2008**. Yuan, J.G., Niu, Z. Evaluation of Atmospheric Correction Using FLAASH. Proceedings of the International Workshop on Earth Observation and Remote Sensing Applications, 2008.

**Yuan et al., 2009**. Yuan, J.G., Niu, Z., Wang, X.P. Atmospheric correction of Hyperion hyperspectral image based on FLAASH. Guang Pu Xue Yu Guang Pu Fen Xi, 2009 May; 29(5):1181-5. Available at: http://www.ncbi.nlm.nih.gov/pubmed/19650448 Accessed October 2011.

# *Acknowledgements*

I would like to thank Giuseppe Elias, owner and manager of the Biancini Farm and his colleague Mr. Migliorini, for their support and help with the provision of data and for having allowed me to carry out samplings on their own fields.

Many thanks also to Stefan Sommer (JRC) for his advice in the remote sensing domain and Prof. Marco Acutis for his positive attitude towards my proposal to study conservation agriculture systems.

A sincere thank you also to all those unnamed who made this research possible and particularly to many valuable colleagues at the JRC in Ispra.

To you, Patrizia, my wife, I say thank you for all your love and infinite patience you had throughout these long years of hard work. Together, tomorrow, we'll achieve many more wonderful goals.